UNIVERSITY OF HAWAII
LIBRARY
DEC 15 '60

The Philosophical Magazine

FIRST PUBLISHED IN 1798

A Journal of Theoretical Experimental and Applied Physics

Vol. 5 September 1960 No. 57
Eighth Series

25s. 0d., plus postage
Annual Subscription £13 10s. 0d., payable in advance

Printed and Published by
TAYLOR & FRANCIS LTD
RED LION COURT, FLEET STREET, LONDON, E.C.4

THE PHILOSOPHICAL MAGAZINE

Editor

Professor N. F. Mott, M.A., D.Sc., F.R.S.

Editorial Board

Sir Lawrence Bragg, O.B.E., M.C., M.A., D.Sc., F.R.S.
Sir George Thomson, M.A., D.Sc., F.R.S.
Professor A. M. Tyndall, C.B.E., D.Sc., F.R.S.

Authors wishing to submit papers for publication in the Journal should send manuscripts directly to the Publishers.

Manuscripts should be typed in *double* spacing on one side of quarto (8 × 10 in.) paper, and authors are urged to aim at absolute clarity of meaning and an attractive presentation of their texts.

References should be listed at the end in alphabetical order of authors and should be cited in the text in terms of author's name and date. Diagrams should normally be in Indian ink on white card, with lettering in soft pencil, the captions being typed on a separate sheet.

A leaflet giving detailed instructions to authors on the preparation of papers is available on request from the Publishers.

Authors are entitled to receive 25 offprints of a paper in the Journal free of charge, and additional offprints can be obtained from the Publishers.

The *Philosophical Magazine* and its companion journal, *Advances in Physics*, will accept papers for publication in experimental and theoretical physics. The *Philosophical Magazine* publishes contributions describing new results, letters to the editor and book reviews. *Advances in Physics* publishes articles surveying the present state of knowledge in any branch of the science in which recent progress has been made. The editors welcome contributions from overseas as well as from the United Kingdom, and papers may be published in English, French and German.

Pyramidal Glide and the Formation and Climb of Dislocation Loops in Nearly Perfect Zinc Crystals†

By P. B. Price‡
Physics and Chemistry of Solids, Cavendish Laboratory, Cambridge§

[Received June 3, 1960]

Abstract

Zinc whiskers and platelets with a (0001) orientation and thin enough ($\lesssim \frac{1}{2}\mu$) to be transparent to 100 kv electrons were deformed in tension inside the electron microscope and the motion of individual dislocations followed by the transmission technique. These observations were then related to the macroscopic properties as determined by stress–strain curves. The crystals, which were found to be initially free of dislocations, deformed mainly by twinning (which is not considered here) or by pyramidal glide on the $(11\bar{2}2)$ $[\bar{1}\bar{1}23]$ system. Dislocations with three types of Burgers vectors were produced: long $\langle\bar{1}\bar{1}20\rangle$ dislocations which were easily immobilized and contributed very little to the deformation; short $\langle\bar{1}\bar{1}23\rangle$ screw dislocations which caused pyramidal glide and sometimes left behind long, narrow $\langle\bar{1}\bar{1}23\rangle$ loops which then split up into circular loops with the same Burgers vector; and circular $\langle 0001\rangle$ loops which were formed from $\langle\bar{1}\bar{1}23\rangle$ loops by the reaction $\frac{1}{3}\langle\bar{1}\bar{1}23\rangle \rightarrow \frac{1}{3}\langle\bar{1}\bar{1}20\rangle + \langle 0001\rangle$. Both types of loops were sessile but disappeared by climb at room temperature at a rate which agreed with the predicted rate. The loops impeded the motion of dislocations and were responsible for the propagation of glide as a Lüders band.

§ 1. Introduction

During an investigation at the University of Virginia of the mechanical properties of zinc whiskers (Cabrera and Price 1958), preliminary experiments showed that the mechanical properties of single crystal 'ribbons' and platelets of zinc were also extremely interesting. These studies have been continued at the University of Cambridge, using the elegant technique of transmission electron microscopy developed by Hirsch *et al.* (1956) and others, and the results appear to be important, not only for their elucidation of some of the properties of whisker-like crystals but also because of their application to the properties of metals in bulk form.

Zinc whiskers and platelets less than about $\frac{1}{2}\mu$ thick proved to be ideal specimens for this type of study because they were already transparent to 100 kv electrons without thinning and because their surfaces were extremely smooth. The crystals were deformed inside the electron microscope and the motion of individual dislocations followed during and after straining. These observations were then compared with the macroscopic behaviour as determined by tensile stress-strain curves.

† Communicated by Dr. P. B. Hirsch.
‡ National Science Foundation Post-Doctoral Fellow, 1959–60.
§ Permanent address: General Electric Research Laboratory, Schenectady, New York.

§ 2. Experimental Procedure

The thin crystals were grown from zinc vapour of high purity by the technique of Coleman and Sears (1957). The investigation was limited to whiskers whose direction of growth was in the basal plane and to platelets whose largest faces were parallel to the basal plane. Thus, in the tensile tests the axis of tension was always parallel to the basal plane. All the crystals were rectangular in cross section and ranged in length from 2 to 6 mm, in width from 10 μ to 1 mm, and in thickness from 0·05 to 0·5 μ. Crystals less than about 20 μ wide were generally referred to as whiskers and wider ones as platelets.

Macroscopic properties were studied with a high sensitivity tensile testing machine, developed by Marsh (1959), which was capable of measuring extensions of less than 100 Å reproducibly. A specimen was mounted with diphenyl-carbazide and observed during deformation at low magnification ($\times$ 100). After the completion of a test it was removed and examined at high magnification in a metallurgical microscope.

The microscopic behaviour was observed in a Siemens Elmiskop 1 electron microscope during plastic deformation in a tensile straining device designed by Fisher (1959) to replace the normal stereo specimen holder. A crystal was mounted with drops of collodion to the two jaws of a tiny chuck which could be forced apart by a wedge device. The wedge was coupled directly to the normal stereo-drive, so that the crystal could be strained in tension by simply rotating the stereo-drive knob located on the outside of the microscope. The specimen gauge length was 0·8 mm and the maximum obtainable plastic strain about 6%, corresponding to four complete turns of the stereo-drive knob.

§ 3. Results

3.1. *Tensile Tests and Observations in the Optical Microscope*

Since the axis of tension was always parallel to the (0001) plane, basal glide was impossible, and plastic deformation began either by the nucleation and growth of a twin or by the initiation and propagation of non-basal glide in the form of a Lüders band. In some cases both twinning and non-basal glide occurred. Only the latter is discussed here; twinning is considered in another paper (Price 1960 a).

Figure 1 is a typical stress–strain curve for a crystal which deformed by nonbasal glide. The elastic region, OY, was linear and extended to a maximum strain which ranged from about 2×10^{-3} for large platelets to 10^{-2} for whiskers. At some point on the crystal, usually at a large growth step or near one of the grips, plastic deformation started and the stress dropped to a value A, about $\frac{2}{3}$ of the yield stress. In the region of easy glide, AB, a Lüders band, clearly observable in the optical microscope at low magnification, was propagated from this point along the crystal, with most of the deformation taking place in a very localized region at the head of the band. If the stress was reduced below the flow stress, creep occurred. If the

stress was completely removed and the crystal allowed to rest for about an hour in the easy glide region, further deformation took place at various points all along the band at about the same flow stress as before. Finally fracture occurred at B at a plastic strain of about 5% to 10%. Sometimes a crystal did not fracture until after the Lüders band had run along its entire length and some further glide had taken place. This only happened with narrow whiskers and was accompanied by an appreciable increase in the flow stress (not shown in fig. 1).

Figure 2† is an optical micrograph of a deformed platelet, after fracture at B, showing the appearance of the glide lines which made up the Lüders band, AC. To the right of C no evidence of plastic deformation could be detected in the optical microscope.

Fig. 1

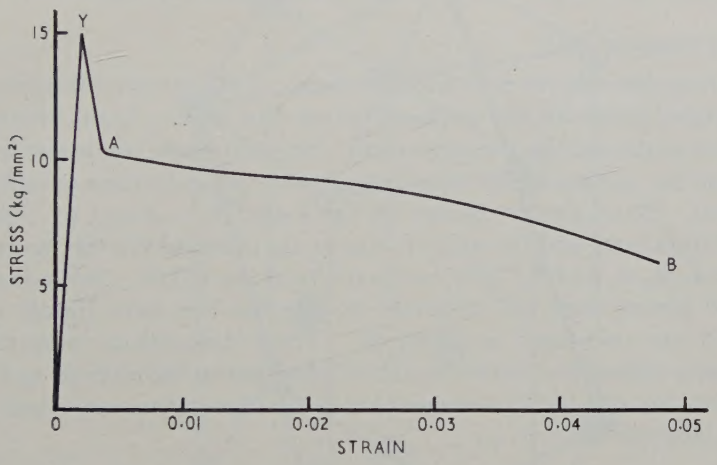

Typical stress–strain curve for a platelet.

The line D is simply a growth step running the length of the crystal. Note that the glide lines and the fractured edges are perpendicular to the edges of the crystal, which run in close-packed directions.

Two features of fig. 2 tell us that the Burgers vector of the deformation must be out of the basal plane:

(1) The crystal does not decrease in width in the deformed region AC.

(2) The glide lines are perpendicular to the axis of tension.

3.2. *Deformation Inside the Electron Microscope*

A tremendous amount of information was gained by observing the various stages of the deformation at high magnification with the transmission electron microscopic technique. Every crystal, provided it was mounted properly, was found to be initially free of dislocations (Price 1960 b). After a very small amount of plastic strain, glide traces and

† Figures 2, 3, 4, 6, 7, 9, 10 and 11 are shown as plates.

dislocations were usually found in a narrow zone a few microns wide and extending all the way across the crystal. As was observed in the optical microscope, this zone was always located where the applied stress was concentrated, either at a large surface step or near one of the glue joints.

Figure 3 is an electron micrograph of part of a narrow deformed zone, with its boundaries indicated by arrows. Within this region were found glide traces, long dislocations lying predominantly in basal planes, short dislocations running from the top face to the bottom face, and a large number of dislocation loops ranging in diameter from a few tens of angstroms to a few thousand angstroms.

During further straining the region containing glide traces and dislocations grew, and by observations of their movement in a large number of crystals, it was possible to determine the nature of the dislocations and their role in the deformation. The results are summarized below.

3.2.1. *Prismatic glide*

The long dislocations were found to have a $\frac{1}{3}\langle 11\bar{2}0\rangle$ type Burgers vector. They glided prismatically on basal planes and on non-basal planes whose zone axis contained the Burgers vector, their non-basal components leaving traces on the surface which were in accurately straight lines parallel to this direction. Examples are shown in fig. 4 at *a*, *b*, *c*, *d* and *e*. The close-packed directions and the axis of tension are indicated in the figure by the vectors $\mathbf{a}_1$, $\mathbf{a}_2$, $\mathbf{a}_3$ and $\mathbf{T}$. The components of the $\langle 11\bar{2}0\rangle$ dislocations lying in basal planes were not subjected to a stress but were simply dragged along by the non-basal components. These dislocations were therefore easily immobilized by obstacles such as loops, other dislocations and surface imperfections, and their movement accounted for only a very small portion of the plastic strain.

3.2.2. *Pyramidal glide*

Most of the deformation resulted from the formation and movement of large numbers of the short dislocations, which produced glide lines whose integrated effect was visible in the optical microscope at low magnification. Isolated traces due to the movement of these dislocations are visible in fig. 4 at A, B, C, D, E, F and G. From the directions and widths of the traces, it was possible to identify the glide planes of the short dislocations, provided the thickness of the crystal was known. This was determined, in crystals which twinned at some stage of the deformation, by measuring the projected width of a coherent twin boundary, which was known to lie on a $\{10\bar{1}2\}$ plane.

It was found that the short dislocations always glided on pyramidal planes with a common $\langle 11\bar{2}3\rangle$ zone axis. Because of the ease with which the dislocations were able to cross-glide from one pyramidal plane to another (see trace E in fig. 4), it was concluded that their Burgers vectors were of the $\frac{1}{3}\langle 11\bar{2}3\rangle$ type and that they were of screw character. We saw in § 3.1 that the direction of glide had to be out of the basal plane, and the

vector $\frac{1}{3}\langle \bar{1}\bar{1}23 \rangle = \mathbf{c}+\mathbf{a}$ is the smallest non-basal lattice vector along which there was a finite resolved shear stress.

The most common pyramidal glide plane was $\{11\bar{2}2\}$, which was responsible for the high density of glide lines visible in the optical microscope. One of these planes is indicated in figure 5, along with the $[\bar{1}\bar{1}23]$ glide direction. It is clear from figs. 4 and 6 that pyramidal glide was not restricted to a $(11\bar{2}2)$ plane but could occur on other pyramidal planes, such as $(10\bar{1}1)$, containing the $[\bar{1}\bar{1}23]$ direction, provided the resolved shear stress on them was sufficiently high.

Fig. 5

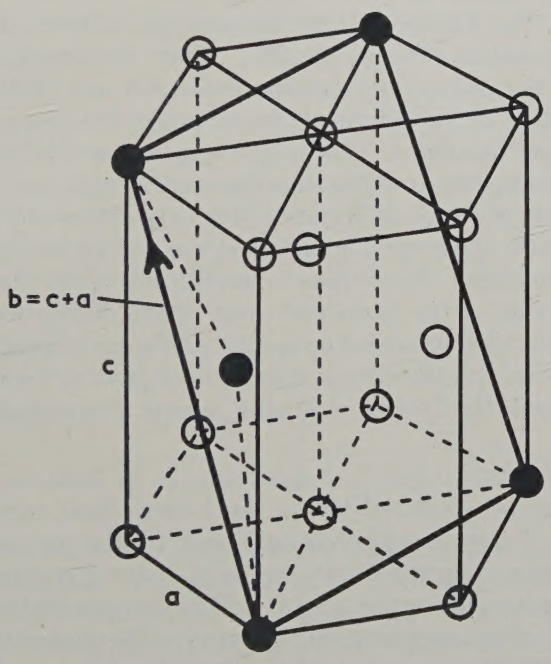

$(11\bar{2}2)$ $[\bar{1}\bar{1}23]$ glide system.

3.2.3. *Dislocation loops*

Dislocation loops, circular in shape and oriented on basal planes (see figs. 3, 4, 6, 7, 9, 10, 11) were formed during pyramidal glide, as a direct result of the motion of $\langle \bar{1}\bar{1}23 \rangle$ type dislocations. This is clearly demonstrated in figs. 4 and 6, which show loops arranged in rows along the paths which individual $\langle \bar{1}\bar{1}23 \rangle$ dislocations have taken.

Loops were only associated with pyramidal traces. Along some traces there were many large, closely spaced loops (fig. 6); along some were a small number of widely spaced, very tiny loops (traces B, D, G, fig. 4); and along others no loops were formed. When the deformation became so

intense that many traces overlapped (fig. 7), it was no longer possible to associate loops with individual traces.

Since none of these loops was observed to glide on the basal plane, it was concluded that their Burgers vectors were out of the basal plane. The results of a detailed study of the loops are presented in § 3.3.

3.2.4. *Propagation of the Lüders band*

It was stated earlier that deformation began with the formation and movement of dislocations in a very narrow region extending across the crystal. During further straining the density of dislocations in this region increased and a large number of loops was produced, which acted as obstacles to the motion of $\langle \bar{1}\bar{1}20 \rangle$ dislocations. This is demonstrated in figs. 6 and 7. The blocked $\langle \bar{1}\bar{1}20 \rangle$ dislocations, in turn, made the glide of $\langle \bar{1}\bar{1}23 \rangle$ dislocations difficult (fig. 3). When the density of loops was very high, all the dislocations became entangled and further glide took place at the edges of the deformed region, where few loops were present, causing it to grow in width. This process was responsible for the propagation of a deformation front which was observed optically as a Lüders band.

If, at some stage of the deformation, the crystal was allowed to rest at room temperature, the loops diminished in size and gradually disappeared, allowing the entangled dislocations to anneal out of the crystal. Within about one hour all of the loops and most of the dislocations were gone. Further straining then produced more glide and more loops in the deformed region. This explains the optical observations that new glide lines could be produced *inside* the Lüders band after a room temperature anneal.

3.2.5. *Fracture*

Usually a crystal fractured before the Lüders band extended over its entire length. Fracture was preceded either by the formation of a twin (Price 1960 a) or by a decrease in thickness of a narrow region a few microns wide and extending across the crystal. This decrease in thickness, which was obvious from the increasing transparency of the narrow region, was due to the movement of large numbers of $\langle \bar{1}\bar{1}23 \rangle$ dislocations on a few pyramidal planes. Once the thinning became appreciable, all of the glide took place in this region, where the stress was highest, until the crystal simply glided in two. The observation of increasing transparency with increasing glide is, of course, further proof that the Burgers vector was out of the basal plane.

3.3. *Detailed Study of the Loops*

3.3.1. *Origin and Burgers vector*

There are two possible ways in which the loops could have originated during pyramidal glide; (1) by a dislocation mechanism involving the $\langle \bar{1}\bar{1}23 \rangle$ dislocations or (2) by condensation of discs of point defects produced during glide. In many cases loops were actually observed in the process of

forming by the first mechanism. This process occurred too rapidly to be photographed, but the successive stages are drawn schematically in fig. 8. During the passage of a $\langle \bar{1}\bar{1}23 \rangle$ screw dislocation a long narrow loop was left behind, (*a*), which was unstable and went through configurations such as (*b*) and (*c*), finally becoming a series of circular loops, (*d*), within a period of 1 to 5 sec. The total area enclosed by the circular loops appeared to be about the same as that enclosed by the original loop. Sometimes several long narrow loops, running in the same direction, were formed at the same time on nearby planes. The long loops then split up into circular loops whose positions were determined by their mutual stress fields. As fig. 9 shows, the circular loops tended to occur in clusters, each loop of a cluster being situated in the same plane as the parent loop from which it was formed.

Fig. 8

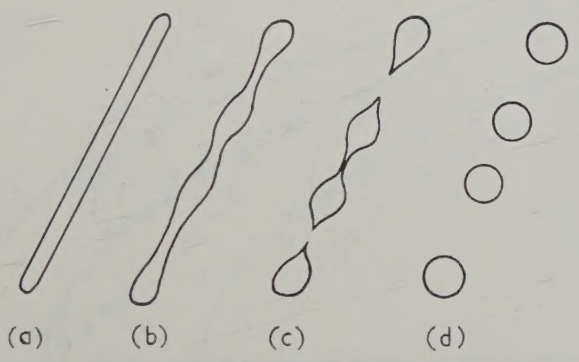

Formation of circular loops from long $\langle \bar{1}\bar{1}23 \rangle$ loops.

The Burgers vector of a loop formed by the dislocation mechanism should be different from that of a loop formed by point defect condensation. In the first case one would expect the Burgers vector to be either $\frac{1}{3}\langle \bar{1}\bar{1}23 \rangle$ or another lattice vector related to it by a simple dislocation reaction. In the second case the Burgers vector would be either $\frac{1}{2}\langle 0001 \rangle$ or $\frac{1}{6}\langle \bar{2}023 \rangle$, neither of which is a lattice vector, and the loop would enclose a stacking fault.

In order to help determine the Burgers vectors, selected area diffraction patterns were obtained for a large number of loops and compared with the corresponding micrographs. It will be noticed in figs. 3, 4, 6, 7, 9, 10 and 11 that some of the loops are fairly uniform in contrast around their periphery (figs. 6 and 9), whereas others vary in contrast, actually becoming invisible along a certain azimuth (figs. 3, 10 (*a*) and 11). It was found that the diffraction pattern of every region containing loops with varying contrast was characterized by a strong reflection from planes parallel to the azimuth along which the contrast was zero or a minimum. This is illustrated in fig. 10 (*a*), which shows loops whose contrast vanishes along a

direction parallel to $(11\bar{2}0)$ planes. The diffraction pattern, fig. 10 (*b*), is in the same orientation as the micrograph. Similar results were obtained when the strong reflection was from $(10\bar{1}0)$ planes. It was concluded that the Burgers vectors of the loops with invisible portions were always $\langle 0001 \rangle$ and that the contrast was due to the edge component of the dislocation, that is, it resulted from displacements of atoms in the plane of, but normal to, the loops. When the displacements were parallel to reflecting planes, no contrast was produced (Howie and Whelan 1960). The possibility of a $\frac{1}{2}\langle 0001 \rangle$ Burgers vector was ruled out because no stacking fault contrast was ever observed inside these loops.

Fig. 12

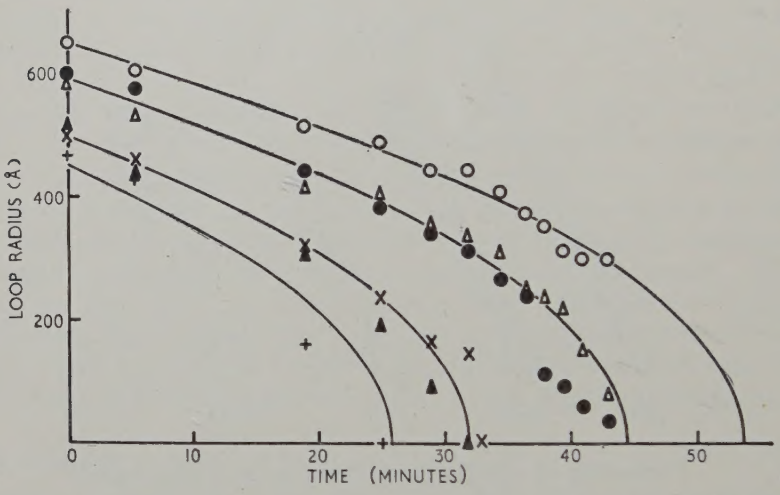

Decrease of radius with annealing time for the six largest loops in fig. 11. The parabolas drawn through the points can be made to coincide by translations along the time axis.

Evidence that the $\frac{1}{3}\langle \bar{1}\bar{1}23 \rangle$ Burgers vector also occurred is seen in fig. 10 (*c*), which shows a number of loops which were formed by the dislocation mechanism. Those at A are of the $\langle 0001 \rangle$ type, with vanishing contrast along a direction parallel to the $(11\bar{2}0)$ reflecting planes (see the diffraction pattern, fig. 10 (*d*)). Each of the other loops shows contrast which, although it varies around the periphery, never completely disappears, and this can only occur if the Burgers vector has a component normal to the reflecting planes. To a first approximation, this contrast is due to a superposition of the contrast from a $\langle 0001 \rangle$ loop and of that from a loop with a Burgers vector in the basal plane.

The most likely explanation for the two different types of contrast is that all of the loops originally had the Burgers vector of their generating $\langle \bar{1}\bar{1}23 \rangle$ dislocations, but that the three loops at A underwent a reaction of the type $\frac{1}{3}\langle \bar{1}\bar{1}23 \rangle \rightarrow \frac{1}{3}\langle \bar{1}\bar{1}20 \rangle + \langle 0001 \rangle$. The $\langle \bar{1}\bar{1}20 \rangle$ loops then disappeared by

glide in the basal plane, leaving loops with a ⟨0001⟩ Burgers vector and with a lower energy.

No evidence was found in the diffraction studies that any of the loops were formed by the condensation of vacancies or interstitials.

3.3.2. *Annealing of loops at room temperature*

The kinetics of annealing of the loops at room temperature were studied by taking a series of high magnification electron micrographs of a small region containing loops over a period of about one hour and measuring the radii of the loops as a function of time. In order to minimize the temperature rise in the crystal due to bombardment by electrons, the high voltage was turned off between exposures, so that the crystal was heated for only a few seconds every five minutes or so.

Fig. 13

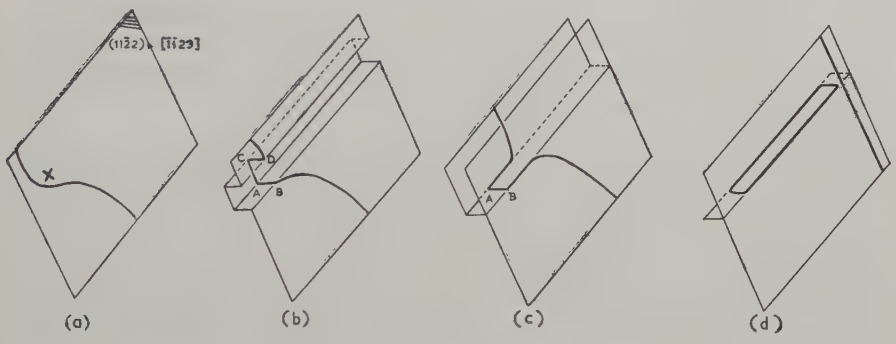

Formation of elongated loops from the multiple jog, AB.

Figure 11 shows qualitatively the behaviour of a large number of loops and fig. 12 is a plot of the radii, r, of the six largest loops in fig. 11 as a function of time, t. It is seen that the loops remained circular during annealing and that the rate of shrinking increased as the loops became smaller. From a plot of log r vs. log t it was ascertained that all of the data could be fitted fairly well by the parabolic equation

$$r^2 = A(t-\tau),$$

where $A \simeq -1{\cdot}3 \times 10^{-14}\,\mathrm{cm}^2/\mathrm{sec}$ is a constant and τ, the intercept of the parabola on the time axis, is the time at which a loop disappeared ($r=0$). The curves in fig. 12, which are parabolas obtained from this equation, are all identical except for a translation along the time axis.

§ 4. Interpretation and Discussion

4.1. *Formation of Loops*

It seems fairly certain that the elongated loops which split up into circular loops were formed from multiple jogs in ⟨$\bar{1}\bar{1}23$⟩ screw dislocations. Figure 13 shows a plausible way in which this could happen (proposed by Hirsch,

private communication). A fast-moving screw dislocation which is held back at some point by an obstacle at X is able to overcome the obstacle by double cross-glide along part of its length. This results in the formation of two multiple jogs, AB and CD. If this occurs near the surface of the crystal, one of the jogs, CD, may be able to glide along the dislocation to the surface, but AB will be prevented from gliding by the obstacle on one side and by a force due to the curvature of the moving dislocation on the other. AB will remain connected to the moving dislocation by two parallel lines. Eventually a long, narrow loop will be pinched off, perhaps when the dislocation cross glides again to avoid another obstacle.

This explanation is supported by evidence in fig. 4, trace E. It appears as though the dislocation encountered an obstacle at O, cross glided and acquired a multiple jog, produced a long loop which split up into a string of circular loops, then cross-glided back onto its original glide plane and lost its jog. At O, where cross glide started, the trace abruptly widened whereas it should have narrowed by an amount determined by the Burgers vector and the angle between the two cross-glide planes. The fact that the widening occurred only at one side of the trace is to be expected on the basis of the above model, in which one of the jogs glides to the surface. From the measured increase in trace width, the jog length was estimated at 200 Å. Assuming that the total area enclosed by the row of loops was the same as the area of the long loop from which they were formed, another estimate of the jog length was obtained by dividing the average area of a loop by the average spacing of loops. This gave about the same value.

Let us now consider the splitting of a long loop into circular loops. It is easy to see that the process involves a lowering of the energy, provided the circular loops exceed a certain diameter. The total energy of n circular loops with a [0001] Burgers vector is $[n\mu\mathbf{b}^2d/4(1-\nu)]\log(d/\mathbf{b}_0)$, where μ is the shear modulus, ν is Poisson's ratio, d is the loop diameter, and $\mathbf{b}_0 \sim \mathbf{b}$. The energy of a long loop can be approximated by the interaction energy of two parallel edge dislocations of length L, separated by a distance r, and this is given by $[\mu\mathbf{b}^2L/2\pi(1-\nu)][\log(r/\mathbf{b}_0)+\frac{1}{2}]$. On the assumption that $n\pi d^2/4 = rL$, the necessary condition for splitting is found to be

$$\frac{d}{\log(d/\mathbf{b}_0)} \geqslant \frac{2r}{\log(r/\mathbf{b}_0)+\frac{1}{2}}.$$

From measurements of loop sizes and spacings in the micrographs, estimates of the widths of elongated loops were made and found to satisfy the above inequality in all cases.

Although the energy of a long loop is lowered by splitting, this can only take place at a temperature at which jogs can easily be formed. Once the loop becomes jogged, the process may be assisted by pipe diffusion along its periphery, because of the large Burgers vector of the dislocation ($\mathbf{b} = 5{\cdot}1$ Å). Experiments are now in progress to see if zinc platelets deformed at low temperature inside the electron microscope contain elongated loops instead of circular ones.

Evidence is beginning to accumulate that dislocation loops are formed during the deformation of many ductile materials. Segall (1960) has observed loops in fatigued specimens of Al, Cu, Ni and Au which were electrolytically thinned after deformation and examined by transmission electron microscopy. He found a very high density of long, narrow loops in Cu, Ni and Au and a high density of circular loops in Al. Elongated loops have also been seen in specimens of Cu – 2·5% Al which were deformed in tension and thinned for examination by the transmission technique (Howie 1960).

Dash (1958) has etched silicon crystals deformed at high temperature and found trails of defects extending behind screw dislocations along the direction of their motion and joining them at cusps. He suggested that the trails exerted a dragging force on the dislocations and that they were formed by the nonconservative motion of jogs.

Johnston and Gilman (1960) have concluded, from etch-pit studies of deformed crystals of LiF and MgO, that moving screw dislocations with multiple jogs ranging in size from 3**b** to 300**b** produce defect trails from which long dislocation loops are formed. This has recently been confirmed for MgO crystals by Washburn *et al.* (private communication), who have observed, by transmission electron microscopy, elongated loops which were probably formed during the motion of jogged screw dislocations. When heated to high temperature they split up into circular loops, in the same way as the loops in zinc did at room temperature.

Circular loops have been observed in large zinc samples, thinned for transmission microscopy, by Fourdeux and Berghezan (1960) and by Brown (private communication), but most of them contained stacking faults and were believed to have been produced by vacancy condensation. The nature of the contrast at the loops observed by Brown has recently been analyzed by Howie and Whelan (1960), using the dynamical theory of electron diffraction and including a term to take account of incoherent scattering.

4.2. *Climb of Loops at Room Temperature*

Because of its prismatic nature, a loop produced by pyramidal glide can only shrink by climb. As we shall see, the observed rates of shrinking are quantitative evidence that climb does occur easily at room temperature in zinc by the diffusion of vacancies either to or from a loop, depending on whether it is of vacancy or interstitial type.

The rate of shrinking of a loop as a function of temperature and radius has been worked out by Silcox and Whelan (1959), using Friedel's theory of climb (1956). The surfaces of a thin specimen (~ 1000 Å) are very effective sources and sinks of vacancies. On the assumptions that the concentration of vacancies during annealing maintains its equilibrium value (zero chemical stress) and that the concentration of jogs in the loop is $\frac{1}{2}$, they obtain the equation

$$\frac{dr}{dt} = -\tfrac{1}{2}Z\nu_a \mathbf{b} \exp\left(-\frac{E_d}{kT}\right)\left[\exp\left(\frac{F_c \mathbf{b}^2}{kT}\right) - 1\right], \quad . \quad . \quad . \quad (1)$$

where r is the loop radius at time t; Z is an atomic coordination factor ~ 11; ν_a is an atomic vibration frequency $\sim 10^{13}$; $\mathbf{b}$ is the Burgers vector of the loop; E_d is the activation energy for self-diffusion; kT is the Boltzmann temperature factor; and $F_c = \mu\mathbf{b}^2 \log(r/\mathbf{b})/4\pi(1-\nu)r$ is the force due to the line tension and curvature of the loop.

In the range of loop radius and temperature of interest, the expression $\exp(F_c\mathbf{b}^2/kT) - 1$ can be approximated quite well by $\alpha\mathbf{b}/r$, where α is determined graphically. Equation (1) is then integrated to give

$$r = r_0[1-(t/\tau)]^{1/2}, \quad \ldots\ldots\ldots \quad (2)$$

where r_0 is the initial radius, at $t=0$, and τ is the time at which $r=0$, given by

$$\tau = \frac{r_0^2}{Z\nu_a\mathbf{b}^2\alpha}\exp\left(\frac{E_d}{kT}\right). \quad \ldots\ldots\ldots \quad (3)$$

The result should apply equally well to vacancy and interstitial type loops.

Equation (2) is equivalent to the empirical equation of § 3.3.2,

$$r^2 = A(t-\tau) \quad \ldots\ldots\ldots \quad (4)$$

with

$$A = -\frac{r_0^2}{\tau} = -Z\nu_a\mathbf{b}^2\alpha\exp\left(-\frac{E_d}{kT}\right). \quad \ldots\ldots \quad (5)$$

For $\langle 0001 \rangle$ loops in zinc at $\sim 300°$K (see fig. 11), α was found to be 240, and putting $\mathbf{b} = 4{\cdot}94$ Å and using the experimentally determined constant $A = -1{\cdot}3 \times 10^{-14}$ cm^2/sec, eqn. (5) was solved for E_d, giving $E_d = 0{\cdot}93$ ev, to be compared with the value 0·95 ev, for self-diffusion parallel to the c-axis, obtained by Shirn *et al.* (1953).

The excellent agreement justifies the assumptions that the average temperature rise in the specimen due to the electron beam was negligible and that the diffusion of vacancies between the loops and the surfaces was so fast that the equilibrium concentration was maintained.

4.3. *Macroscopic Properties*

The electron microscopic observations reported here have made it possible to understand some of the macroscopic properties of zinc whiskers and platelets in the (0001) orientation. It is now clear that a wide platelet has a lower yield point that a whisker, not because of a different dislocation configuration, since neither of them initially contains any dislocations, but because of the greater effectiveness of growth steps and of the glue joints in concentrating the stresses.

The occurrence of pyramidal glide on the $(11\bar{2}2)$ $[\bar{1}\bar{1}23]$ system, which was first reported by Bell and Cahn (1957), has been definitely established, by measurements on individual glide traces, as the major mode of glide in these whiskers and platelets and the one responsible for the optically visible glide lines. The $(11\bar{2}2)$ glide plane may be favoured over other pyramidal planes because the $[\bar{1}\bar{1}23]$ dislocations can lower their energy by splitting into partials on this plane in a reaction of the type

$$\tfrac{1}{3}[\bar{1}\bar{1}23] \rightarrow \tfrac{1}{6}[\bar{2}023] + \tfrac{1}{6}[0\bar{2}23] \text{ (Frank and Nicholas 1953).}$$

It has been seen that the propagation of a deformation front or Lüders band is a result of the formation of loops, which impede dislocations and force new glide to occur at the edges of the deformed region. It should be pointed out that this localized hardening is not accompanied by an increase in the average flow stress. In these crystals, which are initially free of dislocations, the flow stress is the stress necessary for glide at the edge of the deformed region, and this should only increase after the Lüders band has completely covered the crystal, as was observed. Similarly, a room temperature anneal, which eliminates the loops, should not affect the flow stress unless the whole crystal has been deformed.

§ 5. Summary

The most important results which emerged from the investigation were the following:

(1) Zinc whiskers and platelets with a (0001) orientation were initially free of dislocations and had a sharp yield point whose value was determined by stress concentrations at large surface steps or at the grips.

(2) Pyramidal glide in $\langle \bar{1}\bar{1}23 \rangle$ directions and mainly on $\{1122\}$ planes was the major mode of deformation in crystals which did not twin.

(3) Dislocations with three Burgers vectors were identified: (*a*) $\langle \bar{1}\bar{1}20 \rangle$ dislocations which glided prismatically and were easily immobilized; (*b*) $\langle \bar{1}\bar{1}23 \rangle$ dislocations, predominantly screw, which caused pyramidal glide and sometimes left behind long, narrow $\langle 1123 \rangle$ loops which then split up into circular loops with the same Burgers vector; and (*c*) $\langle 0001 \rangle$ loops which were formed from $\langle \bar{1}\bar{1}23 \rangle$ loops by the reaction

$$\tfrac{1}{3}\langle \bar{1}\bar{1}23 \rangle \rightarrow \tfrac{1}{3}\langle \bar{1}\bar{1}20 \rangle + \langle 0001 \rangle.$$

(4) Both types of loops impeded the motion of dislocations and were responsible for the propagation of the active glide region as a Lüders band.

(5) The loops diminished in size and disappeared by climb at room temperature by the diffusion of vacancies between the loops and the surfaces. From the annealing curves an activation energy for self-diffusion of 0·93 ev was obtained, in good agreement with the results of other workers.

Acknowledgments

I am indebted to Professor N. F. Mott, F.R.S., and Dr. F. P. Bowden, F.R.S., for their continued interest and encouragement and for making available the facilities of this laboratory. I am grateful to Dr. P. B. Hirsch for many valuable discussions and for reviewing the manuscript, to R. M. Fisher, who very kindly allowed me to use his straining stage, and to my colleagues in the Cavendish Laboratory for discussions.

This work was carried out during the tenure of a post-doctoral fellowship awarded by the U.S. National Science Foundation.

References

Bell, R. L., and Cahn, R. W., 1957, *Proc. roy. Soc.* A, **239,** 494.

Cabrera, N., and Price, P. B., 1958, *Report of the Cooperstown Conference on the Growth and Perfection of Crystals*, Ed. Doremus, Roberts and Turnbull (New York : Wiley), p. 204.

Coleman, R. V., and Sears, G. W., 1957, *Acta Met.*, **5,** 131.

Dash, W. C., 1958, *J. appl. Phys.*, **29,** 705.

Fisher, R. M., 1959, *Rev. sci. Instrum.*, **30,** 925.

Fourdeux, A., and Berghezan, A., 1960, *Compte rend.*, **250,** 3019.

Frank, F. C., and Nicholas, J. F., 1953, *Phil. Mag.*, **44,** 1213.

Friedel, J., 1956, *Les Dislocations* (Paris: Gauthier-Villars), p. 72.

Hirsch, P. B., Horne, R. W., and Whelan, M. J., 1956, *Phil. Mag.*, **1,** 677.

Howie, A., 1960, *Proceedings of European Regional Conference on Electron Microscopy, Delft* (to be published).

Howie, A., and Whelan, M. J.. 1960, *Proceedings of European Regional Conference on Electron Microscopy, Delft* (to be published).

Johnston, W. G., and Gilman, J. J., 1960, *J. appl. Phys.*, **31,** 632.

Marsh, D. M., 1959, unpublished. For an account of an earlier model see Marsh, D. M., 1959, *J. sci. Instrum.*, **36,** 165.

Price, P. B., 1960 a, *Proc. roy. Soc.* A (in the press); 1960 b, *Phil. Mag.*, **5,** 417.

Segall, R. L., 1960, *Ph.D. thesis*, University of Cambridge.

Shirn, G. A., Wajda, E. S., and Huntington, H. B., 1953, *Acta Met.*, **1,** 513.

Silcox, J., and Whelan, M. J., 1959, *Structure and Properties of Thin Films*, Ed. Neugebauer, Newkirk and Vermilyea (New York : Wiley), p. 164.

The Thermal Conductivity of Impure InAs at High Temperatures†

By F. W. Sheard‡
Cavendish Laboratory, Cambridge

[Received April 5, 1960]

Abstract

The addition of impurities affects both the lattice and electronic thermal conductivities of a semiconductor. At high temperatures the lattice resistance is increased by an amount independent of temperature: for the small concentrations normally present in semiconductors the impurity resistance can be derived very simply from the variational principle. The electronic contribution is normally obtained from the electrical conductivity via a Lorentz number. For a degenerate electron gas assuming polar scattering dominates an approximate calculation shows that at high temperatures the Lorentz number can be considerably reduced below the 'standard' value $\mathscr{L}_0=(\pi^2/3)(k/e)^2$. These theoretical calculations do not completely agree with the observed conductivity of impure InAs between 300 and 700°K (Stuckes 1960). The disagreement is attributed to the electronic contribution. To give agreement the Lorentz number would have to be reduced further but the precise amount is uncertain owing to experimental errors.

§ 1. Introduction

The addition of electrically active impurities to a semiconductor changes both the lattice and electronic thermal conductivities. The lattice conductivity is decreased owing to the additional phonon scattering while the extra conduction electrons increase the electronic contribution. These effects are qualitatively understood but it is nevertheless desirable to study them quantitatively for particular materials.

An absolute calculation of the electronic thermal conductivity would require knowledge of the conduction band structure which is so far only known for Ge, Si and InSb. Instead, using a simple model, one calculates the Lorentz number $\mathscr{L}=\kappa_e/\sigma T$, which at high temperatures will not be painfully sensitive to the details of band structure. Then from the measured electrical conductivity σ the electronic thermal conductivity κ_e is obtained.

However there is often doubt concerning the electron scattering mechanism. At high temperatures and in elemental semiconductors scattering by acoustic modes is likely to dominate. But in compound semiconductors the interaction of the electrons with the electric polarization of the optical modes of the lattice may be stronger and polar scattering may dominate.

† Communicated by the Author.
‡ Now at Physics Department, University of Nottingham.

Since the energy of an optical phonon can span a large part of the electron distribution such scattering is not describable by a simple relaxation time. A crude calculation of the Lorentz number for the case of a degenerate electron gas is given below. It is found that even at temperatures close to the optical mode temperature Θ_0, $\mathscr{L}$ can be considerably below the standard value $\mathscr{L}_0 = (\pi^2/3)(k/e)^2$ valid for elastic scattering. Thus estimates of the heat transport in degenerate compound semiconductors may be considerably in error if they rely on the standard Lorentz number.

The scattering of phonons by impurities is well understood but there are difficulties in the calculation of the thermal resistance from the phonon free path. The magnitude of the impurity resistance at high temperatures is discussed in § 3.

Finally the recent data on heavily doped InAs (Stuckes 1960) are analysed.

§ 2. The Lorentz Number for Polar Scattering

The interaction of an electron of wave vector $\mathbf{k}$ with the electric polarization caused by an optical phonon $\mathbf{q}$ leads to a transition probability

$$\mathcal{Q}_{\mathbf{k},\mathbf{q}}{}^{\mathbf{k}'} \propto \frac{1}{q^2}\delta_{\mathbf{k}+\mathbf{q},\mathbf{k}'}\delta(\mathscr{E}_{\mathbf{k}} + \hbar\omega_l - \mathscr{E}_{\mathbf{k}'}); \quad . \quad . \quad . \quad . \quad . \quad (1)$$

$\mathbf{k}'$ being the wave vector of the scattered electron and ω_l the frequency of the longitudinal optical modes (Ehrenreich 1957). The factor of proportionality need not concern us since the Lorentz number, being the ratio of the thermal and electrical conductivities, is independent of the magnitude of the transition rate.

To take account of the change in energy of an electron during a collision the variational method of calculation must be used. It was in this way that Howarth and Sondheimer (1953) obtained the electrical resistance and thermopower. We shall use the formulation in terms of entropy production (Ziman 1960, p. 280) and indicate only the calculation of the thermal resistivity W.

The relevant equation is

$$W = \frac{T^2 \dot{S}_{\text{scatt}}}{\mathbf{U}^2}, \quad . \quad . \quad . \quad . \quad . \quad . \quad . \quad . \quad (2)$$

where

$$\dot{S}_{\text{scatt}} = \frac{1}{kT^2}\int\int\int (\Phi_{\mathbf{k}} + \Phi_{\mathbf{q}} - \Phi_{\mathbf{k}'})^2 f_{\mathbf{k}}{}^0 n_{\mathbf{q}}{}^0 (1 - f_{\mathbf{k}'}{}^0)\, \mathcal{Q}_{\mathbf{k},\mathbf{q}}{}^{\mathbf{k}'} \mathbf{dk}\, \mathbf{dq}\, \mathbf{dk}' \quad (3)$$

is the rate of entropy production due to scattering processes, and

$$\mathbf{U} = \int \mathbf{v}_{\mathbf{k}}(\mathscr{E}_{\mathbf{k}} - \zeta)\Phi_{\mathbf{k}}\left(-\frac{\partial f_{\mathbf{k}}{}^0}{\partial \mathscr{E}_{\mathbf{k}}}\right)\mathbf{dk} \quad . \quad . \quad . \quad . \quad . \quad (4)$$

is the heat current for the state of the system where the deviation from the equilibrium distribution function is

$$f_{\mathbf{k}} - f_{\mathbf{k}}{}^0 = -\Phi_{\mathbf{k}}\left(\frac{\partial f_{\mathbf{k}}{}^0}{\partial \mathscr{E}_{\mathbf{k}}}\right).$$

$\Phi_{\mathbf{q}}$ is likewise the deviation of the phonon system from equilibrium.

The variational principle assures us that W takes its minimum value when $\Phi_{\mathbf{k}}$, $\Phi_{\mathbf{q}}$ are solutions of the corresponding transport equations subject to the subsidiary condition that the electric current in the system is zero. Thus guessing suitable solutions yields a good approximation to the thermal resistance.

Making the usual assumption that $\Phi_{\mathbf{q}}=0$ we take for the electron distribution in the presence of a thermal gradient along a direction $\mathbf{u}$,

$$\Phi_{\mathbf{k}} \propto (\mathscr{E}_{\mathbf{k}}-\zeta)\mathbf{k}\,.\,\mathbf{u}, \qquad \ldots\ldots\ldots \quad (5)$$

which to a good approximation satisfies the condition of zero electric current.

The evaluation of (3) using (1) and (5) requires an integration over $\mathbf{q}$. This is performed as in the calculation by Ziman (1960, p. 434) of the mobility in the non-degenerate limit. The final integration over $\mathbf{k}$-space is converted into one over the energy $\mathscr{E}$ of the state $\mathbf{k}$ assuming simple parabolic band structure: neglecting the proportionality factors in (1) and (5) we obtain

$$\dot{S}_{\text{scatt}} = \frac{n^0}{4\pi^2 kT^2}\cdot\frac{2m^{*3}}{3\pi^2\hbar^6}\int\left\{2\mathscr{E}\sqrt{\left(1+\frac{\hbar\omega_l}{\mathscr{E}}\right)}(\mathscr{E}-\zeta)(\mathscr{E}-\zeta+\hbar\omega_l)\right.$$
$$\left.+(\hbar\omega_l)^2(2\mathscr{E}-\zeta+\hbar\omega_l)\ln\left(\frac{\sqrt{[1+(\hbar\omega_l/\epsilon)]}+1}{\sqrt{[1+(\hbar\omega_l/\epsilon)]}-1}\right)\right\}f_{\mathbf{k}}{}^0(1-f_{\mathbf{k}'}{}^0)\,d\mathscr{E}, \qquad \ldots \quad (6)$$

where n^0 is the Bose–Einstein distribution for the phonons.

The energy $\mathscr{E}$ of an electron is measured from the bottom of the conduction band so that the limits of integration are $\mathscr{E}=0$ and ∞. Using the variable $x=(\mathscr{E}-\zeta)/kT$ the lower limit becomes $-\zeta/kT$ but may be replaced by $-\infty$ with negligible error if the gas is sufficiently degenerate. The integrals are evaluated by expanding the integrand, apart from the factor $f_{\mathbf{k}}{}^0(1-f_{\mathbf{k}'}{}^0)$, in powers of $\hbar\omega_l/\zeta$ and retaining only the lowest powers to give a non-zero result (Howarth and Sondheimer 1953). Defining $\xi=\zeta/kT$, $\alpha=\hbar\omega_l/kT$, (6) can be expressed in terms of the two integrals evaluated below:

$$\mathscr{I}_1=\int x(x+\alpha)(x+\xi)\sqrt{\left(1+\frac{\alpha}{x+\xi}\right)}\frac{1}{(1+e^{-x})(e^x+e^{-\alpha})}\,dx$$
$$=\frac{\xi\alpha}{(1-e^{-\alpha})}\left(\frac{\pi^2}{3}-\frac{\alpha^2}{6}\right),$$

$$\mathscr{I}_2=\int\alpha^2(2x+\xi+\alpha)\ln\left(\frac{\sqrt{[1+(\alpha/x+\xi)]}+1}{\sqrt{[1+(\alpha/x+\xi)]}-1}\right)\frac{1}{(1+e^{-x})(e^x+e^{-\alpha})}\,dx$$
$$=\frac{\alpha^3\xi}{(1-e^{-\alpha})}\ln\left(\frac{4\xi}{\alpha}\right).$$

Finally

$$\dot{S}_{\text{scatt}}=\frac{n^0}{4\pi^2kT^2}\cdot\frac{4m^{*3}}{3\pi^2\hbar^6}(kT)^4\frac{\xi\alpha}{(1-e^{-\alpha})}\left\{\frac{\pi^2}{3}-\frac{\alpha^2}{6}+\frac{\alpha^2}{2}\ln\left(\frac{4\xi}{\alpha}\right)\right\}. \qquad (7)$$

After a little manipulation the thermal current is found to be

$$|\mathbf{U}| = \frac{(kT)^2(2m^*\zeta)^{3/2}}{9\hbar^4}, \quad \ldots \ldots \quad (8)$$

provided ζ is measured from the bottom of the conduction band.

In our notation the electrical resistance, calculated for the lowest order trial function $\Phi_{\mathbf{k}} = \mathbf{k} \cdot \mathbf{u}$, comes out to be

$$\rho = \frac{n^0}{4\pi^2 kT} \cdot \frac{4m^{*3}}{3\pi^2\hbar^6}(kT)^2 \frac{\xi\alpha}{(1-e^{-\alpha})} \Big/ \frac{e^2(2m^*\zeta)^3}{9\pi^4\hbar^8}. \quad \ldots \quad (9)$$

At high temperatures the behaviour of the electrical and thermal resistivities is given quite reliably by these formulae: σ is inversely proportional to T while κ_e approaches a constant value. But they are only qualitatively true at low temperatures where better trial functions are needed to give any accuracy.

The magnitude of the Lorentz number follows from (7), (8) and (9):

$$\mathscr{L} = \frac{\rho}{WT} = \frac{\mathscr{L}_0}{1 + \frac{3}{2\pi^2}\left(\frac{\Theta_0}{T}\right)^2 \left\{\ln\left(\frac{4\zeta}{\hbar\omega_l}\right) - \frac{1}{3}\right\}}. \quad \ldots \quad (10)$$

It is the deviation from the high temperature limit, $\mathscr{L} \to \mathscr{L}_0$, that concerns us. This arises because of the 'vertical transitions' in which an electron is scattered vertically through the Fermi surface by a phonon of small wave number. Such processes contribute strongly to the thermal resistance because of the considerable energy change $\hbar\omega_l$ involved, but add very little to the electrical resistance owing to the small angle of scatter. Hence the Lorentz number is reduced below the value $\mathscr{L}_0$ valid for elastic collisions. But at sufficiently high temperatures the width of the Fermi surface, kT, is much greater than $\hbar\omega_l$ and the collisions are effectively elastic.

§ 3. Lattice Conduction at High Temperatures

We shall now study how the lattice conductivity is limited by the various phonon scattering mechanisms paying particular attention to the effects of impurities.

Phonon–phonon U-processes provide most of the thermal resistance and a crude estimate of this has been given by Leibfried and Schlömann (1954):

$$W_U = \frac{10\pi^3}{3(4)^{1/3}}\left(\frac{\hbar}{k}\right)^3 \frac{\gamma^2}{M\Theta^2\delta}\left(\frac{T}{\Theta}\right), \quad \ldots \ldots \quad (11)$$

where M is the average mass, δ^3 the average volume per atom and γ is the Grüneisen ratio. They did not consider the different types of U-process in detail and this, with many other approximations, makes (11) only reliable to a factor of 2 or 3.

Adding substitutional impurities produces additional phonon scattering the cross section depending almost entirely on the mass difference ΔM between the impurity and the atom normally occupying the lattice site.

Other effects due to the accompanying strain field are small. The mean free path $\Lambda_{\mathbf{q}}$ for phonons of wave number q is given by (Berman *et al.* 1956),

$$\frac{1}{\Lambda_{\mathbf{q}}} = \frac{q^4}{4\pi} n_s \left(\frac{\Delta M}{\mathscr{D}}\right)^2, \quad \ldots \ldots \quad (12)$$

where there are n_s scattering centres per unit volume in a medium of average density $\mathscr{D}$.

To obtain the thermal resistance we must average this quantity over the whole lattice spectrum taking account of the mutual interactions of the phonons by N-processes and U-processes. When N-processes outweigh the effects of impurity scattering and completely dominate the phonon distribution a simple formula can be obtained (Ziman 1960, p. 308). It derives from the variational principle and as such gives an upper limit to the thermal resistance. Within this approximation the resistances due to U-processes and impurity scattering are additive the latter being expressed as a harmonic average over the mean free path:

$$W_i = \frac{3}{C^2} \int \frac{C_{\mathbf{q}}}{\Lambda_{\mathbf{q}} v_{\mathbf{q}}} \mathbf{dq}, \quad \ldots \ldots \quad (13)$$

where $C_{\mathbf{q}}$ is the contribution of modes of wave vector $\mathbf{q}$ to the total heat capacity C and $v_{\mathbf{q}}$ is the phonon group velocity.

At low temperatures this formula cannot be used: for, the number of N-processes occurring is limited by selection rules and in most solids the scattering by naturally occurring isotopes is sufficient to influence the phonon distribution. Even for small isotopic content the observed resistance can be many times smaller than the variational limit (13). However a more general calculation, in which both N-processes and impurity scattering were allowed to fix the form of the phonon distribution, has given good agreement with experiment over wide ranges of impurity concentration (Berman *et al.* 1959). The theory of this is now well understood.

At high temperatures N-processes are much more common especially at the higher phonon frequencies. Equation (13) will therefore hold under less stringent conditions than required for low temperatures. A simple Debye model for the solid gives

$$W_i = \frac{\delta^3}{kv\Lambda_D} \mathscr{J}_8\left(\frac{\Theta}{T}\right) \Big/ \frac{\Theta}{T}\left\{\mathscr{J}_4\left(\frac{\Theta}{T}\right)\right\}^2 : \quad \ldots \ldots \quad (14)$$

Λ_D is the mean free path for a phonon of the Debye frequency $k\Theta/\hbar$, and v is an average sound velocity. $\mathscr{J}_n(x)$ is the standard transport integral,

$$\int_0^x \{z^n e^z/(e^z-1)^2\}\, dz,$$

which has been extensively tabulated (National Bureau of Standards 1959). This formula predicts that for $T \gtrsim 0{\cdot}6\Theta$, W_i is nearly constant; since we are only interested in temperatures greater than Θ we can write

$$W_i = \frac{3\delta^3}{7kv\Lambda_D}, \quad T \gtrsim \Theta. \quad \ldots \ldots \quad (15)$$

Finally expressing the sound velocity in terms of the Debye temperature and introducing the average mass per atom M we have from (12)

$$W_i = \frac{9\pi}{14}(6\pi^2)^{1/3}\frac{\hbar}{k^2}\frac{\delta^4}{\Theta}n_s\left(\frac{\Delta M}{M}\right)^2. \quad . \quad . \quad . \quad . \quad (16)$$

Unfortunately the available experimental evidence refers to such large concentrations of imperfections that we are unable to verify (16) in detail. The measurements of Geballe and Hull (1958) on normal and isotopically pure Ge have shown clearly that the additional resistance is independent of temperature for $T > \Theta$, but the observed magnitude is five times smaller than predicted by (16). For a Ge alloy containing 10% Si (Steele and Rosi 1958) the isotope resistance is some twenty-five times smaller. But for these specimens this is not really surprising since when they are taken to low temperatures ($\Theta/10$) the variational limit (13) is too large by factors of about 30 and 130 respectively (see Berman *et al.* 1959).

Use of the simple formula (13) is therefore limited to small impurity concentrations but for a particular concentration it is a better approximation at high than at low temperatures. For semiconductors where concentrations are indeed small it is likely to be quite accurate. To derive a formula for the high-temperature impurity resistance at arbitrary concentrations would be difficult; for the U-processes, which can be neglected at low temperatures, would have to be taken explicitly into account.

A formula similar to (16) but with a smaller numerical coefficient has been given by Ambegaokar (1959). He assumes that at high temperatures the phonon spectrum is dominated by U-processes, described by an appropriate relaxation time, upon which isotope scattering is a small perturbation. This is incorrect, for accompanying the U-processes there must be more than an equal number of N-processes which cannot be taken into account by simply adding reciprocal relaxation times. By treating the N-processes properly (Klemens 1958, p. 32, Callaway 1959) one arrives by a slightly different method at (16) again.

In an n-type semiconductor the conduction electrons can also scatter phonons and contribute to the lattice resistivity. However, a rough estimate shows the effect to be negligible for the impure InAs sample considered in the next section.

§ 4. The Thermal Conductivity of Impure InAs

To calculate the thermal transport in heavily doped InAs we need, apart from the measured electrical conductivity, estimates of the Fermi level, the optical mode temperature and the Debye temperature.

A knowledge of the melting point T_M, density $\mathscr{D}$ and average atomic weight A can be used to estimate the Debye temperature from the Lindemann melting formula

$$\Theta = BT_M^{-1/2}A^{-5/6}\mathscr{D}^{1/3}. \quad . \quad . \quad . \quad . \quad . \quad . \quad (17)$$

The value 200 taken for B was the mean of values calculated from the known properties of Si and Ge. This gave $\Theta = 280°\text{K}$.

The optical mode energy has not been determined very accurately (Picus *et al.* 1959, Ehrenreich 1957) and we shall simply take the round figure of 350°K for Θ_0.

Since intrinsic InAs is weakly degenerate at room temperature, a sample containing 10^{19} donor impurities per cm^3 will be highly degenerate. With an effective mass of $0{\cdot}064m_e$ (Welker and Weiss 1956) and a parabolic conduction band the Fermi energy would be 0·26 ev. However, comparison with InSb (Ehrenreich 1957, 1959) suggests the conduction band is appreciably non-parabolic, having a greater density of states, which would lower the calculated Fermi level.

Fig. 1

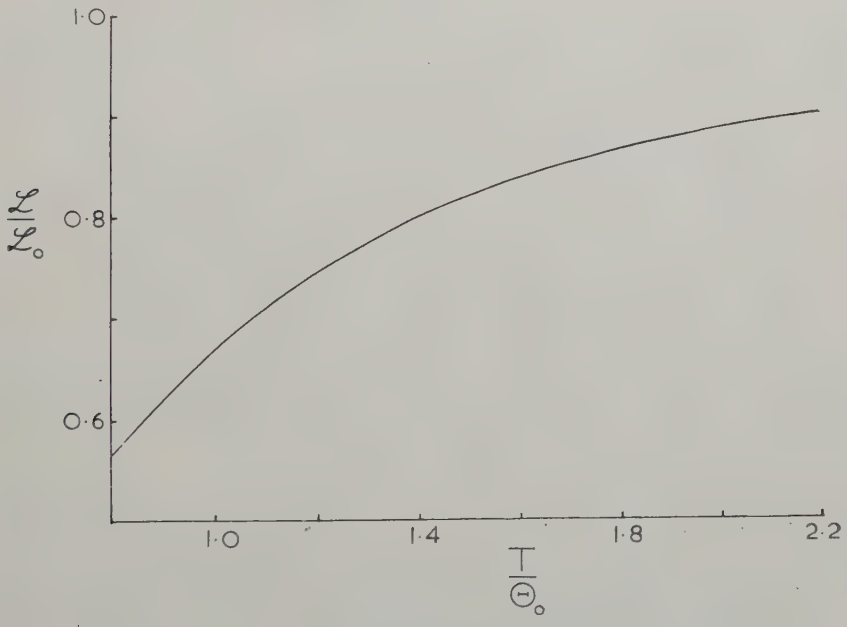

Lorentz number for polar scattering in a degenerate electron gas: $\zeta/\hbar\omega_l = 9$.

These plausible values can now be used to calculate the effects of the impurities on the electronic and lattice thermal conductivities of InAs.

The electronic contribution follows immediately from (10) with $(\zeta/\hbar\omega_l) \sim 9$, for which the behaviour of the Lorentz number is shown in fig. 1. The reduction below the asymptotic value $\mathscr{L}_0$ is surprisingly large: at $T = \Theta_0$, $\mathscr{L}/\mathscr{L}_0 \sim 0{\cdot}67$.

The extra lattice resistance is given by (16) evaluated for a concentration of 10^{19} substitutional sulphur atoms per cm^3: the result is $W_i = 0{\cdot}43$ cal^{-1} cm sec °K. In order to justify our use of the variational limit we look at the ratio of the calculated W_i to the observed Umklapp resistance at

$T = \Theta$, $W_i/W_U(\Theta)$, which clearly reflects the relative strengths of impurity scattering and phonon–phonon scattering. In the experiments previously mentioned on Ge and a Ge–Si alloy it is about 0·5 and 25 respectively. But for the InAs sample $W_i/W_U(\Theta)$ is much smaller ($\sim\frac{1}{30}$) thus justifying the assumption that the phonon system is dominated by N-processes and only slightly perturbed by the impurity scattering.

We could now compute theoretically the total thermal conductivity of the impure InAs and compare with experiment. This would involve using the very crude estimate (11) of W_U and the results would therefore not be of great significance. The Leibfried–Schlömann estimate has in any case been thoroughly discussed elsewhere (Klemens 1958, p. 46). Since our interest lies with the relatively small effects of the impurities we shall take W_U from experiment and avoid the numerical uncertainties in (11).

Table 1. Electronic and lattice contributions to the thermal conductivity of pure InAs ($n = 3 \times 10^{16}$)

T°K	$\kappa_{expt}^{(p)}$	$\kappa_e^{(p)}$	$\kappa_L^{(p)}$	W_U
300	0·0640	0·0004	0·0636	15·72
400	0·0448	0·0006	0·0442	22·60
500	0·0335	0·0010	0·0325	30·80
600	0·0280	0·0025	0·0255	39·20
700	0·0250	0·0045	0·0205	48·80

Unit of conductivity: cal cm^{-1} sec^{-1} $°K^{-1}$.

Table 1, taken from Stuckes (1960), summarizes the data for a fairly pure InAs sample (3×10^{16} donors cm^3) from which W_U was obtained in the temperature range 300 to 700°K. The electronic thermal conductivity $\kappa_e^{(p)}$ was calculated using the relaxation time approximation and Boltzmann statistics: since it is small the error in the lattice conductivity $\kappa_L^{(p)}$ is unlikely to be large.

Our estimate of the total conductivity of the impure specimen is thus obtained by the following algebraic manipulations: the superscripts (p) and (i) refer to the words pure and impure.

$$\left.\begin{aligned} \frac{1}{W_U} &= \kappa_L^{(p)} = \kappa_{expt}^{(p)} - \kappa_e^{(p)}, \\ \frac{1}{\kappa_L^{(i)}} &= W_L^{(i)} = W_U + W_i, \\ \kappa_{total}^{(i)} &= \kappa_L^{(i)} + \kappa_e^{(i)}. \end{aligned}\right\} \quad \ldots \quad (18)$$

The result is given in table 2.

The last two columns show that there is a discrepancy which increases with temperature becoming quite large at the highest temperature. There are obviously four possible sources of this disagreement, i.e. W_U, W_i, $\kappa_e^{(i)}$, $\kappa_{expt}^{(i)}$; but what is the relative significance of each in producing the final discrepancy?

Firstly, experimental errors are by no means negligible. The measured conductivities are only accurate to 3% at the lower temperatures and 5% at the higher temperatures in the table (Stuckes 1960). At 300°K this could account for more than half the difference $\kappa_{total}^{(i)} - \kappa_{expt}^{(i)}$. At 700°K W_U also includes errors in $\kappa_e^{(i)}$ and about a third of the discrepancy could be explained in this way. We are left with possible errors in the theoretical estimates of W_i, $\kappa_e^{(i)}$ with which to explain the remainder.

Table 2. Theoretical estimate of total thermal conductivity of impure InAs ($n = 10^{19}$).

T°K	$W_L^{(i)}$	$\kappa_L^{(i)}$	$\kappa_e^{(i)}$	$\kappa_{total}^{(i)}$	$\kappa_{expt}^{(i)}$
300	16·15	0·0619	0·0072	0·0691	0·0630
400	23·03	0·0434	0·0111	0·0545	0·0470
500	31·23	0·0320	0·0142	0·0462	0·0377
600	39·63	0·0252	0·0165	0·0417	0·0320
700	49·23	0·0203	0·0182	0·0385	0·0285

Unit of conductivity: cal cm^{-1} sec^{-1} $°K^{-1}$.

The value deduced for the impurity resistance is reliable as far as the Debye model applies to InAs. It is a variational estimate and as such can only be reduced by more accurate calculation using the same model. A more realistic model, or the presence of other imperfections in the impure sample, could possibly lead to a larger W_i. However, if the source of the remaining discrepancy is in the impurity resistance, this would need to be strongly temperature dependent. At the highest temperature it would have to be some fifty times the value previously calculated. This is in flat contradiction to theory of § 3 and the experiments of Geballe and Hull. An explanation invoking a temperature dependent impurity resistance is therefore to be rejected. One can more plausibly tamper with the magnitude of W_i; at 300°K, where the electronic contribution $\kappa_e^{(i)}$ is of least importance, only multiplication by two is needed to bring about the required agreement.

At the higher temperatures, where $\kappa_e^{(i)}$ is important, the discrepancy between theory and experiment persists. It would not however be surprising if our calculation of $\kappa_e^{(i)}$ were wrong. Even the assumption of polar scattering is suspect for the dominant scattering mechanism in InAs has not been definitely established. Since the phonon scattering cross-section is known accurately no such doubts exist about W_i; only its magnitude is a little uncertain.

Suppose for example that we accept the latter calculation; the electronic heat transport can then be estimated from experiment according to

$$\kappa_e^{(i)}(\text{estd}) = \kappa_{\text{expt}}^{(i)} - \frac{1}{W_U + W_i}, \quad . \quad . \quad . \quad . \quad . \quad (19)$$

and compared directly with theory. This final comparison is made in table 3 and illustrated in fig. 2. The curve marked 'elastic scattering' is the result of using the standard Lorentz number $\mathscr{L}_0$. There is considerable uncertainty in the experimental curve. The dotted lines E indicate the limits to which it could be raised by a favourable combination of experimental errors. It thus appears that the reduction in the Lorentz number afforded by polar scattering is not sufficient to account for the experimental results.

Table 3. Comparison of estimated κ_e for impure InAs with theory

T°K	$\kappa_L^{(i)}$	$\kappa_{\text{expt}}^{(i)}$	$\kappa_e^{(i)}$ (estimated)	$\kappa_e^{(i)}$ (polar)	$\kappa_e^{(i)}$ (elastic)
300	0·0619	0·0630	0·0011	0·0072	0·0121
400	0·0434	0·0470	0·0036	0·0111	0·0153
500	0·0320	0·0377	0·0057	0·0142	0·0176
600	0·0252	0·0320	0·0068	0·0165	0·0193
700	0·0203	0·0285	0·0082	0·0182	0·0205

Unit of conductivity: cal $\text{cm}^{-1}\,\text{sec}^{-1}\,°\text{K}^{-1}$.

Unfortunately the simplifications made in deriving this formula will not provide an excuse for reducing the Lorentz number still further. Briefly they are:

(1) Electron screening: This reduces the transition probability (1) especially at the lower phonon frequencies (Ehrenreich 1959). Vertical transitions, which only contribute strongly to the thermal resistance, are not so frequent and the Lorentz number is consequently increased.

(2) Trial functions: Only the simplest possible were used in the calculation. The electrical resistance is given accurately (Howarth and Sondheimer 1953) but the thermal conductivity is more sensitive to the balance of the electron system and needs a larger correction. But κ_e is thereby increased and so also is $\mathscr{L}$.

(3) Partial degeneracy: The electron gas may not be completely degenerate as assumed. At temperatures sufficiently high for the relaxation time approximation to be valid a partially degenerate gas has a Lorentz number slightly smaller than $\mathscr{L}_0 = 3{\cdot}29(k/e)^2$, and tending

towards the value $3(k/e)^2$ for a non-degenerate gas. This same trend will be observed at rather lower temperatures but the decrease in $\mathscr{L}$ is likely to be quite small.

(4) Band structure: We do not expect the actual band structure of InAs to greatly influence the formula for $\mathscr{L}$. The position of the Fermi level also depends on the model used but it appears logarithmically so that only serious misplacement would affect the magnitude of $\mathscr{L}$.

Fig. 2

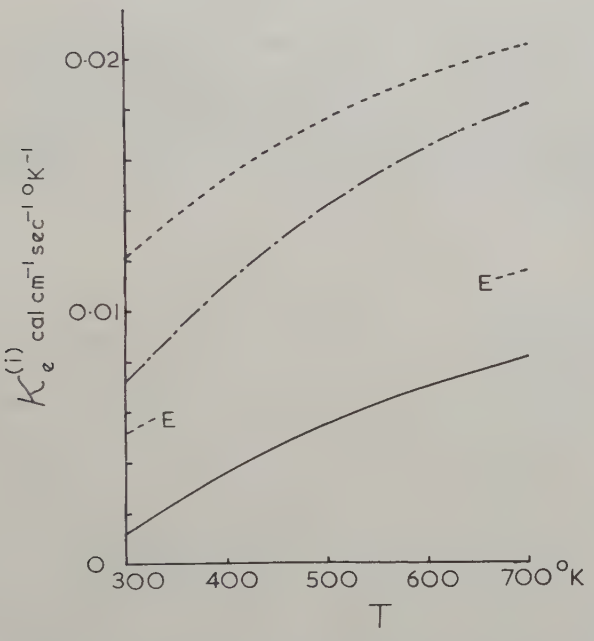

Electronic thermal conductivity of impure InAs.

———— estimated from experiment.
— — — — polar scattering.
– – – – – – – elastic scattering.

Experiments of greater accuracy are desirable in order to clarify the position by defining the precise reduction in the Lorentz number. Nevertheless it is clear that the electron scattering mechanism in InAs is inelastic at high temperatures.

Acknowledgments

I wish to express my thanks to Dr. J. M. Ziman for his helpful advice and to Miss A. D. Stuckes for a copy of her paper before publication. I am also indebted to Industrial Distributors (1946) Ltd., for a research grant.

References

Ambegaokar, V., 1959, *Phys. Rev.*, **114,** 488.

Berman, R., Foster, E. L., and Ziman, J. M., 1956, *Proc. roy. Soc.* A, **237, 344.**

Berman, R., Nettley, P. T., Sheard, F. W., Spencer, A. N., Stevenson, R. W. H., and Ziman, J. M., 1959, *Proc. roy. Soc.* A, **253,** 403.

Callaway, J., 1959, *Phys. Rev.*, **113,** 1046.

Ehrenreich, H., 1957, *J. Phys. Chem. Solids*, **2,** 131; 1959, *Ibid.*, **9,** 129.

Geballe, T. H., and Hull, G. W., 1958, *Phys. Rev.*, **110,** 773.

Howarth, D. J., and Sondheimer, E. H., 1953, *Proc. roy. Soc.* A, **219,** 53.

Klemens, P. G., 1958, *Solid State Physics*, Vol. 7 (New York: Academic Press).

Leibfreid, G., and Schlömann, E., 1954, *Nachr. Akad. Wiss. Göttingen*, IIa, No. 4, 71.

National Bureau of Standards, 1959, Circular No. 595.

Picus, G., Burnstein, E., Henwiss, B. W., and Hass, M., 1959. *J. Phys. Chem. Solids*, **8,** 282.

Steele, M. C., and Rosi, F. D., 1958, *J. appl. Phys.*, **29,** 1517.

Stuckes, A. D., 1960, *Phil. Mag.*, **5,** 84.

Welker, H., and Weiss, H., 1956, *Solid State Physics*, Vol. 3 (New York: Academic Press), p. 22.

Ziman, J. M., 1960, *Electrons and Phonons* (Oxford: Clarendon Press).

Nuclear Magnetic Resonance in β Brass†

By G. W. West
Division of Tribophysics,
Commonwealth Scientific and Industrial Research Organization,
University of Melbourne, Australia

[Received April 22, 1960]

Abstract

The nuclear magnetic resonance lines from β brass at room temperature have been studied as a function of composition and deformation. A simple model is proposed to explain the variation of intensity with composition. The Knight shift is 0·14%, independent of composition. Filing at room temperature eliminates the line from most specimens but it can be restored by annealing. Changes in line shape occur before, during, and after recrystallization.

§ 1. Introduction

The effects of deformation and composition on the ^{63}Cu resonance in copper and copper–zinc alloys have been studied by Bloembergen and Rowland (1953). They showed that in pure copper the components of the line due to the satellite transitions ($m = \frac{3}{2} \rightarrow \frac{1}{2}$, $-\frac{1}{2} \rightarrow -\frac{3}{2}$) can be almost eliminated by cold work but that there is no effect on the central component corresponding to the transition $m = \frac{1}{2} \rightarrow -\frac{1}{2}$. Furthermore, in cold-worked copper–zinc alloys they showed that the central component was unobservable when the zinc content exceeded 25%. They explained these effects in terms of quadrupole broadening but pointed out that if the composition was such that an ordered structure with cubic symmetry occurred, quadrupole broadening should be absent and a line would be expected. Following this idea, they looked for resonance from a β brass containing nearly 50% zinc. However, they could detect no resonance and suggested that ordering was not complete.

Since then resonance lines from β brass have been reported (West 1958). The present paper gives details of the variation of this resonance line with composition and with deformation and subsequent heat treatment.

§ 2. Experimental Details

The detecting apparatus was a conventional Pound–Knight–Watkins spectrometer operating at about 5·96 Mc/s and a Varian 12 in. electromagnet set at about 5250 gauss. The modulation amplitude was 3 gauss peak-to-peak and all resonance lines were obtained at room temperature.

The alloys were originally prepared from OFHC copper and pure zinc for another investigation (Clarebrough 1957). Their compositions are given in table 1.

† Communicated by W. Boas.

The copper–zinc equilibrium diagram (Raynor 1944) was used to determine the phase composition of each alloy. The composition of alloy C corresponds to the β phase boundary so that alloys C, D and E all contain β phase of the same composition. For alloy D approximately $\frac{8}{9}$ of the specimen volume should be β phase while for alloy E about $\frac{7}{9}$ should be. Metallographic examination showed that alloy A, after it had been annealed at 450°C for two hours and then slowly cooled in the furnace, contained a small amount of γ phase, estimated very approximately as 5%. These estimates of the amounts of the different phases present are necessary since in comparing the signals from different alloys it has been assumed that no signal was obtained from the copper atoms in α or γ phases.

Table 1. Zinc Content of Alloys

Alloy	Phases present	Atomic % zinc in alloy	Atomic % zinc in β phase
A	$\beta+\gamma$	50·05	49·5
B	β	47·64	47·64
C	β	46·15	46·15
D	$\alpha+\beta$	45·06	46·15
E	$\alpha+\beta$	43·14	46·15

The material for the resonance experiments was prepared by filing the alloys at room temperature and accepting only those particles which passed through a 160 mesh sieve. These particles were then placed for 5 min in a solution of stearic acid in benzene, washed and allowed to dry. By this treatment the particles were coated with an insulating layer which was stable at the annealing temperatures used. The specimens of brass consisted of 200 mg of powder held in glass tubes. A reference specimen of OFHC copper (99·96% Cu) was prepared in a similar manner but only particles which passed through a 300 mesh sieve were used. The reference specimen was annealed at 450°C for two hours. It contained 98·5 mg of copper, i.e. the same number of copper nuclei as would be present in 200 mg of an ideal copper-zinc alloy containing 50 atomic per cent zinc.

For all heat treatments up to 350°C the glass tubes containing the filings were immersed in silicone oil at the appropriate temperature for 5 min. For heat treatments above 350°C, in order to minimize loss of zinc, the filings were sealed in glass tubes under a pressure of argon of just less than one atmosphere and then placed in a furnace for the specified time.

§ 3. Experimental Results

3.1. *Effect of Composition*

Specimens of all compositions were annealed for two hours at 450°C and slowly cooled in the furnace. Table 2 shows relative integrated intensities, relative peak-to-peak heights of the derivative curves, and the line widths

as measured between peaks on the derivative curve. The values for the brass specimens have been normalized to correspond to specimens containing the same total number of nuclei in the β phase as would be present in 200 mg of an ideal copper–zinc alloy containing 50 atomic per cent zinc.

Table 2. Results for Annealed Copper and β Brass

Alloy	Copper	A	B	C	D	E
Relative integrated intensities	2·5	0·68	0·48	0·35	0·35	0·35
Relative peak-to peak heights	1	0·57	0·35	0·25	0·21	0·17
Line width (gauss)	6	3·3	3·5	4	4	4

The lines for specimens from alloys A, B, and C, annealed at 450°c for two hours, and for the reference copper specimen under the same resonance conditions are shown in fig. 1. The lines for D and E have peak heights as indicated in table 2 but are relatively larger in the tails than the line for C, so that the integrated intensities for C, D and E are approximately equal.

The lines from these annealed specimens are symmetrical and there is a slight broadening and a decrease in peak height as the copper content increases. In order to compare the shapes of the lines, the derivative curves for a specimen from alloy A and for the copper reference specimen have been replotted in fig. 2. The scales of both axes have been adjusted so that both lines have the same peak height and coincide at half peak height. It is clear that the curve from the brass specimen has a much larger tail than that from the copper specimen.

The lines from the brass specimens occur at a frequency 5·2 kc/s below that from the copper reference specimen and any variation of frequency with change in composition is less than 0·1 kc/s. Thus the Knight shift for ^{63}Cu is only 0·14% in β brass compared with 0·23% in pure copper. If these values are substituted in the Korringa (1950) relation the calculated spin-lattice relaxation time for copper is 0·37 that for brass.

The saturation curves for a specimen from alloy A and for the copper reference are shown in fig. 3. The ratio of relaxation times from these results is given by (Andrew 1955)

$$\frac{T_1(\text{copper})}{T_1(\text{brass})} = 0{\cdot}43\,\frac{T_2(\text{brass})}{T_2(\text{copper})},$$

where T_1 = spin–lattice relaxation time, and
T_2 = spin–spin interaction time.

For this to agree with the results calculated from the Korringa relation the spin–spin interaction times for copper and brass would need to be approximately equal.

Fig. 1

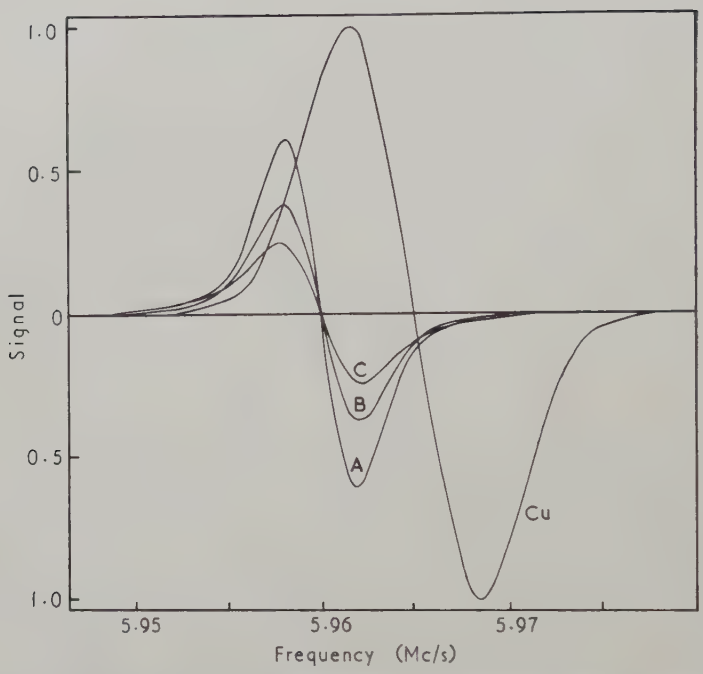

The derivatives of the ^{63}Cu resonance in β brass (alloys A, B, and C) and in pure copper.

Fig. 2

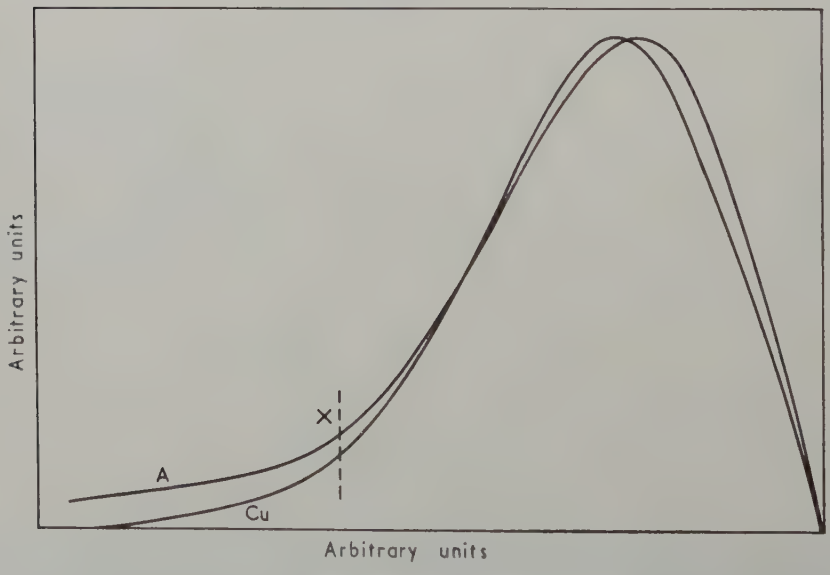

The line shapes of the ^{63}Cu resonance in β brass (50·05% zinc) and copper.

Fig. 3

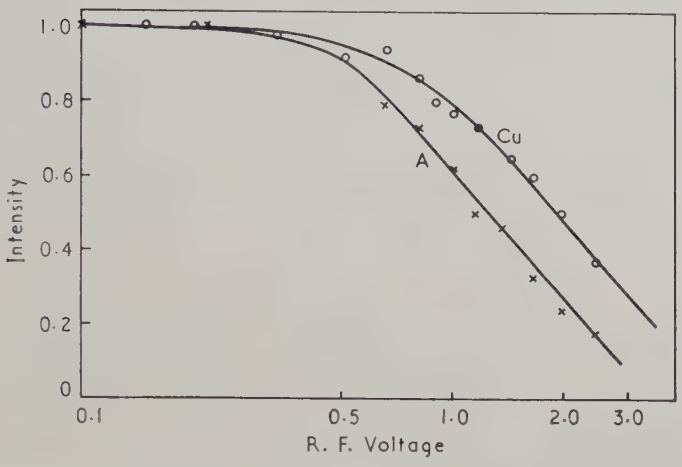

The saturation curves for the ^{63}Cu resonance in β brass and copper as a function of the radio frequency voltage across the specimen coil

○ ○ ○ Copper; × × × β brass (50·05% zinc).

Fig. 4

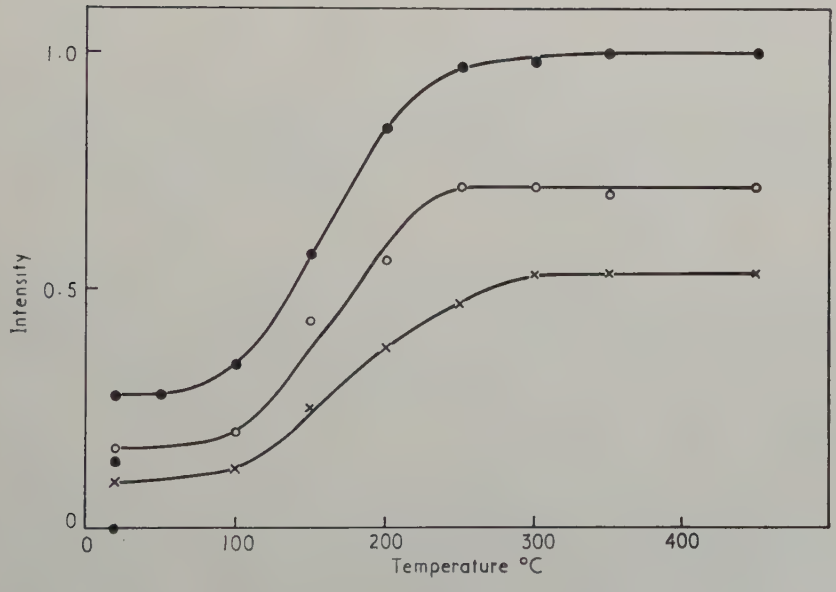

The variation of the peak-to-peak height of the derivative curve with annealing temperature for the ^{63}Cu resonance in β brass

. . . 47·64% zinc; ○ ○ ○ 46·15% zinc; × × × 45·06% zinc.

3.2. *Effect of Deformation and Annealing*

In one set of annealing experiments one specimen from each of alloys B, C, and D was filed and prepared as described in § 2. Two hours after filing, only alloy B gave an observable signal. However, after eight weeks at room temperature, the signal from alloy B had doubled in intensity and the other specimens gave observable signals. All specimens were then given 5 min annealing treatments at successively higher temperatures up to 350°C. The peak-to-peak height of the derivative curve as a function of annealing temperature is shown in fig. 4.

Fig. 5

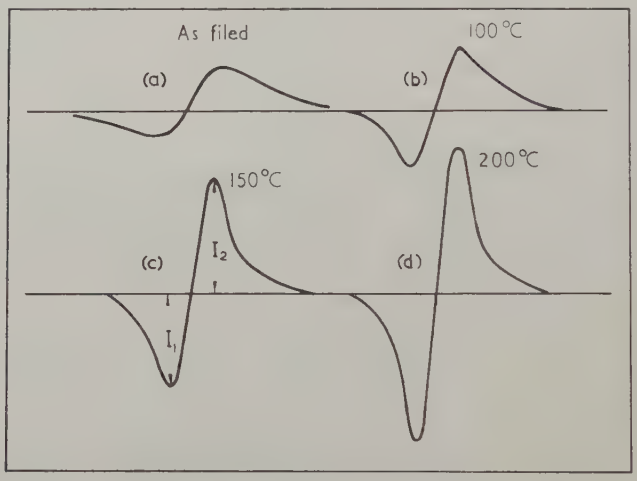

The variation of line shape with annealing temperature for the ^{63}Cu resonance in β brass (47·64%) zinc.

(*a*) as filed; (*b*) annealed at 100°C;
(*c*) annealed at 150°C; (*d*) annealed at 200°C.

In another set of annealing experiments, separate filed specimens of equal weight were annealed at various temperatures up to 450°C. The results from these agree with those from the first set and are also included in fig. 4. The lines for specimens from alloy B as filed and after annealing at 100°C, 150°C and 200°C are shown in fig. 5. Similar sets of curves are obtained from alloys C and D.

Table 3 shows the relative peak-to-peak heights of the derivative curves, the ratio of the peak values on the derivative curve (I_1/I_2 in fig. 5), and the line widths as measured between peaks for specimens from alloys B, C, and D as filed and after annealing at the temperatures shown. The points to be noted are (1) the steady increase in peak-to-peak height, even above 200°C, (2) the asymmetry of the lines which disappears after annealing at 200°C or above, (3) the steady decrease in line width on annealing up to 200°C.

X-ray back-reflection photographs of alloys B, C, and D were taken after filing and after annealing at 150°C, 200°C and 450°C. These showed that recrystallization became effectively complete between 100°C and 200°C.

Table 3. Results of Annealing Alloys B, C and D

Alloy		Filed	100°C	150°C	200°C	300°C	450°C
B	Peak-to-peak height	0·28	0·34	0·56	0·84	0·99	1·0
	Asymmetry I_1/I_2	0·7	0·8	0·8	1·0	1·0	1·0
	Line width (gauss)	6·0	4·5	3·7	3·5	3·5	3·5
C	Peak-to-peak height	0·17	0·20	0·44	0·56	0·72	0·72
	Asymmetry I_1/I_2	0·7	0·8	0·8	1·0	1·0	1·0
	Line width (gauss)	6·4	4·8	4·2	4·0	4·0	4·0
D	Peak-to-peak height	0·10	0·16	0·28	0·42	0·60	0·60
	Asymmetry I_1/I_2	0·7	0·8	0·8	1·0	1·0	1·0
	Line width (gauss)	8·0	5·6	4·8	4·0	4·0	4·0

§ 4. Discussion

4.1. *Effect of Composition*

In comparing the intensities of the resonance lines from different specimens, the following assumptions will be made:

(i) The integrated intensity is proportional to the number of copper nuclei contributing,

(ii) the satellite components have been eliminated from all lines from brass specimens, and

(iii) a nucleus will contribute to the resonance only if each of the first three shells of atoms surrounding it contains atoms of one type.

These assumptions are comparable to those used by Bloembergen and Rowland to explain their results in α brass, and as is shown below they provide a consistent explanation of the present results.

Suppose we have a fully ordered β brass containing $(N/2)\,(1+x)$ copper atoms and $(N/2)\,(1-x)$ zinc atoms. Then the $(N/2)a$-sites are occupied by copper atoms, and the $(N/2)b$-sites are occupied by $(N/2)\,(1-x)$ zinc atoms and $(N/2)x$ copper atoms. The eight nearest neighbours of each copper atom on a b-site will be copper and the probability that the eighteen next nearest neighbours (six in the second shell and twelve in the third) will

be all of the one type is $(1-x)^{18}+x^{18}$. Therefore, the contribution to the resonance from copper atoms on b-sites is $(N/2)x[(1-x)^{18}+x^{18}]$. Similarly the contribution from copper atoms on a-sites is $(N/2)[x^8+(1-x)^8]$. For β brass, the possible range of x is such that the only significant contribution comes from the term $(N/2)(1-x)^8$. This corresponds to copper atoms on a-sites with eight zinc atoms in the first surrounding shell and copper atoms filling the second and third shells. Therefore, the number of copper nuclei contributing to the resonance is $(N/2)(1-x)^8$ and it follows that the integrated intensities from alloys A, B, and C should be in the ratio 1 : 0·75 : 0·57. The experimental values shown in table 2 give this ratio as 1 : 0·7 : 0·5, i.e. within experimental error of the predicted ratio.

Since the copper reference specimen contains $N/2$ nuclei the ratio of the integrated intensity for brass to that for the central component of copper will be $(1-x)^8$. The integrated intensity of the central component for copper is 0·4 that of the total, i.e. 1·0 on the scale used in table 2. The integrated intensities should on this argument be 0·92, 0·69 and 0·53, for alloys A, B, and C respectively. The fact that the measured values are lower may be due to two causes. Firstly, the long tails on the β brass lines may have caused the intensities to be underestimated. Secondly, the alloys may not be fully ordered. If it is assumed that the discrepancy is entirely due to disorder, it can be shown that long-range order parameters of 0·98, 0·97 and 0·96 for alloys A, B, and C respectively give calculated intensities corresponding to those shown in table 2.

Referring now to the shape of the lines, the large tail on the line from β brass (see fig. 2) indicates that some of the nuclei have suffered appreciable second-order quadrupolar interaction so that their resonance signal is displaced well away from the centre of the line. However, since the central portion of the line is symmetrical this part must consist of undistorted central components from other nuclei. If the curve is divided at x into a central portion plus a tail, the number of nuclei in the central portion is about 70% of the number contributing to the resonance.

The frequency of the resonance in β brass appears to be independent of composition and the discussion above has suggested that each copper nucleus contributing to the resonance is surrounded by a shell of zinc atoms. Similarly, in α phase copper–zinc alloys, Bloembergen and Rowland found that the frequency of the resonance was independent of composition. They further suggested that a copper nucleus contributes to the resonance only if it is completely surrounded by at least two shells of copper atoms. The Knight shift observed in copper will then be characteristic of a copper atom surrounded by copper atoms, and that in β brass of a copper atom surrounded by zinc atoms in the first shell. Drain (1959) has shown that in the silver-cadmium system, where quadrupolar interactions are absent, the Knight shift decreases continuously as the cadmium content increases from zero to 50%. He suggests that if it were possible to eliminate quadrupolar interaction in the copper–zinc system the behaviour would be similar. The present results agree with this prediction.

4.2. *Effect of Deformation and Annealing*

The deformation produced by filing is sufficient to render the line unobservable for specimens with low zinc content (alloys C and D). This behaviour is in sharp contrast to that of copper and α brass where filing has no apparent effect on the central component. Since the strains must be of the same order of magnitude in the two sets of alloys, this implies that the tensor giving the electric field gradient in terms of the strain is much larger for β brass.

The recovery of intensity with time at room temperature indicates that an appreciable amount of atomic movement is taking place. However, all lines from deformed specimens are asymmetric and comparatively broad. Therefore, in these lines the central components are showing the effects of second-order strain broadening. Further, these effects persist on annealing at temperatures below 200°C, i.e. any atomic re-arrangements occurring during recovery are not sufficient to eliminate second-order broadening. However, on annealing at 200°C, i.e. on recrystallization, the return to a symmetrical line and a further reduction in width indicate that second-order broadening has been reduced. The continuing increase in peak-to-peak height and constant line width on annealing at temperatures above 200°C is probably due to an increase in the degree of order in the specimens.

It is possible that some of the change during recovery may be due to the phase transformation discovered by Massalski and Barrett (1957). They have shown that filing β brass at room temperature causes a change to the hexagonal close-packed phase. Such a change would destroy the cubic symmetry around the nucleus with consequent elimination of the resonance line. The line would reappear as the hexagonal close-packed phase reverted to the body-centred cubic phase. However, it is unlikely that all the change in intensity can be attributed to this cause since only small traces of the hexagonal close-packed phase were reported.

Acknowledgments

I would like to thank Mr. H. S. Voake for his valuable assistance throughout the whole of this investigation. I would also like to thank Mr. J. F. Nicholas and Mr. E. A. Faulkner for much helpful discussion and criticism.

References

Andrew, E. R., 1955, *Nuclear Magnetic Resonance* (Cambridge: University Press), p. 111.
Bloembergen, N., and Rowland, T. J., 1953, *Acta Met.*, **1**, 731.
Clarebrough, L. M., 1957, *Acta Met.*, **5**, 413.
Drain, L. E., 1959, *Phil. Mag.*, **4**, 484.
Korringa, J., 1950, *Physica*, **16**, 601.
Massalski, T. B., and Barrett, C. S., 1957, *Trans. Amer. Inst. min. (metall.) Engrs*, **209**, 455.
Raynor, G. V., 1944, *Annotated Equilibrium Diagram*, No. 3 (London: Inst. Metals).
West G. W., 1958, *Nature, Lond.*, **182**, 1436.

Some Magnetic Properties of the Ising Model†

By D. M. Burley
Mathematics Department, The University, Glasgow, W.2‡

[Received May 4, 1960]

Abstract

Two properties of the Ising model are considered. Firstly, by extrapolating appropriate series expansions, the spontaneous magnetization of a ferromagnet for three-dimensional lattices is obtained. From the results accurate values for the critical temperature are found. Secondly, the high temperature susceptibility of an antiferromagnet is derived from the approximation of Kikuchi. The resulting susceptibility curves show that for loose-packed lattices a maximum value occurs at a temperature slightly above the critical point, while for the close-packed lattices no such effect is obtained.

§ 1. Introduction

Two of the fundamental properties in magnetism are the appearance of the spontaneous magnetization of a ferromagnet in zero field, and the zero field susceptibility for both a ferromagnet and antiferromagnet. The first of these properties has been studied in detail on the Ising model for two-dimensional lattices, and explicit formulae have been obtained by Yang (1952) and Potts (1952). For the three-dimensional lattices the spontaneous magnetization has been evaluated for various approximate methods and Münster and Sagel (1956) have summarized many of the results, together with the results obtained by the series expansion method of Fuchs, for the equivalent problem of the phase boundary of regular solutions. For the simple cubic lattice, Wakefield (1951) evaluated the spontaneous magnetization by extrapolating the series expansion which he obtained by calculating a large number of terms in the partition function for the assembly and then calculating the spontaneous magnetization from the free energy (F) by the equation

$$I_0/I_\infty = \partial F/\partial H|_{H=0} \qquad \ldots\ldots (1)$$

where I_0 is the spontaneous magnetization in zero field at a temperature T, I_∞ is its value at absolute zero and H is the applied magnetic field. He then tried to extrapolate the resulting series. The convergence of this series is very slow in the critical region, and his method of extrapolation is doubtful there, particularly since he found that the magnetization dropped discontinuously to zero from a value of about 0·4. A better method of extrapolation will be applied and some more reliable results obtained.

† Communicated by the Author.

‡ Present address: Applied Mathematics Department, The University, Sheffield, 10.

The second quantity, the zero field susceptibility, has been studied in some detail for a ferromagnet by Domb and Sykes (1957). A more interesting problem, however, is to evaluate susceptibility for an antiferromagnet, since on the Ising model, with only nearest-neighbour interactions, a close-packed lattice has no completely ordered state and hence no cooperative transition ; also it will be shown that for loose-packed lattices the maximum value occurs not at the Néel temperature but at a temperature slightly above it. The approximate method of Kikuchi (1951) is used in the calculation of this paper. Sykes and Fisher (1958) have reported results of this nature and some detailed calculation has been given by Fisher (1959).

§ 2. Spontaneous Magnetization

The method of extrapolation used in this section follows closely the method used by Domb and Sykes (1956). They showed that the partition function per spin, $\Lambda(\mu, z)$, could be written in a series expansion, at low temperatures, as

$$\Lambda(\mu, z) = 1 + \mu f_1(z) + \mu^2 f_2(z) + \ldots \qquad (2)$$

where $\mu = \exp(-2mH/kT)$ and $z = \exp(-\epsilon/kT)$, m is the magnetic moment per spin and ϵ the interaction energy between nearest neighbours. The $f_r(z)$ in the expansion are just finite polynomials, which are listed for the various lattices by Domb and Sykes (1956).

Using (1) the spontaneous magnetization can be written in terms of these $f_r(z)$ as

$$I_0/I_\infty = \lim_{r\to\infty} (1 - 2C_r), \qquad (3)$$

where

$$C_r = \sum_{i=1}^{r} i f_i(z) \Big/ \sum_{i=0}^{r} f_i(z). \qquad (4)$$

For any given z and given lattice it is found that the numbers C_r vary in a smooth and convergent manner and that the extrapolation $r\to\infty$ can be made with confidence. For small z, a very good estimate can be obtained by plotting C_r against $1/r$ and extrapolating the resulting graph ; this method was found to be adequate for $T/T_c < 0{\cdot}8$ (where T_c denotes the critical temperature). For larger values of z, a more accurate method must be applied and it is essential that the polynomials $f_i(z)$ be calculated accurately to at least six figures for the various values of z in the critical region, since some differencing is employed. Fortunately a large amount of data on the $f_i(z)$ had been calculated on the digital computor and was kindly made available by Professor C. Domb. Where no data were available, the values were calculated, and from the $f_i(z)$ it is easy to compute the C_r of eqn. (4).

The method of extrapolation was chosen to cover as large a variation as possible and it was assumed that $\Delta C_r = C_r - C_{r-1}$ could be written in

the form $\Delta C_r = A/r^h$. For a given lattice and a fixed value of z, a series of values of h were obtained which were seen to approach a limit h^*, and using this value of h^*, a series of values of A were obtained which approached a value of A^*. If $f_0(z)$ to $f_p(z)$ were known for the given lattice the value of C_∞ was calculated from the equation:

$$C_\infty = C_p + A^* \sum_{r=p+1}^{\infty} 1/r^{h^*}. \quad \ldots\ldots (5)$$

Fig. 1

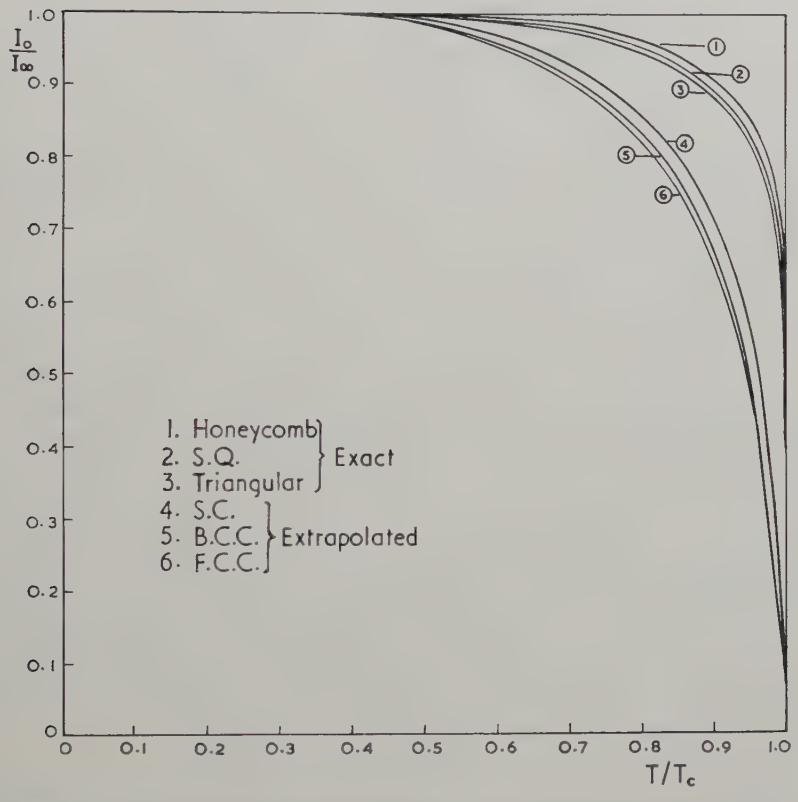

Graph of the spontaneous magnetization against reduced temperature.

In the critical region it was found that h^* was close to unity and since (5) is very sensitive to changes in h^* in this region, care had to be taken. An example of the method of calculation is given in Appendix I for the body-centred cubic lattice for the value $z^2 = 0{\cdot}529$. This value is very close to the critical point ($T/T_c = 0{\cdot}99$) and the possible error of extrapolation is at its maximum. The value of h^* chosen for this calculation was 1·26 and the limits between which h^* could vary are 1·24 and 1·30. The computed values of C_∞ for these extreme values are 0·248 and 0·200, and the value for $h^* = 1{\cdot}26$ is $C_\infty = 0{\cdot}227$. Thus the estimated

error in the critical region for the spontaneous magnetization is $\pm 0{\cdot}04$. For smaller values of z the estimated error decreases rapidly. The method was followed for the simple cubic (S.C.), body-centred cubic (B.C.C.) and face-centred cubic (F.C.C.) lattices and the results are shown in fig. 1 in comparison with the exact curves for the two-dimensional lattices; and the computed values for the three-dimensional lattices are given in Appendix II.

Since the Ising model treats spin as a classical property, quantitative agreement with experiment is not to be expected, but despite the considerable idealization of the model good qualitative agreement is obtained, the spontaneous magnetization curves going to zero at the critical temperature. The importance of the quantum nature of spin is shown well by the better quantitative agreement obtained at low temperatures from the spin wave treatment of the Heisenberg model (Dyson 1956). This work on the Ising model is important, nevertheless, on two counts. Firstly, the data obtained give a valuable yardstick by which more physically realistic models and approximate methods, used for the models, can be measured. Secondly, fig. 1 shows clearly that the dimensionality of the lattice is the most important feature to be considered and that the coordination number of the lattice only affects the fine structure of the curves.

For the two-dimensional lattices and approximate methods, for the Ising model, it is known that near the Curie point the spontaneous magnetization behaves like $I_0/I_\infty \sim A(T_c - T)^n$ and this is assumed to be the case for three-dimensional lattices also. The exact results for the two-dimensional lattices give $n = \frac{1}{8}$ and it would be extremely useful if n could be estimated for the three-dimensional lattices. In order to estimate its value, however, extremely accurate data must be obtained in the region $0{\cdot}98 < T/T_c < 1$. Such accurate results are not available from this work, but from the extrapolated curves of fig. 1 it appears certain that $n > \frac{1}{8}$. A comparison of these curves with those obtained from the Bethe and Kikuchi approximations indicates that n is between $\frac{1}{4}$ and $\frac{1}{2}$.

§ 3. Critical Points

The critical temperature associated with a given lattice is obtained by finding the value of z for which the spontaneous magnetization becomes zero. When the values of z_c obtained by Domb and Sykes (1956) were used it was found that, instead of vanishing, the spontaneous magnetization for the body- and face-centred cubic lattices remained at a value of about $0{\cdot}15$. Since the possible error was estimated to be $\pm 0{\cdot}04$ it was assumed that these critical values were inaccurate. Because the spontaneous magnetization curve is so steep near the Curie point, it is very sensitive to changes in T_c and hence a recalculation of the critical values from the data obtained in the previous section, produces accurate values.

The critical temperatures obtained by Domb and Sykes (1956) were obtained by extrapolation of the maximum of the low temperature specific heat. In a later paper, Domb and Sykes (1957) studied the high-temperature susceptibility and obtained approximations to the Curie temperature by estimating the radius of convergence of the series expansion in inverse powers of temperature. The results obtained in this paper are in close agreement with the present estimates, and a comparison is made in the table, where the various values of $t_c = kT_c/q\epsilon$ are presented.

Estimated Critical Values of $t_c = kT_c/q\epsilon$

Lattice	Domb and Sykes (1956)	Domb and Sykes (1957)	Present estimate
S.C.	0·748	0·752	0·749
B.C.C.	0·784	0·794	0·793
F.C.C.	0·805	0·816	0·815

The accuracy of the present estimates for the critical temperature were obtained by plotting the values for the spontaneous magnetization against z and considering the possible errors made in the extrapolation. It was found that the critical temperatures obtained were accurate to $\pm 0{\cdot}003$ and it may be observed that, for the simple cubic lattice, both the values of Domb and Sykes are within these limits.

§ 4. High-temperature Susceptibility

The particular interest in this quantity is that at temperatures well above the Curie point a magnet becomes paramagnetic and the zero field susceptibility (χ_0) obeys the Curie–Weiss law.

$$\chi_0 = \frac{C}{T \pm T_p}, \qquad \ldots\ldots\ldots \quad (6)$$

where T_p is the paramagnetic Curie temperature, the positive sign referring to an antiferromagnet and the negative sign to a ferromagnet. From the constant, C, information can be obtained about the Bohr magneton number and hence about the spin of the systems in the assembly. This constant is, therefore, of considerable interest experimentally and a theoretical reproduction of the behaviour, and a consideration of deviations from this behaviour are desirable.

On the Ising model, the ferromagnetic susceptibility has been studied in detail both from the Bethe approximation originally by Firgau (1942), and more recently by Domb and Sykes (1957) from a series expansion method. For the antiferromagnetic little has been attempted however.

Brooks and Domb (1951) calculated the susceptibility from series expansions for the simple quadratic lattice, but because of the difficulty of convergence near to the Néel point, they missed the essential feature of a maximum slightly above this point. The Bethe approximation also does not produce a maximum. In this case, the reason is linked to the fact that the approximation does not consider any closed configurations on the lattice and hence does not even differentiate between loose- and close-packed lattices. This difference is most important in the antiferromagnetic case and it is the closed configurations on a lattice which determine the behaviour of the assembly in the neighbourhood of the critical point.

The simplest method by which closed configurations can be taken into account, is by using the approximation of Kikuchi (1951). The notation and derivation of this approximation are rather long and in order to avoid reproducing Kikuchi's work, his notation will be followed exactly and his results assumed to be known. The method has to be extended a little to include the parameter $\mu = \exp(-2mH/kT)$, but the extension is trivial and modifies his equations only slightly. One of the variables (ξ_1) occurring in the approximation turns out to be exactly the magnetization of the assembly and consequently the susceptibility in zero field can be derived from the equation

$$\chi_0 = (I_\infty m/kT)(\partial\xi_1/\partial\mu)\big|_{\mu=1}. \qquad \ldots\ldots \quad (7)$$

On the Bethe approximation, which may be treated in Kikuchi's notation, the long-range order, ξ_1, and the short-range order, y_2, are the only independent variables to appear in the basic equations obtained for the approximation. The derivatives with respect to μ of these two quantities can then easily be calculated. At temperatures above the Curie point, and when the magnetic field is zero (i.e. $\mu = 1$) the basic equations can be solved explicitly as

$$\xi_1 = 0, \qquad y_2 = z/2(1+z).$$

Putting these values into the calculated value of $(\partial\xi_1/\partial\mu)\big|_{\mu=1}$ and using (7) gives the Firgau formula

$$\chi_0 = (I_\infty m/kT)\{qz - (q-2)\}^{-1}. \qquad \ldots\ldots \quad (8)$$

This, however, is not the susceptibility of an antiferromagnet but of a ferromagnet. In order to make the necessary conversion the simplest method is to use the variable $v = (1-z)/(1+z) = \tanh(\epsilon/2kT)$ and changing the sign ϵ just changes the sign of v. Applying this transformation to (8) gives

$$\frac{\chi_0\epsilon}{I_\infty m} = \frac{\tanh^{-1} v(1-v)}{1+(q-1)v}.$$

Since the long-range order, ξ_1, has been put explicitly equal to zero this formula is only valid above the Néel temperature, which occurs at the specific heat singularity, that is for $0 \leqslant v \leqslant 1/(q-1)$.

On the Kikuchi approximation the method follows very closely the method for the Bethe approximation, but this time two long-range order parameters, ξ_1 and ξ_2, appear, although it is still the quantity $\xi_1' = (\partial\xi_1/\partial\mu)|_{\mu=1}$ which is required in order to substitute into eqn. (7). From the basic equations obtained by the approximation, in the region above the Néel point and in zero field (i.e. $\mu = 1$ and $\xi_1 = \xi_2 = 0$), explicit solutions can be obtained for the other variables occurring in the equations. It is again simple to substitute into the calculated quantity ξ_1'. Making the transformation to the antiferromagnetic problem, that is using the variable v and then changing its sign, gives for the various lattices

S.Q.
$$\frac{\chi_0\epsilon}{I_\infty m} = \frac{\tanh^{-1} v(1-2v)(1+v)}{(1+2v)(1+v-4v^2)} \quad \text{for} \quad 0 \leqslant v \leqslant \tfrac{1}{8}(\sqrt{17}-1); \qquad (9)$$

Tri.
$$\frac{\chi_0\epsilon}{I_\infty m} = \frac{\tanh^{-1} v(1+v)}{(1+3v)(1+4v)} \quad \text{for} \quad 0 \leqslant v \leqslant \tfrac{1}{4}; \qquad (10)$$

S.C.
$$\left.\begin{aligned} \frac{\chi_0\epsilon}{I_\infty m} &= \tanh^{-1} v\, \frac{(3+p)(1+p)}{(3-p)(5-p)}, \\ v &= \frac{p^4 - 18p^3 + 18p - 1}{p^4 + 36p^3 + 54p^2 + 36p + 1}, \end{aligned}\right\} \quad \text{for} \quad 0 \leqslant v \leqslant 0{\cdot}2136 \quad \text{or} \quad \tfrac{1}{3} \leqslant p \leqslant 1; \qquad (11)$$

F.C.C.
$$\left.\begin{aligned} \frac{\chi_0\epsilon}{I_\infty m} &= \frac{\tanh^{-1} v(t-t^2+t^3)(1+t-t^2+t^3)}{(2-t+t^2-t^3)(3-t+t^2-t^3)}, \\ v &= \frac{t^3 - 3t^2 + t + 1}{t^3 + t^2 + t + 1}, \end{aligned}\right\} \quad \text{for} \quad 0 \leqslant v \leqslant 0{\cdot}09975 \quad \text{or} \quad 0{\cdot}8412 \leqslant t \leqslant 1. \qquad (12)$$

The regions of validity of the various parameters are determined as in the Bethe approximation, since the long-range order parameters are put explicitly equal to zero. The upper limits for v are found in the case of loose-packed lattices, from the specific heat singularity, and in the case of close-packed lattices, from the specific heat singularity for the corresponding ferromagnetic problem.

In order to compare these formulae with the exact series expansions it is necessary to expand the closed forms in a power series. For the two-dimensional lattices, this is very easy and it is found that for the simple quadratic lattice the expansion agrees up to v^7 with the expansions of Domb and Sykes (1957) and then the terms are too large by an amount $(16v^8 - 96v^9 + 488v^{10} - \ldots)$. This error can be attributed to the inaccurate counting of an octagon and similar larger clusters on the lattice. The expansion for the triangular lattice agrees up to the term v^5 and then is too large by an amount $(12v^6 - 204v^7 + 1944v^8 - 14\,388v^9 + \ldots)$, again the

error can be attributed to the inaccurate counting of hexagons and some larger clusters. The expansion for the three-dimensional lattices is more difficult, but as expected agreement is obtained up to v^5 for the simple cubic and up to v^3 for the face-centred cubic.

Fig. 2

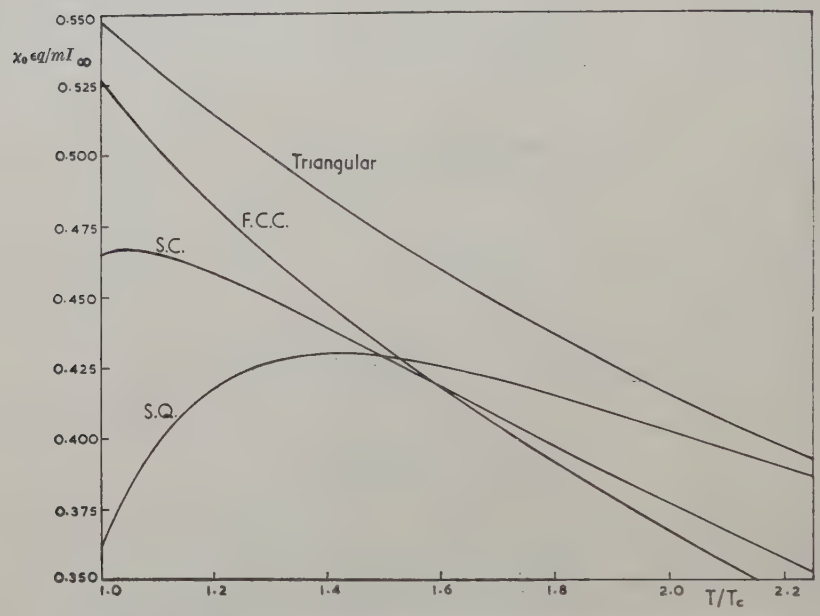

Graph of zero field susceptibility against reduced temperature for an antiferromagnet.

In fig. 2 the curves of $\chi_0 \epsilon q/mI_\infty$ are plotted against T/T_c and interesting results are observed. It is noticed that, while the curves for the close-packed lattices increase monotonically up to the Néel point, for the loose-packed lattices the curves show a maximum above the critical temperature and are decreasing when they reach this point. These maxima occur at $T/T_c = 1{\cdot}43$ for the simple quadratic and at $T/T_c = 1{\cdot}04$ for the simple cubic lattice. How the curves continue as the temperature is decreased through the Néel point is a very interesting question, but the solution of the basic equations in this region is complicated, and this was not attempted. For the close-packed lattices an additional difficulty arises from the fact that no ordered state exists even at absolute zero. Although it was found possible to write down the basic equations for the triangular lattice they are so complicated that no solution was attempted except for $T = 0$. At this point is was found that the entropy for this lattice is given by

$$S/R = \ln \tfrac{4}{3} = 0{\cdot}2877 \qquad . \; . \; . \; . \; . \; . \; (13)$$

compared with the exact value obtained by Wannier (1951) of

$$S/R = 0{\cdot}3383.$$

The agreement between the two results is not particularly good but the value (13) is almost identical to a result obtained by Wannier by considering the origin of the major part of the degeneracy. The agreement between (13) and this result is to be expected however since Wannier used just the configurations on the lattice treated correctly by the Kikuchi approximation, both methods neglecting intermediate-order parameters.

Despite the difficulty of solution in the low-temperature region, some idea of the behaviour can be obtained by writing the susceptibility in the form of Sykes and Fisher (1958). They showed that the susceptibility behaves essentially like the configurational energy, and this is only modified by a function which is small in the critical region. This was found to be the case for the Kikuchi approximation, the susceptibility being modified at the critical point by only 2% for the S.Q. lattice and $\frac{1}{2}$% for the triangular lattice. The shape of the curves can thus be deduced from the configurational energy or the specific heat. For the Bethe approximation the complete curves have been calculated numerically and a sharp cusp is observed at the Néel point. For the Kikuchi approximation, the loose-packed lattices will still show a discontinuity in the gradient but this will not be so pronounced, while the exact result will show a vertical point of inflexion, with no discontinuity in slope at the Néel point. For the close-packed lattice, since there is no specific heat discontinuity, and no completely ordered state, it may be assumed that the curves pass through the corresponding ferromagnetic Curie point with no change of slope or point of inflexion in the case of the exact solution.

The striking result of this investigation is the appearance of the maximum in the susceptibility for the loose-packed lattices. Cooke *et al.* (1959) have observed experimentally such maxima for various antiferromagnetic salts at $T/T_c \cong 1{\cdot}01$. This result is in quite good agreement with the value obtained for the simple cubic lattice, and it thus appears that the maximum is of an essentially cooperative nature. A difficulty of comparison arises, however, since the salts considered all have a face-centred cubic structure, which on the Ising model shows no antiferromagnetic transition. The stabilizing effects of second nearest neighbours with a ferromagnetic interaction and also a consideration of anisotropic effects may well provide for the antiferromagnetic transition and the associated maximum. It is hoped to study these effects in more detail.

Acknowledgments

I should like to thank Professor C. Domb for his continued interest and encouragement in this work and Drs. M. F. Sykes and M. E. Fisher for many discussions on the subject. I should also like to thank the Department of Scientific and Industrial Research for a maintenance grant for the period during which most of this work was completed.

APPENDIX I

Method of Extrapolation for the Body-centred Cubic Lattice and $z^2 = 0{\cdot}529$

i	ΔCi	h	A	A^*/i^{h^*}
1	0·073631		0·07363	0·0980
		0·982		
2	0·037271		0·08926	0·0409
		1·157		
3	0·023321		0·09309	0·0246
		1·181		
4	0·016603		0·09523	0·0171
		1·232		
5	0·012611		0·09582	0·0129
		1·220		
6	0·010098		0·09654	0·0103

The value of h^* chosen is 1·26 which gives $A^* = 0{\cdot}0980$.

$$C_\infty = 0{\cdot}1735 + 0{\cdot}0980 \sum_{i=7}^{\infty} 1/i^{1{\cdot}26} = 0{\cdot}405.$$

APPENDIX II

Results for the Extrapolation of the Spontaneous Magnetization

S.C.		B.C.C.		F.C.C.	
T/T_c	I_0/I_∞	T/T_c	I_0/I_∞	T/T_c	I_0/I_∞
0·998	0·06	0·999	0·04	0·998	0·02
0·993	0·18	0·990	0·19	0·994	0·08
0·987	0·23	0·964	0·39	0·987	0·15
0·982	0·29	0·936	0·55	0·973	0·30
0·972	0·43	0·909	0·64	0·959	0·40
0·920	0·64	0·859	0·76	0·949	0·46
0·858	0·80	0·789	0·84	0·916	0·61
0·740	0·91	0·688	0·92	0·800	0·82
0·642	0·95	0·600	0·96	0·684	0·92
0·558	0·98	0·523	0·98	0·512	0·98

References

Brooks, J. E., and Domb, C., 1951, *Proc. roy. Soc.* A, **207,** 343.
Cooke, A. R., Lazenby, R., McKim, F. R., Owen, J., and Wolf, W. P., 1951, *Proc. roy. Soc.* A, **250,** 97.
Domb, C., and Sykes, M. F., 1956, *Proc. roy. Soc.* A, **235,** 247 ; 1957, *Ibid.* A, **240,** 214.
Dyson, F. J., 1956, *Phys. Rev.*, **102,** 1217.
Firgau, E., 1942, *Ann. Phys., Lpz.*, **40,** 295.
Fisher, M. E., 1959, *Physica*, **25,** 521.
Kikuchi, R., 1951, *Phys. Rev.*, **81,** 988.
Münster, A., and Sagel, K., 1956, *Z. Phys. Chem., Neue Folge.*, 7, **267,** 296.
Potts, R. B., 1952, *Phys. Rev.*, **88,** 352.
Sykes, M. F., and Fisher, M. E., 1958, *Phys. Rev. Letters*, **1,** 321.
Wakefield, A. J., 1951, *Proc. Camb. phil. Soc.*, **47,** 419.
Wannier, G. H., 1950, *Phys. Rev.*, **79,** 357.
Yang, C. E., 1952, *Phys. Rev.*, **85,** 808.

The Spacing of Prismatic Dislocation Loops†

By R. Bullough and R. C. Newman

Research Laboratory, Associated Electrical Industries, Aldermaston Court, Aldermaston, Berkshire

[Received May 11, 1960]

Abstract

The stresses round a circular prismatic dislocation loop are determined and used to calculate the spacings between such loops in a row generated from a source of internal stress. The results are consistent with the available experimental observations.

§ 1. Introduction

Recent experiments by Dash (1958), Jones and Mitchell (1957) and Parasnis and Mitchell (1959) have established that stresses set up round internal defects in crystals can be relieved by the generation and motion of several co-axial prismatic dislocation loops (Seitz 1951). The diameters of the loops in such a row are approximately equal and comparable with the diameter of either an artificially introduced inclusion (Jones and Mitchell 1957) or a particle of precipitated second phase (Parasnis and Mitchell 1959); the stresses are a consequence of a differential expansion during heating in the former case and a change in volume on precipitation in the latter case.

The purpose of this paper is to investigate theoretically the relation between the separation and diameter of adjacent loops in a particular row of such loops. In § 2 the stresses and displacements associated with a single prismatic loop in an elastic medium are derived. These are obtained by 'cutting' along the cylindrical glide surface and applying suitable boundary conditions to the two curved surfaces. Finally in § 3 the equilibrium configuration of a row of loops is computed, subject to the assumption that a critical shear stress is required to move a loop and the results are compared with the available experimental observations.

§ 2. The Stresses and Displacements around the Loop

We shall consider a circular prismatic loop of strength b and radius a with its centre at the origin of a cylindrical coordinate system, $z=0$ being the plane of the loop. This dislocation is created by making a cylindrical cut over the surface $r=a$ in an infinite medium and applying

† Communicated by the Authors.

a shear stress to the two sides of the cut so that the relative displacement across $r=a$ is given by

$$w^{o}(a,z)-w^{i}(a,z)=\left.\begin{array}{ll}-b/2 & z>0\\ +b/2 & z<0\end{array}\right\}, \qquad \ldots\ldots (1)$$

where w is the displacement in the z direction and the superscripts o and i refer to regions outside ($r\geqslant a$) and inside ($r\leqslant a$) the cut respectively. The cut is now rewelded and to ensure no additional forces are required for this procedure we must have continuity of traction across $r=a$; thus

$$\left.\begin{aligned}p_{rr}^{i}(a,z)&=p_{rr}^{o}(a,z),\\ p_{rz}^{i}(a,z)&=p_{rz}^{o}(a,z).\end{aligned}\right\} \qquad \ldots\ldots (2)$$

Finally, the radial displacement u must be continuous across $r=a$:

$$u^{i}(a,z)=u^{o}(a,z). \qquad \ldots\ldots\ldots (3)$$

The required stresses were obtained using the method of Fourier transforms (see for example Tranter and Craggs 1945). The two relevant solutions of the transformed biharmonic equation are:

and

$$\left.\begin{aligned}X^{i}(r,\eta)&=A(\eta)I_0(\eta r)+B(\eta)\eta r I_1(\eta r)\\ X^{o}(r,\eta)&=C(\eta)K_0(\eta r)+D(\eta)\eta r K_1(\eta r)\end{aligned}\right\} \qquad \ldots\ldots (4)$$

where

$$\left[\frac{d^2}{dr^2}+\frac{1}{r}\frac{d}{dr}-\eta^2\right]^2 X(r,\eta)=0. \qquad \ldots\ldots (5)$$

The arbitrary functions A, B, C and D were obtained by satisfying the boundary conditions (1), (2) and (3) after transformation; the expressions relating the stresses and displacements to the stress function $\chi(r,z)$, where

$$X(r,\eta)=\int_{-\infty}^{\infty}\chi(r,z)\exp(i\eta z)\,dz,$$

are given in full by Sneddon (1951).

The required solution in the region $r\geqslant a$ is:

$$\left.\begin{aligned}
p_{rr}&=\frac{2\alpha}{r}\mu\int_0^{\infty}\{(1-2\nu)r\eta v_{01}(\eta)+2(1-\nu)v_{11}(\eta)-a\eta v_{10}(\eta)\}\cos\eta z\,d\eta,\\
p_{rz}&=2\alpha\mu\int_0^{\infty}\{av_{10}(\eta)-rv_{01}(\eta)\}\eta^2\sin\eta z\,d\eta,\\
p_{zz}&=2\alpha\mu\int_0^{\infty}\{\eta r v_{11}(\eta)-2v_{01}(\eta)-\eta a v_{00}(\eta)\}\eta\cos\eta z\,d\eta,\\
w&=\alpha\int_0^{\infty}\{\eta r v_{11}(\eta)-2(1-\nu)v_{01}(\eta)-\eta a v_{00}(\eta)\}\sin\eta z\,d\eta,\\
u&=\alpha\int_0^{\infty}\{2(1-\nu)v_{11}(\eta)+\eta r v_{01}(\eta)-\eta a v_{10}(\eta)\}\cos\eta z\,d\eta,
\end{aligned}\right\} \qquad (6)$$

where

$$v_{ij}=K_i(r\eta)I_j(a\eta), \quad \alpha=ba/2\pi(1-\nu)$$

and μ and ν are the shear modulus and Poisson's ratio respectively. The solution for the region $r\leqslant a$ may be obtained simply by replacing v_{ij} by u_{ij} where

$$u_{ij}=(-1)^{i+j}I_i(r\eta)K_j(a\eta).$$

We have also obtained the elastic solution by making a cut through the plane of the loop and applying suitable tractions to the two planar sides of such a cut. The solution obtained using this latter model appears in a different form from that given above; for example, the shear stress on the cylindrical surface $r=a$ is

$$p_{rz}(a,z)=\pi\alpha\mu z\int_0^\infty \eta^2 J_1^2(a\eta)\exp(-\eta|z|)\,d\eta. \quad . \; . \; . \quad (7)$$

The equivalence of (7) and $p_{rz}(a,z)$ given by (6) may be demonstrated by showing that each is equal to the same line integral:

$$\frac{\alpha z}{2i}\int_{c-i\infty}^{c+i\infty}\frac{2^s\Gamma(2+\frac{1}{2}s)\Gamma(-1-s)\Gamma(1-s)a^{-s-2}|z|^s}{[\Gamma(-\frac{1}{2}s)]^2\Gamma(1-\frac{1}{2}s)}\,ds$$

by simple use of the product formula for the Mellin transform (Titchmarsh 1948); similarly the more general stresses and displacements can be related to line integrals of this type.

In order to determine the equilibrium spacing of loops in a row we shall require the variation of $p_{rz}(a,z)$ with $\rho=z/2a$. The integrals involved in (6) or (7) can be evaluated in terms of tabulated elliptic integrals (Watson 1952) and the variation is shown in fig. 1.

§ 3. The Equilibrium Configuration of a Row of Loops

It is assumed that when a new loop is created at the surface of the inclusion it will glide on the cylindrical surface and simultaneously cause the other loops in the row to move further away from the inclusion. The final configuration will be achieved when the shear stress on each one of the loops due to its neighbours is equal to the critical shear stress p_{rz}^{crit} to move the loop. The shear stress distribution around a single loop, as shown in fig. 1, decreases rapidly with distance z from the loop:

$$p_{rz}(a,z)\to\frac{ba^3\mu}{(1-\nu)z^4} \quad \text{(large } z\text{)}.$$

In view of this, and since experimental observations indicate that the separation between loops is comparable with their diameters, the resultant shear stress on any loop of the row is quite well determined by the relative positions of its first and second neighbours only. In setting up the relevant difference equations for each loop it was convenient to introduce

Fig. 1

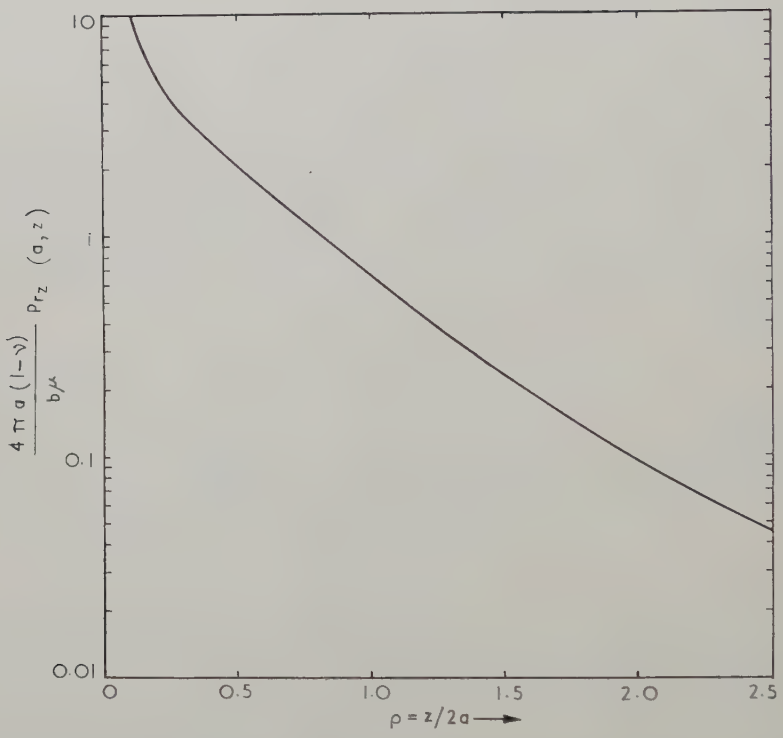

The shear stress distribution on the cylindrical glide surface $r=a$ due to a single loop of radius a and strength b situated at $z=0$.

Fig. 2

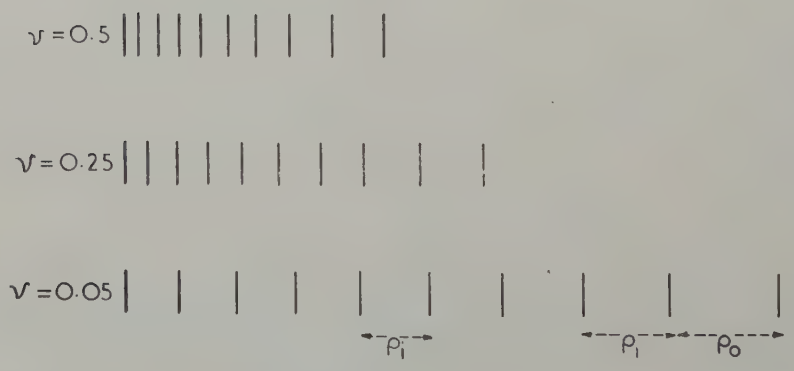

Equilibrium configurations for row of ten loops drawn to scale ($\rho = z/2a$).

the dimensionless parameter v given by

$$v = \frac{4a\pi(1-\nu)}{b\mu} p_{rz}^{\text{crit}}. \quad \ldots \quad (8)$$

These equations were linearized and solved by a method of repeated approximation on a digital computer. Computations were made for both a row of five and ten loops with three values of v: 0·5, 0·25 and 0·05. Tabulated results for the row of ten loops are given in table 1 and shown diagrammatically in fig. 2.

Table 1. Computed spacings for the row of ten loops in units of the loop diameter

v \ ρ_i	0	1	2	3	4	5	6	7	8
0·5	1·23	0·951	0·791	0·684	0·606	0·546	0·491	0·478	0·317
0·25	1·55	1·25	1·07	0·952	0·862	0·792	0·731	0·703	0·549
0·05	2·47	2·05	1·83	1·68	1·57	1·48	1·41	1·35	1·25

Table 2. Values of p_{rz}^{crit}/μ as a function of the parameter v and the ratio $2a/b$

v \ $2a/b$	10^5	10^4	10^3
0·5	10^{-6}	10^{-5}	10^{-4}
0·25	5×10^{-7}	5×10^{-6}	5×10^{-5}
0·05	10^{-7}	10^{-6}	10^{-5}

The configuration for the row of five loops was not significantly different from the outermost five loops in the row of ten for all the v values. Hence the ten loop configurations may also be used to determine the configurations for any number of loops less than ten. It may be seen from fig. 2 or table 1 that as the critical shear stress is reduced (decreasing values of v) the variation of spacing between any two adjacent loops in the row also decreases. For a row of more than about five loops and with $v = 0{\cdot}5$ it is seen from fig. 2 that the loops become closely spaced and hence in this case our neglect of third neighbour interaction is not justified near the source of the loops.

It has been assumed above that the critical shear stress to move a loop is independent of the loop diameter. This we believe is a reasonable assumption when the diameter of the loop exceeds about 10**b** (where **b** is the Burgers vector of the loop). Although it has not been possible to solve the integral equation appropriate to a Peierls loop, and hence obtain a direct indication of the dependence of the dislocation width on the loop diameter, the corresponding problem for a pair of parallel straight

dislocations lying back to back has been solved and indicates that the width variation is not significant until the spacing between the lines is less than 5**b**.

In order to compare the present results with experimental observation the following procedure is adopted. From the number of loops in the row and the mean ratio of spacing to loop diameter it is possible, with the aid of fig. 2, to determine the value of the parameter v. This value of v and the measured loop diameter $2a$ enable an estimate of the critical shear stress to be made from (8). The dependence of the critical shear stress on v and the ratio $2a/b$ as given by (8) is shown in table 2 for a wide range of loop diameters.

Table 3. Application to the experimental observations of Dash (1958) and Parasnis and Mitchell (1959)

Material	Number of loops in row	Approximate loop diameter (microns)	ρ_i(mean)	Estimated value of v	Value of critical shear stress
AgCl	>10	1·3	0·9	$\lesssim 0{\cdot}25$	$\lesssim 10^{-5}\,\mu$
Si	4	30	0·7	$\gtrsim 0{\cdot}5$	$\gtrsim 10^{-6}\,\mu$

We have applied this method to the results of Parasnis and Mitchell (1959, fig. 6) on silver chloride and Dash (1958, fig. 1) on silicon. Their results are summarized in table 3 and it is seen that these lead to not unreasonable values of the critical shear stress. A more stringent test of this theory must await further experimental observations.

Acknowledgments

The authors wish to thank Mr. P. Redman for his assistance with the numerical work and Mr. D. P. R. Petrie and Mr. R. L. Rouse for their encouragement. Thanks are also due to Dr. T. E. Allibone, F.R.S., Director of the Laboratory, for permission to publish this paper.

References

Dash, W. C., 1958, *Phys. Rev. Letters*, **1**, 11.
Jones, D. A., and Mitchell, J. W., 1957, *Phil. Mag.*, **3**, 1.
Parasnis, A. S., and Mitchell, J. W., 1959, *Phil. Mag.*, **4**, 171.
Seitz, F., 1951, *Rev. mod. Phys.*, **23**, 328.
Sneddon, I. N., 1951, *Fourier Transforms* (New York: McGraw-Hill).
Titchmarsh, E. C., 1948, *Introduction to the theory of Fourier Integrals* (Oxford : Clarendon Press).
Tranter, C. J., and Craggs, J. W., 1945, *Phil. Mag.*, **36**, 241.
Watson, G. N., 1952, *The theory of Bessel functions* (Cambridge : University Press).

Some Elastic and Thermal Properties of Zirconium and Tungsten†

By A. Myers

Physics Department, the University, Leeds‡

[Received March 28, 1960; and in revised form August 9, 1960]

Abstract

The longitudinal and shear wave velocities of 10 Mc/s ultrasonic waves have been measured in polycrystalline specimens of zirconium and tungsten at temperatures between 14° and 300°K and the elastic constants calculated from these measurements. The difference between the specific heats at constant pressure and at constant volume in these metals at various temperatures has been calculated by means of the thermodynamic relation involving the bulk modulus of the metal; this difference is used in the examination of a suggested method of obtaining the γ values, and hence the electronic specific heats of metals.

It is found that the γ values for zirconium and tungsten estimated by this method are greater by factors of about 1·3 and 2·8 respectively than the values obtained from low-temperature calorimetric determinations. For a number of reasons, which are discussed, close agreement is not to be expected but no satisfactory explanation for the very wide discrepancy has been found.

§ 1. Introduction

The γ value of a metal is the value of the proportionality constant relating the electronic contribution to the specific heat (C_e) to the absolute temperature (T) in the relation $C_e = \gamma T$, which is generally assumed to be valid for temperatures such that $kT \ll \epsilon_0$, where k is Boltzmann's constant and ϵ_0 is the Fermi energy.

The usual method of obtaining γ has been by means of low-temperature calorimetry (γ obtained in this way will be denoted by γ_0). Such methods of obtaining γ, although applicable to most metals, are tedious in practice and almost invariably involve measurements at liquid helium temperatures. Recently, γ values have been estimated by Clusius and Bühler (1955), Clusius and Franzosini (1956), Clusius and Losa (1955 a, b), Clusius *et al.* (1957), and Clusius and Schachinger (1947, 1952 a, b) using a method which does not involve measurements in the liquid helium temperature range. They assume that the lattice specific heat (C_L) can be represented, over an appreciable temperature range, by a single Debye term. They select a series of trial γ values and calculate the electronic specific heat which would correspond to these values; the electronic specific heat is subtracted from the total specific heat at constant volume (C_v), i.e. from the sum of the lattice and electronic contributions. The γ value,

† Communicated by the Author.

‡ For academic year 1959–60, at Physics Department, Brown University, Providence, R.I., U.S.A.

which leaves the remainder most nearly following a single term Debye curve over a sufficiently large temperature interval, is then chosen as the one to be associated with the electronic specific heat of the metal. The actual technique is to plot graphs of θ_D (the Debye characteristic temperature) against the absolute temperature for various γ values, and to select that value of γ for which the variation of θ_D with temperature is least.

The method depends upon a knowledge of the variation of C_v with temperature. Measurements of the specific heats of metals, however, are obtained under constant pressure conditions (C_p) and these must be converted into values corresponding to constant volume conditions. This conversion can be made by means of the relation:

$$(C_p - C_v)_T = 9\alpha^2 K V T,$$

where α is the coefficient of linear expansion, K is the bulk modulus and V is the atomic volume. In order to allow the conversion of specific heat data to be made over the whole temperature range of interest, the variation of α and K with temperature is needed. Extensive data exist for the temperature dependence of the expansion coefficient of most metals but the temperature dependence of the bulk modulus is known only in a few cases. Approximate relations between C_p and C_v exist which do not involve the temperature variation of K and for most metals these relations are sufficiently accurate for the present purpose. It has been found as a result of the present investigations that this situation holds for zirconium and tungsten. It was considered necessary to show this because γ values which do not agree with γ_0 are obtained for both metals following the method used by Clusius *et al.*, and also the uncertainty introduced by using the approximate relations is not known. In addition, it has been stated (Dayal 1944) that tungsten does not obey Grüneisen's law (namely that $KV\alpha/C_v$ is a constant, independent of temperature) at temperatures below 300°K; this is involved in deriving the approximate relation. Expansion coefficient data are available for tungsten and zirconium in the appropriate temperature range but there is no corresponding information for the bulk moduli; the variations of the bulk moduli with temperature have therefore been measured. The bulk moduli are determined by measuring the ultrasonic longitudinal and shear wave velocities, the accuracy depending on the ultrasonic attenuation coefficients of the metals. The lower these, the more accurate are the velocity measurements. Tungsten and zirconium possess low attenuation coefficients and were partly chosen for this reason. These metals are also among the most readily available of the relatively few which have the following additional advantages:

(*a*) they have fairly large γ values (so that C_e will be significant in comparison to C_L);

(*b*) data is available giving the temperature dependence of α and C_p;

(*c*) the anharmonic motion of the lattice vibrations is probably small (see § 4).

§ 2. Experimental Details

2.1. *Elastic Moduli*

The elastic moduli of metals can be obtained conveniently, having regard to the temperature range involved, by measurement of the velocities of ultrasonic longitudinal and shear waves. For an isotropic medium, and these polycrystalline materials are assumed to be effectively isotropic, the following relations hold and enable K to be determined:

$$V_L = \left\{\frac{1}{p}\left[K + \tfrac{4}{3}G\right]\right\}^{1/2}, \quad V_S = \left\{\frac{G}{p}\right\}^{1/2},$$

where V_L and V_S are the velocities of propagation of elastic longitudinal and shear waves respectively, G is the rigidity modulus and p is the density.

The wave velocities have been measured using a method described in a previous paper (Myers *et al.* 1959) under the name of the coincidence technique. In this a continuous sequence of pulses of oscillation (of 3–5 μsec duration) are applied across a quartz transducer cemented to one end of the specimen. Signals are received at the other end of the specimen by means of a similar quartz crystal. Because of the reflection of pulses at the ends of the specimen, several pulses are received for each pulse initially propagated. The coincidence is made between the front of any of the reflected pulses, or the directly transmitted pulse, and the front of the subsequent pulse of oscillation from the oscillator. The time taken for the wave to travel through the specimen is obtained by measurement of the pulse repetition frequency of the oscillator.

10 Mc/s longitudinal and shear waves are propagated by using X-cut and Y-cut quartz crystals respectively.

The wave is delayed on every traversal of the specimen by a small time; this is an end effect caused by the wave traversing the metal to crystal bond and also by interference effects due to reflections at the various boundaries at the ends of the specimen. The usual method of eliminating these time delays is to measure the velocity in two or more different lengths of the specimen and consider the time taken to travel a path equal to the difference in length of the specimens (Neighbours *et al.* 1952). This procedure has been followed here. In addition, the magnitudes of the end effects have been made as small as possible by using very thin bonds. Apparent delays of 0·01 to 0·03 μsec for longitudinal waves and of 0·02 to 0·06 μsec for shear waves were measured and corrected for; even if the correction were not made, the error introduced from this source would have been less than 0·3% in the transit time.

2.2. *The Specimens*

Both the zirconium and the tungsten were supplied in the form of sintered cylindrical bars of about 20 mm diameter by Murex, Ltd. Measurements were taken in both cases on two specimens about 6 and 12 cm long. The suppliers quote the purity of the zirconium as from 98 to 99%, about 1% to 2% of the impurity being hafnium and less than

0·3% being other elements. This was as pure zirconium as could readily be obtained commercially. The tungsten, on the other hand, was stated to contain only from 0·02 to 0·05% of iron and traces only of other elements, giving it a purity of about 99·95%.

The density of the zirconium specimens was $6{\cdot}55 \pm 0{\cdot}01$ g/cm^3; this is to be compared with an x-ray density for zirconium of $6{\cdot}502 \pm 0{\cdot}002$ g/cm^3. The 1 to 2% hafnium impurity was thought to be responsible for the actual density being higher than the x-ray value and measurements by de Boer and Fast (1940) on zirconium containing 0·5% hafnium confirm this to some extent by giving an x-ray density of 6·54 g/cm^3. It is probable, however, that the actual density was determined not only by the impurity but also by the porosity of the sintered metal. The purity of the tungsten was much higher than that of the zirconium and the density of $18{\cdot}65 \pm 0{\cdot}04$ g/cm^3 was noticeably low in comparison with the x-ray density of $19{\cdot}270 \pm 0{\cdot}002$ g/cm^3; this was due to porosity. It is not obvious which density should be taken in order to estimate the elastic constants of pure, non-porous specimens of polycrystalline zirconium and tungsten. Fewer objections seem to be against taking the x-ray densities and, following Overton and Gaffney (1955), these have been used. In subsequent discussions, however, the implications of this decision are considered.

2.3. *The Bonds and the Cryostat Arrangements*

Dow Corning 200 silicone fluid, of viscosity $2{\cdot}5 \times 10^6$ centistokes, was used to produce the bonds for use with longitudinal waves, and Edwards apiezon grease grade N was used for the shear waves; in both cases the bonds were effective from 300° to 14°K.

The temperature of the specimens was controlled by suspending them inside a silvered glass dewar in which the pressure between the walls can be varied. This dewar was immersed in a bath of liquid nitrogen. At the start of the experiments, the pressure in the dewar interspace was about 0·1 cm of mercury, so that the heat conduction across the walls was appreciable and the specimen cooled down. When the required temperature was reached, the interspace pressure was reduced to about 10^{-6} cm of mercury, producing an effective thermal isolation while measurements were taken.

Temperatures lower than the boiling point of liquid nitrogen were obtained by immersing the specimen in either liquid nitrogen or liquid hydrogen and reducing the pressure above the liquid.

The temperature of the specimen was measured by means of two calibrated chromel–alumel thermocouples strapped one at each end of the specimen.

§ 3. Results

The wave velocities obtained for zirconium are shown in figs. 1 and 2. In these figures the full line gives the variation of the velocity with temperature after the end effects have been allowed for; these values are given at 25°K intervals in table 1. Also given in table 1 are the adiabatic elastic

constants E, K and G (where E is Young's modulus) and the factor $(C_p - C_v)_T$. The values of $(C_p - C_v)_T$ have been obtained using the expansion coefficient data of Erfling (1939) and Nix and MacNair (1942) for zirconium and tungsten respectively. The values of $(C_p - C_v)_{\mathrm{NL}}$ are those given by the Nernst–Lindemann equation: $(C_p - C_v)_{\mathrm{NL}} = AC_p^2T$, where A is a constant which is evaluated at 300°K; this is an approximate relation

Fig. 1

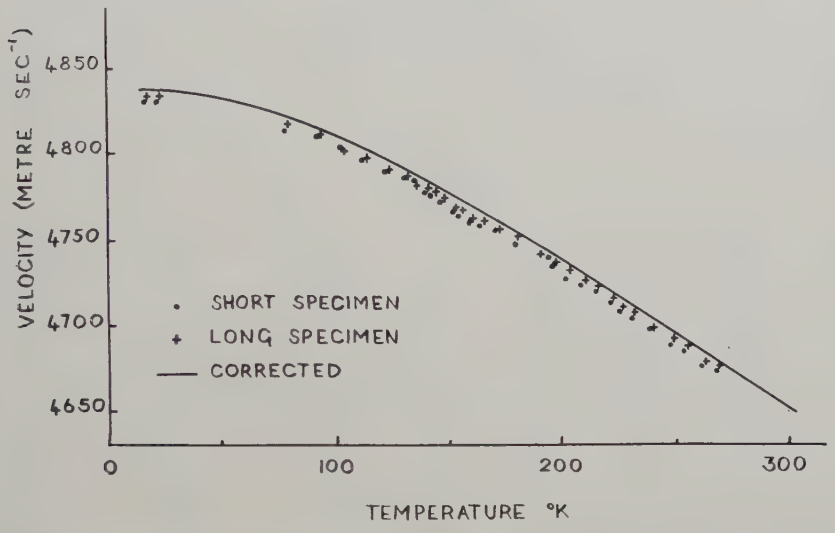

The variation of the longitudinal wave velocity in zirconium with temperature.

Fig. 2

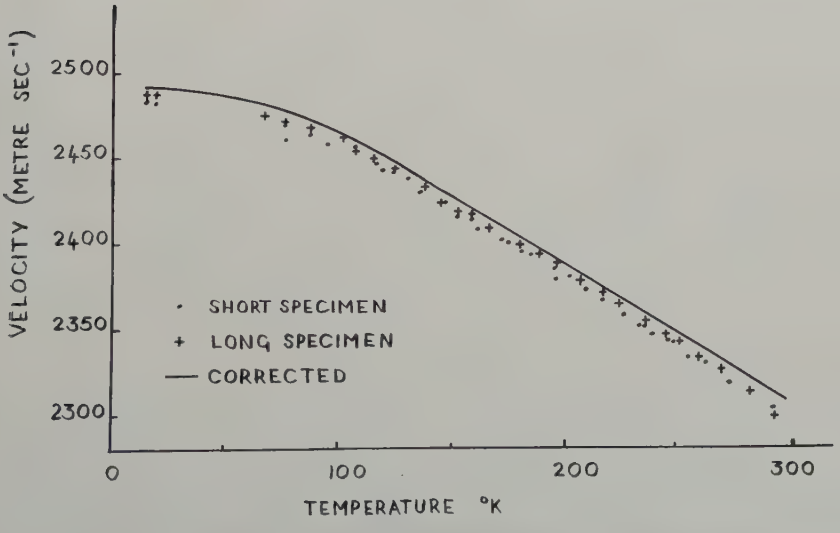

The variation of the shear wave velocity in zirconium with temperature.

much used in the conversion of specific heat data from constant pressure to constant volume conditions.

Table 1. The smoothed ultrasonic wave velocities, the elastic constants and the factor $(C_p - C_v)$, calculated by means of the thermodynamic and also by the Nernst–Lindemann relation, for zirconium and tungsten. Velocities are given in metres per second, elastic constants in units of 10^{-11} dynes per square centimetre and $(C_p - C_v)$ in calories per gram mole per °K

T	V_L	V_S	E	G	K	$(C_p-C_v)_T$	$(C_p-C_v)_{NL}$
(i) Zirconium							
	±4	±3	$\pm 0{\cdot}1_5$	±0·01	±0·06	± ~1%	± ~2%
0	4838	2484	$10{\cdot}6_2$	4·02	9·88	0·0000	0·0000
25	4836	2484	$10{\cdot}6_3$	4·02	9·86	0·0000	0·0000
50	4830	2480	$10{\cdot}5_9$	4·01	9·84	$0{\cdot}0001_8$	$0{\cdot}0006_7$
75	4822	2472	$10{\cdot}5_1$	3·98	9·81	0·0014	0·0027
100	4808	2461	$10{\cdot}4_4$	3·95	9·77	0·0044	0·0055
125	4794	2442	$10{\cdot}3_0$	3·89	9·74	0·0081	0·0086
150	4776	2423	$10{\cdot}1_4$	3·82	9·73	0·0113	0·0116
175	4758	2403	$9{\cdot}9_9$	3·76	9·69	0·0144	0·0148
200	4737	2388	$9{\cdot}8_6$	3·71	9·63	0·0178	0·0179
225	4716	2365	$9{\cdot}6_9$	3·64	9·61	0·0213	0·0211
250	4695	2345	$9{\cdot}5_5$	3·58	9·55	0·0246	0·0242
275	4672	2323	$9{\cdot}3_7$	3·51	9·50	0·0282	0·0276
300	4650	2298	$9{\cdot}1_8$	3·43	9·49	0·0300	0·0300
(ii) Tungsten							
	±5	±4	±0·7	±0·04	±0·2	± ~1·5%	± ~2·5%
0	5116	2836	$39{\cdot}7_5$	15·55	29·86	0·0000	0·0000
25	5115	2835	39·7	15·54	29·86	0·0000	0·0000
50	5114	2833	39·7	15·52	29·86	$0{\cdot}0003_9$	$0{\cdot}0004_1$
75	5112	2831	39·6	15·50	29·85	0·0019	0·0024
100	5110	2828	39·5	15·46	29·85	0·0047	0·0058
125	5107	2824	39·4	15·41	29·84	0·0083	0·0100
150	5103	2820	39·3	15·36	29·82	0·0120	0·0144
175	5099	2816	39·2	15·31	29·80	0·0162	0·0190
200	5094	2812	39·1	15·26	29·73	0·0204	0·0233
225	5089	2807	38·9	15·20	29·69	0·0246	0·0272
250	5085	2801	38·8	15·13	29·66	0·0295	0·0321
275	5079	2796	38·7	15·07	29·64	0·0354	0·0362
300	5075	2791	38·5	15·01	29·63	0·0410	0·0410

§ 4. Discussion

The comparison of values of $(C_p - C_v)$ given by the Nernst–Lindemann equation with those given by the thermodynamic relation shows that the two sets of values agree well for both zirconium and tungsten at all except the lower temperatures; here it has been found that the disagreement arises not because of the variation of K with temperature, which is

neglected in the Nernst–Lindemann equation but because of the assumption that C_p is proportional to α (using Grüneisen's law); thus the disagreement is due to the well-known failure of this law at low temperatures. Whereas with zirconium the assumption that C_p is proportional to α leads to an error of about 30% in the value of $(C_p - C_v)$ at 100°K, the error introduced is only 5% if the bulk modulus is assumed not to vary with temperature. In fact a very close estimate of $(C_p - C_v)$ can be obtained by using the relation $(C_p - C_v) = B\alpha^2 T$, where B is a temperature independent constant to be evaluated at room temperature, rather than the Nernst–Lindemann relation. This situation does not necessarily hold in all metals especially those in which the bulk modulus is very temperature dependent. The magnitude of the conversion factor $(C_p - C_v)$ is small in the two metals

Fig. 3

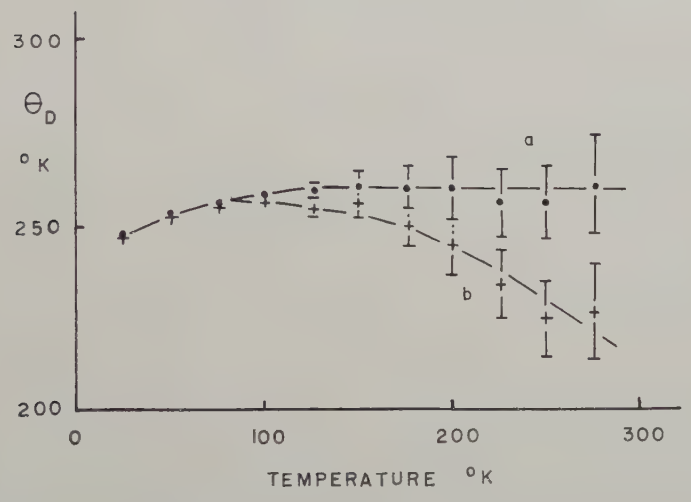

The variation of θ_D with temperature for zirconium. A γ value of $9{\cdot}1 \times 10^{-4}$ cal mole^{-1} deg^{-2} is assumed in curve (*a*) and a γ value of $7{\cdot}0 \times 10^{-4}$ cal mole^{-1} deg^{-2} is assumed in curve (*b*).

studied even at normal temperatures; at 100°K although the Nernst–Lindemann relation gives a value for $(C_p - C_v)$ differing appreciably in zirconium from that given by the thermodynamic relation, the whole term represents only a small fraction, about 0·1% of C_v.

The values of $(C_p - C_v)_T$ for zirconium shown in table 1 have been used to convert the specific heat data of Skinner and Johnston (1951) to constant volume conditions; this has then been used to estimate the γ value of the metal employing the method used by Clusius. The plot of θ_D against temperature is shown in fig. 3 and a γ value of $9{\cdot}5 \times 10^{-4}$ cal mole^{-1} deg^{-2} is indicated. This is to be compared with the values of $6{\cdot}9 \times 10^{-4}$ cal mole^{-1} deg^{-2} (Estermann *et al.* 1952) and $7{\cdot}25 \times 10^{-4}$ cal mole^{-1} deg^{-2}

(Wolcott 1955). The zirconium used by Skinner and Johnston was of high purity and their measurements accurate.

When the method is applied to tungsten, using the specific heat data compiled by Kelley (1948), the γ value obtained is 9×10^{-4} cal mole^{-1} deg^{-2} in comparison with values of $3{\cdot}53 \times 10^{-4}$ cal mole^{-1} deg^{-2} (Rayne 1954) and $2{\cdot}9 \times 10^{-4}$ cal mole^{-1} deg^{-2} (Wolcott 1955). The plots of θ_D against temperature are shown in fig. 4 in which it can be seen that the discrepancy between the above values cannot be explained in terms of the estimated experimental uncertainty.

The specific heat data for tungsten are less accurate than those for zirconium and, in order to check the above result, the specific heat of tungsten was measured between 77° and 300°K and agreement obtained to within about 1%. It was found that the value of γ indicated was again about 9×10^{-4} cal mole^{-1} deg^{-2}.

Fig. 4

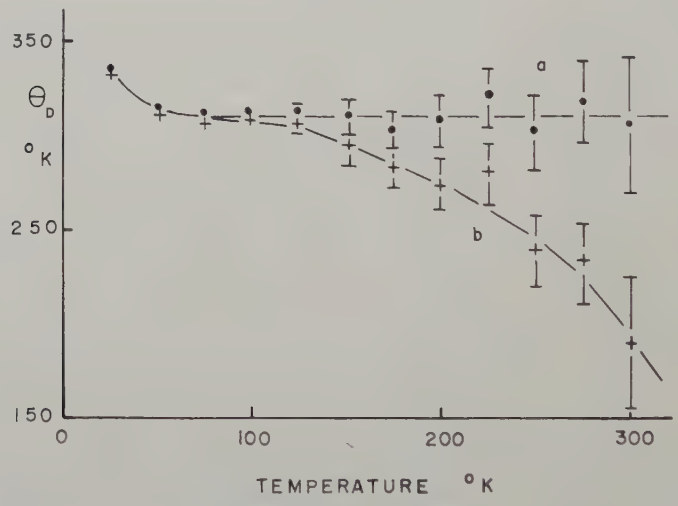

The variation of θ_D with temperature for tungsten. A γ value of $9{\cdot}0 \times 10^{-4}$ cal mole^{-1} deg^{-2} is assumed in curve (*a*) and a γ value of $3{\cdot}0 \times 10^{-4}$ cal mole^{-1} deg^{-2} is assumed in curve (*b*).

The principles involved in the calculation of γ values by the method used by Clusius have been known for some time (cf. Stoner 1938). A γ value for tungsten has been previously estimated (Wilson 1954) by considering data at 1000°K; this value is $5{\cdot}2 \times 10^{-4}$ cal mole^{-1} deg^{-2} and is in fairly good agreement with γ_0. In view of this the calculations were extended to 2000°K, using the specific heat data compiled by Kelley and the Nernst–Lindemann relation for $(C_p - C_v)$ above 300°K.

It is well established that at temperatures above about $\theta_D/3$, Grüneisen's law agrees very well with experiment, so $(C_p - C_v)_{NL}$ should give reliable values in the region above 300°K; in addition, $(C_p - C_v)$ is about three

times smaller than C_e and any small deviations from Grüneisen's law will be unimportant.

At high temperatures the lattice specific heat becomes less and less dependent on the precise θ_D value chosen and ultimately approaches 3R, thus a plot of θ_D against temperature is not suitable. Instead $(C_v - C_L)/T$ has been calculated and is shown in table 2, a θ_D value of 310°K being used as this is the value generally accepted and is also the value indicated by the curves of fig. 4. $(C_v - C_L)/T$ gives the γ value of the metal provided that the lattice specific heat follows Debye's theory. It can be seen that except between about 100° and 400°K fairly good agreement with γ_0 is obtained. Thus, between 100° and 400° there is an additional contribution to the specific heat; at higher temperatures the contribution appears to decrease.

Table 2. Estimated γ values for tungsten assuming $\theta_D = 310$°K. $(C_v - C_L)$ is given in units of calories per gram mole per °K

T°K	100	200	300	400	500	600
$(C_v - C_L)/T \times 10^4 \pm \sim 10\%$	5·0	9·3	9·3	5·0	4·2	4·0
T°K	700	800	1000	1200	1500	2000
$(C_v - C_L)/T \times 10^4 \pm \sim 10\%$	3·8	4·0	4·1	4·5	4·5	4·6

One possible reason why the γ values obtained for zirconium and tungsten do not agree with their respective γ_0 values is that, in the calculation of the elastic constants from the wave velocities, incorrect densities may have been taken. If a different density were taken, $(C_v - C_L)$ would be changed by an amount proportional to the temperature and hence γ would be changed; a decrease in density would lead to an increase in the estimated value of γ and to an even worse agreement with γ_0. It is inconceivable that a higher density than the x-ray value should be used but even if it were, although a lower estimate for γ would result, the variation of $(C_v - C_L)/T$ shown in table 2 for tungsten would not be explained. Also, if the actual instead of the x-ray density were taken, since $(C_v - C_L)$ is at least three times greater than $(C_p - C_v)$, the resulting γ value would be greater by only about 3%, i.e. by less than the uncertainty in γ. Thus, the porosity of the specimens does not appreciably affect the γ value obtained, nor could it account for the temperature dependence of $(C_v - C_L)/T$ observed in table 2.

The increase of the specific heat beyond that expected, in the temperature region above about 100°K, may be due either to the Debye theory not being obeyed by tungsten or to an increase in the γ value of the metal as

the temperature is increased. Increases in γ can occur when open electronic bands overlap (Elcock *et al.* 1953). It is not, however, expected that this will happen at temperatures so low in comparison to ϵ_0/k (the degeneracy temperature). Interactions between the electron gas and the lattice vibrations can also lead to an increase in γ (Buckingham and Schafroth 1954, Jones 1957). Buckingham and Schafroth find that because of modification of the density of energy levels at the Fermi surface γ is increased at lower temperatures but the increase when $T \gg \theta_D$ is zero. At intermediate temperatures the contribution to the γ value has not been evaluated. The interaction considered by Jones is one which gives a significant contribution to the electronic specific heat when the electronic energy as a function of momentum is very different from that in the free electron case. This is the situation when the Fermi surface approaches closely the Brillouin zone boundary. This interaction also leads to an increase in γ_0. It is unlikely, however, that these effects are responsible for the unusual behaviour of the apparent γ value in tungsten since the low temperature γ value obtained experimentally agrees very well with that calculated theoretically (Manning and Chodorow 1939); no account was taken, in the calculation, of the electron-lattice interactions and thus these interactions do not appear to play a significant part in determining the low temperature γ value for tungsten. Yet in both cases it is at low temperatures that the effects of such interactions are expected to be noticeable. Thus, it is presumed that the disagreement is due to a contribution to the lattice specific heat which is not given by the Debye theory. The deviations from Debye's theory may be caused either because the actual vibration spectrum of the normal modes for tungsten may not yield a specific heat which follows Debye's theory at these temperatures or because substantial contributions from anharmonicity of the lattice motion may be present. Any vibration spectrum able to yield a variation in the specific heat capable of explaining the situation would have a very different shape from that calculated theoretically for tungsten (Fine 1939). This spectrum, though based on the assumption of central forces acting between the atoms, predicts the same θ_D value as that obtained experimentally and predicts generally the same variation of θ_D at low temperatures as that experimentally observed. It also gives specific heat values which above about 50°K obey Debye's theory. It might, therefore, seem more likely that the cause of the disagreement is anharmonic motion of the lattice, which gives rise either to a positive or a negative contribution to the specific heat. Unfortunately theories of anharmonic motion are still in a rudimentary stage and it is not known if such a contribution to the specific heat could occur in tungsten. The melting point of tungsten, however, is high and the lattice vibrations at 300°K will be small in comparison to the interatomic spacing; thus, the anharmonicity is expected to be also small. This is borne out by the small values of other properties of the metal which are dependent on the anharmonicity of the lattice vibrations, e.g. the expansion coefficient and the variation of the bulk modulus with temperature. Clusius has found, however, that

this method of obtaining γ works in metals for which the anharmonicity is presumably greater than in tungsten as e.g. in rhodium.

The decrease of $(C_v - C_L)/T$ in tungsten above 400°K to a value close to γ_0 is remarkable since, at these temperatures, there is the possibility of vacancy formation giving an additional contribution to the specific heat and existing contributions may be more important, e.g. anharmonicity and band overlap. Vacancy formation becomes important in the region of the melting point and gives a positive contribution to the specific heat. This would lead to increasing values of $(C_v - C_L)/T$ with increasing temperatures; table 2 does not disclose any significant contribution of this type. Reasons have been presented suggesting that the anharmonic motion in tungsten is small; in table 2 any contribution from this source, even at 2000°K, appears to be negligible. The work of Elcock, Rhodes and Teviotdale raises the question of whether or not, because of the band overlap, the γ value should be constant up to 2000°K. The density of states curve calculated by Manning and Chodorow suggests that γ should decrease below γ_0 at high temperatures but, because of the idealised bands considered by Elcock *et al.*, no numerical check can be made to determine if 2000°K is sufficiently high for such a decrease to be important. $(C_v - C_L)/T$ in table 2 does not indicate any such decrease. Though it would appear that the value of $(C_v - C_L)$ in tungsten at high temperatures corresponds to C_e, there is the unlikely possibility that this agreement is fortuitous and that cancellation of two or more of the above effects is responsible for the constancy of $(C_v - C_L)/T$.

§ 5. Conclusions

The elastic constants of zirconium and tungsten have been measured between 14° and 300°K.

It has been noted that the Nernst–Lindemann relation enables specific heat values to be converted from constant pressure to constant volume conditions with sufficient precision for most purposes in zirconium and tungsten in the temperature range extending up to 300°K.

It has been found that the method used by Clusius for obtaining the γ values of metals does not give γ values agreeing with those obtained from measurement in the liquid helium temperature range in the case of zirconium and tungsten. In zirconium this difference although small is significant. In tungsten it is much greater than in zirconium but is reduced when Clusius' method is extended to temperatures greater than θ_D. On theoretical grounds it is thought that the additional contributions to the specific heats are not of electronic origin.

Acknowledgments

I am grateful for the advice and interest of Dr. L. Mackinnon and Dr. F. E. Hoare and also for the encouragement and helpful comments of Professor E. C. Stoner, F.R.S. In addition I am indebted to the Department of Scientific and Industrial Research for a maintenance grant.

References

de Boer, J. H., and Fast, J. D., 1940, *Rec. Trav. chim. Pays-Bas*, **59,** 161.

Buckingham, M. J., and Schafroth, M. R., 1954, *Proc. phys. Soc. Lond.* A, **67,** 828.

Clusius, K., and Bühler, H. H., 1955, *Z. Naturf.* A, **10,** 930.

Clusius, K., and Franzosini, P., 1956, *Z. Naturf.* A, **11,** 957.

Clusius, K., and Losa, C. G., 1955 a, *Z. Naturf.* A, **10,** 545 ; 1955 b, *Ibid.*, **10,** 939.

Clusius, K., Losa, C. G., and Franzosini, P., 1957, *Z. Naturf.* A, **12,** 34.

Clusius, K., and Schachinger, L., 1947, *Z. Naturf.* A, **2,** 90; 1952 a, *Ibid.*, **7,** 185 ; 1952 b, *Z. angew. Phys.*, **4,** 442.

Dayal, B., 1944, *Proc. Indian Acad. Sci.* A, **20,** 192.

Elcock, E. W., Rhodes, P., and Teviotdale, A., 1953, *Proc. roy. Soc.* A, **221,** 53.

Erfling, H. D., 1939, *Ann. Phys., Lpz.*, **34,** 136.

Estermann, I., Friedberg, S. A., and Goldman, J. B., 1952, *Phys. Rev.*, **87,** 582.

Fine, P. C., 1939, *Phys. Rev.*, **56,** 355.

Jones, H., 1957, *Proc. roy. Soc.* A, **240,** 321.

Kelley, K. K., 1948, *U.S. Bur. Mines Bull.*, Nos. 476, 477.

Manning, M. F., and Chodorow, M. I., 1939, *Phys. Rev.*, **56,** 787.

Myers, A., Mackinnon, L., and Hoare, F. E., 1959, *J. acoust. Soc. Amer.*, **31,** 161.

Neighbours, J. R., Bratten, F. W., and Smith, C. S., 1952, *J. appl. Phys.*, **23,** 889.

Nix, F. C., and MacNair, D., 1942, *Phys. Rev.*, **61,** 74.

Overton, W. C., and Gaffney, J., 1955, *Phys. Rev.*, **98,** 969.

Rayne, J., 1954, *Phys. Rev.*, **95,** 1428.

Skinner, G. B., and Johnston, J. L., 1951, *J. Amer. chem. Soc.*, **73,** 4549.

Stoner, E. C., 1938, *Phil. Mag.*, **25,** 899.

Wilson, A. H., 1954, *The theory of metals* (Cambridge: University Press), p. 150.

Wolcott, N. N., 1955, Conf. de Phys. des basses temps., Paris, Sept. 2–8.

The Mechanism of Quench-hardening and its Recovery in Gold†

By M. Meshii and J. W. Kauffman
Materials Science Department, Northwestern University,
Evanston, Illinois, U.S.A.

[Received September 15, 1959]

Abstract

Resoftening characteristics of quench-hardened gold were experimentally determined. Resoftening occurred above 600°c at a highly temperature-dependent rate with an activation energy of 4·7 ev. Various quench-hardening mechanisms are considered. The processes corresponding to the observed characteristics are for quench-hardening: formation of tetrahedral stacking faults; and for resoftening: the nucleation of a Shockley partial dislocation ring on any face of the tetrahedron.

§ 1. Introduction

Pure metals can be hardened by rapid quenching from high temperatures and subsequent ageing in the neighbourhood of room temperature (Maddin and Cottrell 1955, Meshii and Kauffman 1957, 1959, Kimura *et al.* 1958, 1959). All, or nearly all, of the quench-hardening is acquired during the ageing process. During the ageing, quenched-in vacancies and vacancy complexes migrate and coagulate, eventually forming lower energy configurations. Thus, the end products resulting from the vacancy migration and coagulation are considered to be the cause of this type of hardening. Various mechanisms for quench-hardening have been put forward, such as the formation of cavities along dislocation lines (Coulomb and Friedel 1956), jog formation (Maddin and Cottrell 1955), and sessile dislocation rings collapsed from vacancy platelets (Li *et al.* 1953). However, none of these proposals has been based on systematic experimental observations.

In the present work, the nature of resoftening from quench-hardening is studied. This allows a further examination of various possible hardening mechanisms. It is found that none of the above mentioned mechanisms can correspond to the observed resoftening characteristics.

Recently, Silcox and Hirsch (1959), using an electron microscope, observed, in thin foils of gold, contrast effects caused by quenching; they explained these as tetrahedral stacking faults. Hardening due to tetrahedral stacking faults was found to be consistent with the present results. The mechanism of resoftening proposed by the present authors is the formation of a new Shockley dislocation ring on any face of the tetrahedral stacking fault, which subsequently grows, finally collapsing the tetrahedron.

† Communicated by the Authors. This investigation was performed with the support of the Office of Naval Research of the United States Government.

§ 2. Experimental Procedure

The quenching methods used have been described in a previous publication (Meshii and Kauffman 1959). The samples were gold wire, 0·016 in. in diameter, of purity, as reported by the supplier, 99·999%. The purity was checked by measuring the ratio of resistivity at room temperature to that at 4·2°K. For all specimens used these ratios were between 1500 and 2500. The temperature from which the quench was begun was $1000° \pm 10°$C. The cooling rate used was 30 000°C/sec. After quenching, all specimens were aged one hour at 100°C so as to produce the maximum saturated hardening. Further ageing at this temperature did not produce detectable over-ageing. Following this ageing treatment, the specimens were annealed in an argon atmosphere at high temperatures controlled to within ± 1°C, except for a very short time interval when the specimen was placed into the furnace. However, this short interval was found to have a negligible effect on the annealing results.

§ 3. Experimental Results

Ageing at 100°C for 1 hr is sufficient to saturate at maximum hardening; no further change in mechanical properties was observed by further ageing at this temperature. After the specimens gained maximum quench-hardening, they were annealed isothermally at four different temperatures—612°C, 627°C, 642°C and 657°C—for various periods of time. These data are shown in figs. 1 and 2. A large temperature dependence of the resoftening rate is evident. The times required to reach the given yield loads of 4·0 lb and 3·0 lb are shown in the table.

Annealing temperature (°C)	Time taken to reach the yield load of 4·0 lb (hrs)	Time taken to reach the yield load of 3·0 lb (hrs)
657	0·5	1·1
642	1·2	3·0
627	3·8	8·5
612	9·8	24·0

In fig. 3, logarithms of the times in the table are plotted against the reciprocal of absolute temperatures of annealing. Two straight lines are found whose slopes yield 4·7 and 4·8 ev as the activation energy of resoftening. The activation energy found here is much larger than the activation energy for self-diffusion of gold. Further, we find that the temperature for resoftening of quench-hardening is much higher than the temperature for resoftening of gold deformed to give the same degree of hardening.

Fig. 1

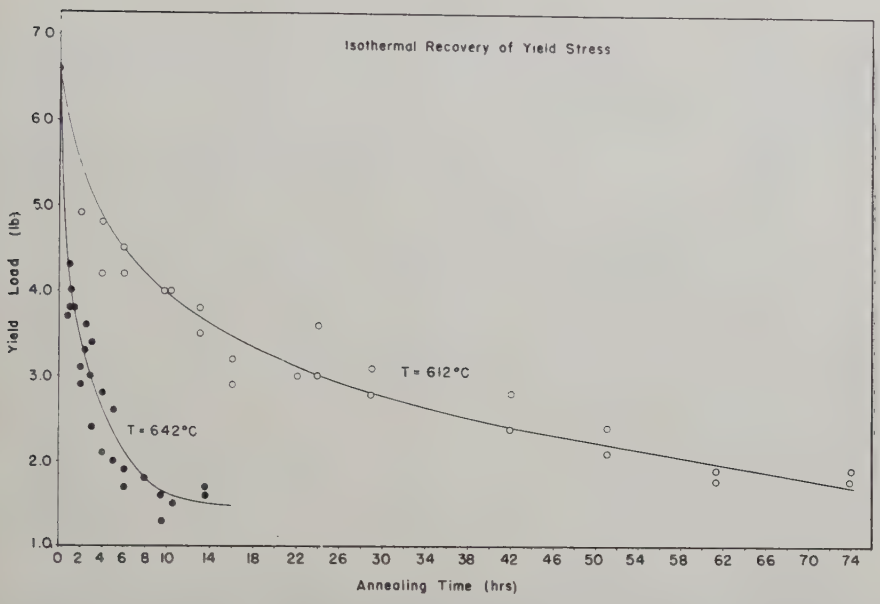

Isothermal recovery of yield stress at 612°c and 642°c. All specimens are quenched from 1000°c with an average cooling rate of 30 000°c/sec and aged at 100°c for 1 hr before annealing.

Fig. 2

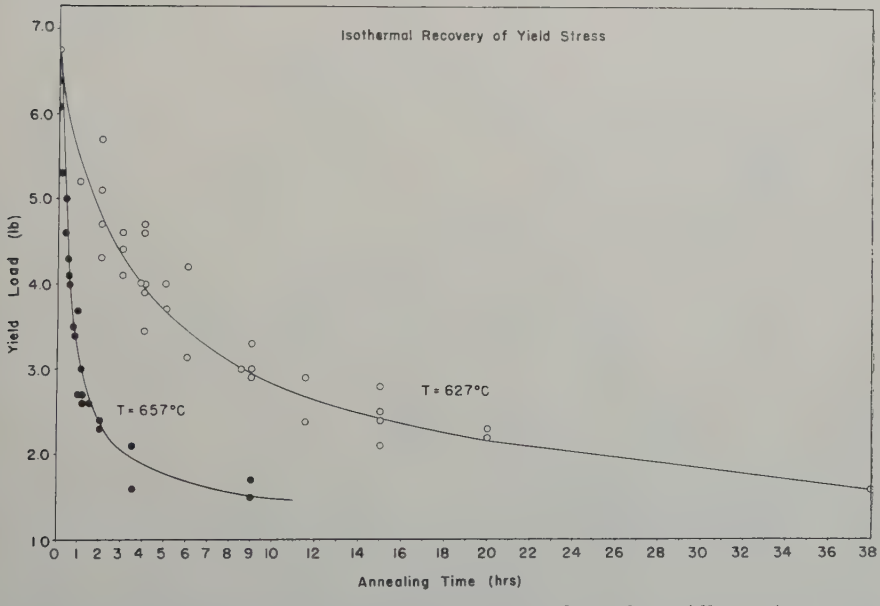

Isothermal recovery of yield stress at 627°c and 657°c. All specimens are quenched from 1000°c with an average cooling rate of 30 000°c/sec and aged at 100°c for 1 hr before annealing.

§ 4. Discussion

4.1. *Primary Characteristics*

The mechanism of quench-hardening and the mechanism of the recovery of quench-hardening must correspond to the following experimental observations:

(1) Quench-hardening is persistent at high temperature, resoftening only above 600°c, while strain hardening shows appreciable resoftening at 400°c.

(2) The resoftening kinetics exhibit an activation energy of 4·7 ev, which is much higher than that of self-diffusion in gold.

Fig. 3

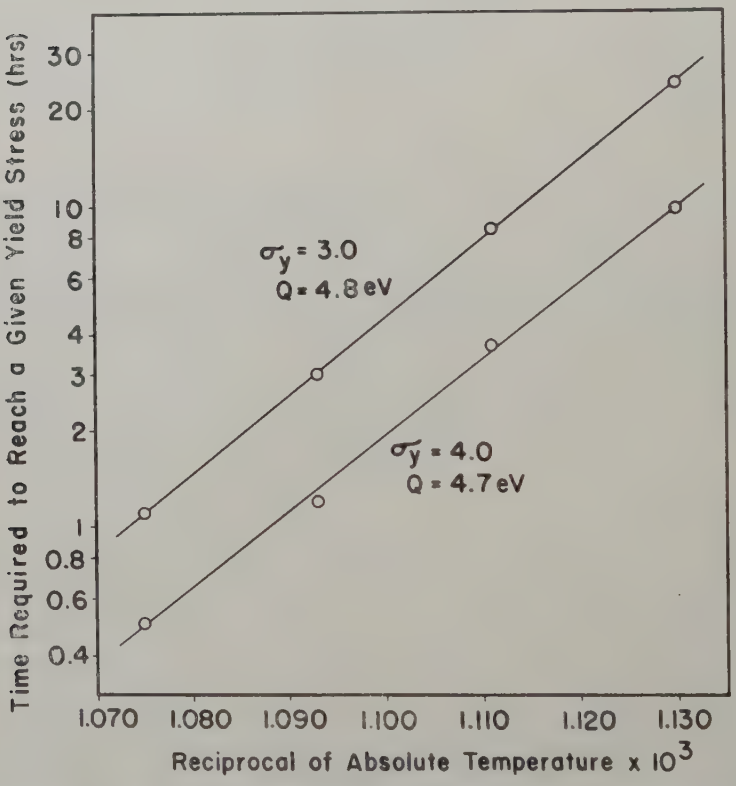

Logarithmic plot of time required to reach the degrees of recovery $\sigma_y = 3{\cdot}0$ and $\sigma_y = 4{\cdot}0$ against reciprocal of absolute temperature of annealing.

From the large activation energy for resoftening of quench-hardening and the high temperature necessary for resoftening, we conclude that the mechanism for resoftening of quench-hardening must not be diffusion controlled. The resoftening of strain hardening has generally been interpreted in terms of self-diffusion, and this has been confirmed by experimental and theoretical results, although there are still some uncertainties as to the detailed mechanism involved.

4.2. *The Mechanism Corresponding to the Observed Recovery Characteristics*

Several mechanisms have been proposed for quench-hardening. These involve various configurations resulting from vacancy condensation and are capable of producing various degrees of hardening. We may now quantitatively examine these mechanisms using the present experimental results. The possible hardening due to jogs and cavities formed along existing dislocations must be rejected as the main hardening mechanism for the quenched gold, because these would anneal out at lower temperatures with the activation energy of self-diffusion. The same consideration is valid for unextended or partially extended Frank sessile dislocations.

A possible configuration resulting from the migration and coagulation of quenched-in vacancies was recently observed (Silcox and Hirsch 1959) with an electron microscope. In gold foils they found configurations resulting from quenching, which have a tetrahedral appearance. They interpreted these configurations as being formed from triangular sheets of vacancies. The edges of the tetrahedra consist of stair-rod dislocations and the faces are intrinsic stacking fault planes. Since the stair-rod dislocation, by definition, is the intersection of two stacking fault planes, it follows that these dislocations must exist as straight line segments and the Burgers vector must not lie on the stacking fault plane to which it belongs. Therefore we reach the important conclusion that these stair-rod dislocations can neither glide nor climb by simple diffusion, and a mechanism for resoftening other than diffusion must be considered. In the following section, a mechanism for the disappearance of these tetrahedral configurations is proposed.

4.3. *The Disappearance of Tetrahedral Stacking Faults by Dislocation Nucleation*

A dislocation ring which nucleates on any face of a tetrahedron and subsequently grows and interacts with the stair-rod dislocations can annihilate the tetrahedral configuration. We consider the nucleation of a dislocation such as to eliminate the stacking fault as it grows. This removal of the stacking fault plane provides a driving force tending to increase the area of the dislocation ring. This type of dislocation would have a fault vector of the $\frac{1}{6}\langle 112\rangle$ type. After the new dislocation, which is a Shockley partial dislocation ring, is nucleated, its further growth proceeds, decreasing the energy. As this dislocation ring grows, it will eventually reach the edge of the stacking fault and then interact with the three stair-rod dislocations. Similar dislocation reactions have been proposed by Silcox and Hirsch (1959) to describe the tetrahedral formation. Three stair-rod dislocations are transformed into two Shockley partial dislocations and one Frank sessile dislocation. The resultant two Shockley partial dislocations can move so as to eliminate the two remaining stacking faults. The final configuration resulting from these reactions is a stacking fault plane surrounded by a Frank sessile dislocation. Thus, for resoftening to occur, we still must eliminate this final configuration. This

can occur now by the evaporation of vacancies out of the Frank sessile dislocation ring. Using the activation energy for self-diffusion, one can calculate the time required for this evaporation to take place. The result is only a few seconds in the temperature range where resoftening occurs. Hence the time limiting process will be the nucleation of the original dislocation on the stacking fault plane. It is now necessary to consider in more detail the nucleation of this dislocation to see if it corresponds to the observed experimental data.

The analysis for the case of the nucleation of a dislocation ring under an external force has been made by Cottrell (1953). Using his method we have extended the calculations to the present case, which gives both the critical size for the nucleation of a Shockley partial dislocation ring on the stacking fault plane and also the activation energy required for the nucleation. Using 40 erg/cm^2 as the stacking fault energy, $4{\cdot}8 \times 10^{-7}$ cm is found for the critical radius and 6·6 ev is found for the activation energy. This calculated activation energy is in reasonable agreement with the experimentally observed value of 4·7 ev. Further, the probability of nucleation must be proportional to the area of the stacking fault and therefore to the number of tetrahedral stacking faults. Then, a first order reaction should be observed for the disappearance of the tetrahedral stacking faults and hence for their resoftening process. Here again we find agreement with the experimental data to within experimental error.

4.4. *The Case of Extended Frank Sessile Dislocations*

In the § 4.2, the Frank sessile dislocations were considered to be unextended; however, it is possible that these dislocations exist as extended dislocations and we now consider the more complex mechanisms for their removal. In the case of totally extended Frank sessile dislocations, the extended partials must combine before vacancy evaporation can take place. Then the activation energy for the disappearance of the configuration is the sum of the energies, namely, self-diffusion plus the energy difference between extended and unextended dislocations. The shape of extended Frank sessile dislocations is generally triangular. The evaporation of vacancies is most likely to take place from an apex of the triangle, because the length of the dislocation is thus shortened instead of lengthened, and because the energy for dislocation recombination is the lowest at an apex of a triangular ring. The activation energy for recombination of extended dislocations is estimated to be much smaller than that of self-diffusion for this case†.

The nucleation of a Shockley partial dislocation on the stacking fault region is an alternative mechanism for the elimination of extended Frank sessile dislocations. The stacking fault region inside a Frank sessile dislocation has the same probability of nucleation as a stacking fault on a tetrahedron. If this process should occur, the Frank sessile dislocation

† Appendix.

will be converted to a glissile dislocation of the $\frac{1}{2}\langle 110\rangle$ type. However, the vacancy mechanism is more likely, due to its lower activation energy.

4.5. *Consideration of the Size of the Tetrahedra*

Let us next consider the effect of the size of the tetrahedra. When tetrahedra are smaller than a critical size, they become more stable than triangular rings of Frank sessile dislocations. Then a mechanism other than the nucleation of a Shockley dislocation ring must be considered for the elimination of these tetrahedra. Extended jogs have been considered previously (Silcox and Hirsch 1959). The energy to form a jog on a tetrahedron will be considerably larger than the activation energy for the present recovery mechanism. On the other hand, as shown in the present experimental results, a sudden recovery of quench-hardening occurs over a narrow temperature range with a distinct activation energy of 4·7 ev and no hardening effect remains after this recovery. These facts in conjunction with the above consideration lead us to conclude that the tetrahedra smaller than a critical size are unimportant for the mechanism of quench-hardening and its recovery in gold.

Acknowledgments

The authors wish to acknowledge the discussions and the suggestions of Professor J. Takamura of Kyoto University, and Professor R. Thomson of the University of Illinois.

They would also like to thank Professor A. Kelly of Cambridge University for reading this paper.

APPENDIX

The Energy of Recombination of an Extended Frank Dislocation

The repulsive force between the partial dislocations is

$$F=\frac{\mu(\mathbf{b}_1\,.\,\mathbf{b}_2)}{2\pi(1-\nu)d}$$

where $(\mathbf{b}_1\,.\,\mathbf{b}_2)$ is $a^2/18$ in the case of Frank sessile dislocation. This force must balance the surface tension due to the stacking fault at $d=d_0$

$$\frac{\mu a^2}{36\pi(1-\nu)d_0}=\gamma,$$

$$d_0\gamma=\frac{\mu a^2}{36\pi(1-\nu)}.$$

The energy required to recombine an extended Frank dislocation consists of two terms, E_d and E_γ.

The segments of ΔL of Shockley and stair-rod dislocations recombine to ΔL of Frank dislocation. Then energy change is

$$E_d=\frac{\mu a^2}{36\pi}\log\left(\frac{r}{r_0}\right)\Delta L.$$

By the recombination of the segment ΔL, the area $\Delta L \cdot d_0$ of the stacking fault is eliminated. The energy due to this is

$$E_\gamma = -\gamma d_0 \cdot \Delta L.$$

Thus the total energy change is

$$E = E_d + E_\gamma = \left[\frac{\mu a^2}{36\pi} \log\left(\frac{r}{r_0}\right) - \gamma d_0 \right] \Delta L = \left[\frac{\mu a^2}{36\pi} \log\left(\frac{r}{r_0}\right) - \frac{\mu a^2}{36\pi(1-\nu)} \right] \Delta L.$$

The total energy change per an atomic distance is only 0·2 ev, where we have used $\mu = 2{\cdot}8 \times 10^{11}$ erg/cm^3, $a = 4{\cdot}08 \times 10^{-8}$ cm, $r = 430 \times 10^{-8}$ cm, and $r_0 = 5{\cdot}77 \times 10^{-8}$ cm. The evaporation of vacancies from a triangular ring of Frank sessile dislocation is most likely to take place from its apex. The recombination over two atomic distances is sufficient for a vacancy to evaporate. Hence it is evident that this energy will be considerably smaller than the activation energy of self-diffusion, even though some approximations have been used in the above calculation.

References

Cottrell, A. H., 1953, *Dislocations and Plastic Flow in Crystals* (Oxford: Clarendon Press), p. 53.

Coulomb, P., and Friedel, J., 1956, *Dislocations and Mechanical Properties of Crystals* (Lake Placid Conference) (New York: John Wiley and Sons, Inc.), p. 555.

Kimura, H., Maddin, R., and Kuhlmann-Wilsdorf, D., 1958, *Bull. Amer. phys. Soc.*, **3,** 125; 1959, *Acta Met.*, **7,** 154.

Li, C. H., Washburn, J., and Parker, E. R., 1953, *J. Metals*, **5,** 1223.

Maddin, R., and Cottrell, A. H., 1955, *Phil. Mag.*, **46,** 735.

Meshii, M., and Kauffman, J. W., 1957, *Bull. Amer. phys. Soc.*, **2,** 145; 1959, *Acta Met.*, **7,** 180.

Seeger, A., 1955, *Defects in Crystalline Solids* (London: Physical Society), p. 391.

Silcox, J., and Hirsch, P. B., 1959, *Phil. Mag.*, **4,** 72.

Unloading Effects in Aluminium and Aluminium–Zinc Single Crystals†

By A. T. Thomas
Aluminium Laboratories Limited, Banbury, Oxon, England

[Received March 28, 1960]

Abstract

Interrupted tensile tests have been carried out on single crystals of super-purity aluminium and solid solutions of aluminium–zinc. Partial load removal during an interruption of the test is shown to have several effects on subsequent plastic flow. Unloading yield points are formed during tests on both alloy and aluminium specimens, while strain ageing yield points formed during tests on alloy specimens are shown to be either enhanced or diminished, depending on the sequence of prior ageing and unloading. Finally the relationship between unloading and room temperature recovery is examined and the results suggest that the trapping of glissile dislocations, as a result of unloading, leads to a partial suppression of recovery.

§ 1. Introduction

Experimental work at different times has demonstrated that non-elastic and irreversible effects can occur when alloys and pure metals are unloaded during interruptions of tensile tests. Holden and Kunz (1952) showed how strain ageing yield points in iron are decreased in magnitude if the ageing takes place under reduced load. Their interpretation followed a suggestion by Fisher that the anchoring of a dislocation by solute atoms is more efficient if the former is in a stressed or bowed condition than if relaxed. An alternative suggestion by Paxton (1953) emphasized the sensitivity of the upper yield point to various experimental factors leading to stress concentrations. Thus the unloading is likely to disturb axiality of the specimen leading to a reduced yield point.

Another effect of unloading has been reported by Haasen and Kelly (1957) and Makin (1958) who observed the existence of yield points during tensile tests on single crystals of, respectively, high-purity aluminium and nickel, and copper, as a result of unloading during interruptions of the tests. The characteristics and mode of occurrence of these yield points suggest that strain ageing is an unlikely explanation for their formation. The yield points occur only if some of the load is removed during an interruption of test and their magnitude increases with extent of unloading. The effect is absent at low strains, occurring only after the termination of

† Communicated by the Author.

the region of easy glide, and its magnitude increases with strain. The yield point magnitude is independent of the waiting period and the yield points occur equally well at liquid air temperatures. These observations have suggested a process in which the glissile dislocations run backwards and trap one another during unloading.

An examination of yield points in α-brass and other face-centred cubic metals by Bolling (1959) has indicated the formation of unloading yield points to be a general feature of face-centred cubic metals at temperatures where recovery is not appreciable. This work also confirmed that the magnitude of the strain ageing yield point is a function of the stress on the specimen during ageing, and ageing under reduced stress decreases the yield point. Finally, Bolling has shown that combining ageing with unloading produces interesting yield effects which he attributes to a combination of both processes.

The present study was undertaken to examine the general effects of unloading during interruptions of tensile tests on single crystals of high-purity aluminium and dilute aluminium–zinc alloys. The conditions were, therefore, examined under which yield points in alloy crystals could be enhanced or suppressed as a result of prior unloading.

§ 2. Experimental Procedure

The materials used were super-purity aluminium (99·996%) and high-purity alloys of aluminium–0·42 at. % zinc and aluminium–0·2 at. % zinc. The alloys were made by melting together super-purity aluminium and 'Crown Special' zinc (99·986%) kindly supplied by the National Smelting Company, Avonmouth. The melting furnace was an alumina-lined crucible heated in an electrical resistance furnace, and the melt was chill cast in an iron mould producing an ingot 0·75 in. diameter × 4 in. in size. After discarding the head and tail the remainder of the cast ingot was heated for 4–5 hours at 450°C, and then extruded to $\frac{1}{8}$ in. diameter wire using a miniature extrusion press operated by an Amsler tensile testing machine. Wire drawing from $\frac{1}{8}$ in. diameter to 0·064 in. diameter was carried out using a simple draw bench. Single crystals were prepared from the drawn wire by the strain anneal method and wire crystals of approximately 5 cm in length were sectioned by a strain-free electro-erosion technique. To facilitate loading in the tensile machine, small polycrystalline loops of aluminium or the appropriate alloy were attached to the ends of the crystal by local welding, leaving a 4 cm working length. The orientation of each crystal was measured by the Laue back-reflection method and is shown in fig. 1.

Tensile tests were performed at a strain rate of 2×10^{-5} per sec in an Instron tensile testing instrument which is a recording hard beam machine. The load was measured by a load cell and the elongation by the cross-head motion. Tests were carried out either at room temperature or at 90°K with the specimen immersed in a Dewar flask containing liquid air.

In order to estimate the proportion of the applied load removed during an unloading test, a calibration test was carried out on a dummy specimen at a strain rate of 2×10^{-5} per sec to determine the rate of unloading. This was measured and found to be approximately 3 kg/min for a cross-head speed of 0·005 cm/min.

Fig. 1

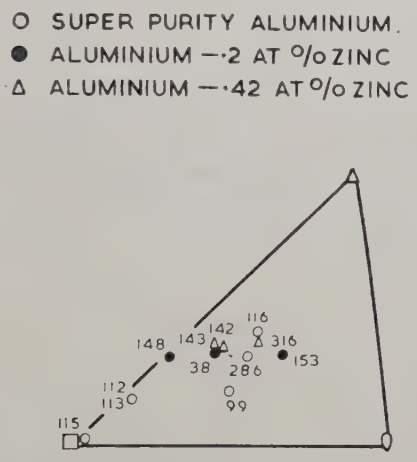

Initial orientations of the tension axes of the crystals examined.

§ 3. General Effects of Unloading

To appreciate the influence of unloading on such processes as recovery and strain ageing, it is first necessary to observe the deformation behaviour of specimens under conditions of no deliberate unloading during the interruption periods.

3.1. *Interruptions Without Unloading*

These tests were carried out to show the general nature of the strain ageing yield points in dilute aluminium–zinc alloys, and also to demonstrate some effects of room temperature recovery. A wire single crystal of aluminium–0·2 at. % zinc was strained plastically at room temperature. At frequent intervals the test was stopped and restarted after a time interval of 5 min. No load was deliberately removed during the interruption, but some creep relaxation usually occurred. This relaxation never exceeded 10% and was usually much less. Whenever a yield point was found (in this and subsequent tests) the magnitude of the yield point (Δl) and the change in flow stress (Δh) were measured. These quantities are illustrated in fig. 2.

A typical example of the relationship between the parameters Δh, Δl and load (l) on specimen for such an interrupted test is shown in fig. 3 for specimen T153 (aluminium–0·2 at. % zinc). Yield points, which at small extensions and small loads were well developed, decreased with increase of load. At a load of 4·2 kg, which corresponded to an elongation

of 20%, the yield point no longer occurred. At the same time, small and positive increases in flow stress (Δh) which occurred at small loads, gradually changed to large negative values at high loads indicating a softening of the crystal during the period of interruption at this stage of the test.

Fig. 2

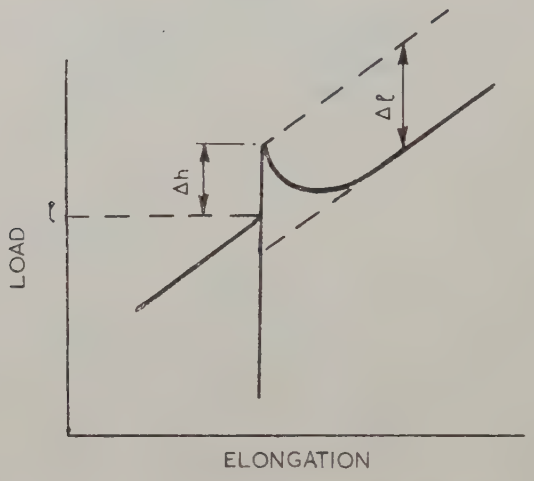

Illustrating the method adopted for measuring the magnitude of a yield point (Δl), and the change in flow stress (Δh) at a value of load (l) where the tensile test is interrupted.

Fig. 3

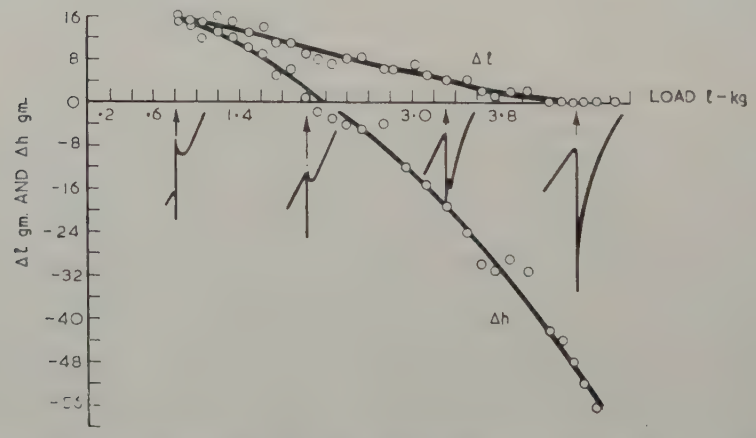

The variation of yield point (Δl) and flow stress (Δh) with load (l) expressed graphically and diagrammatically for alloy crystal T153 tested at 295°K.

Similar tests on a super-purity aluminium crystal specimen produced no yield points and no initial increases in flow stress, but progressive softening of the crystal again occurred.

Tests at 90°K produced no yield points and no softening in either specimen.

3.2. *Unloading During Interruptions*

The relation between Δl and load for an alloy crystal when a constant proportion (75%) of the load is removed and replaced during each constant time interval (5 min) is shown in fig. 4, again using specimen T153 (aluminium–0·2 at. % zinc) tested at room temperature as a typical example. After interruptions, small strain ageing yield points were obtained at the beginning of the test. These decreased with increase of load and became zero at a load of 1·2 kg. At 1·4 kg a yield point reappeared. Initially this was very small and rounded in appearance, being no more than a small undulation in the load/extension curve. As the test proceeded, the yield points became larger and sharper, but never as abrupt as the initial strain ageing yield points.The difference in appearance of the two types of yield point are well shown in fig. 6, where test (*a*) produces a strain ageing yield point and test (*g*) gives rise to an unloading yield point.

Fig. 4

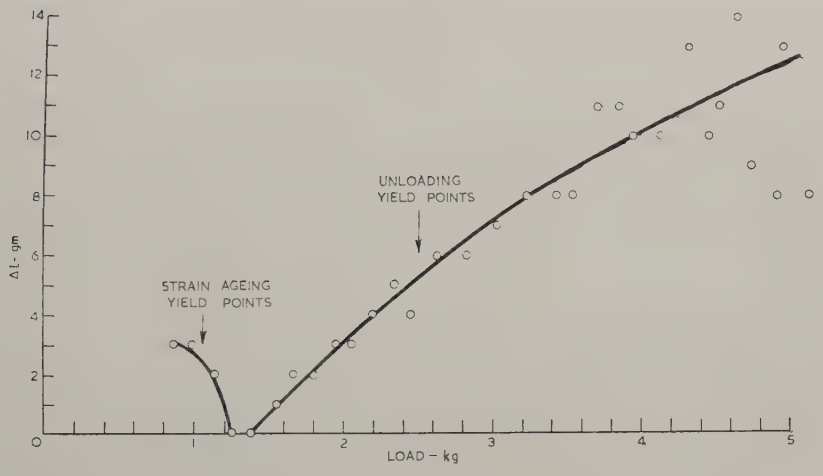

The variation of strain ageing yield point and unloading yield point (Δl) with load (l) for alloy crystal T153 tested at 295°K with 75% of applied load removed and reapplied during each 5 min interruption.

Tests on super-purity crystals indicate a similar yield point development with increase in load. A notable difference is the absence of any strain ageing yield point which is present in an alloy crystal. At liquid air temperature (90°K) yield points which develop as a result of unloading are very much larger than at room temperature for both alloy and aluminium crystals, whilst strain ageing yield points are absent at this temperature.

Unloading yield points were never observed during the easy glide or Stage I regions of the load-extension curves which is in agreement with the observations on copper single crystals by Makin (1958). It was further

Fig. 5

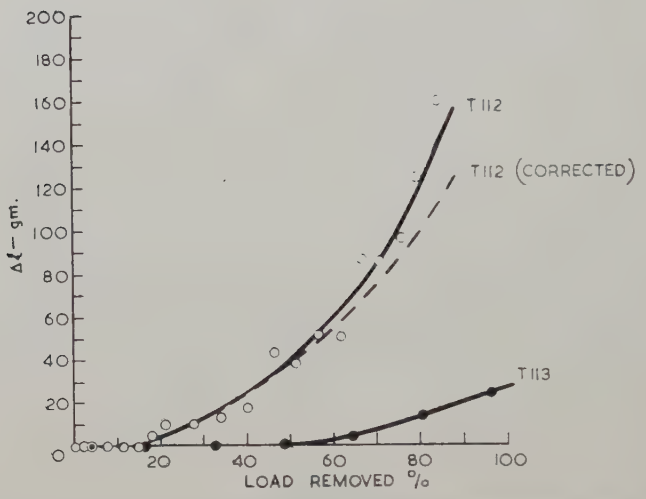

The variation of unloading yield point (Δl) with percentage load removed for the aluminium crystals T112 tested at 90°K and T113 at 295°K for time intervals of 5 min.

Fig. 6

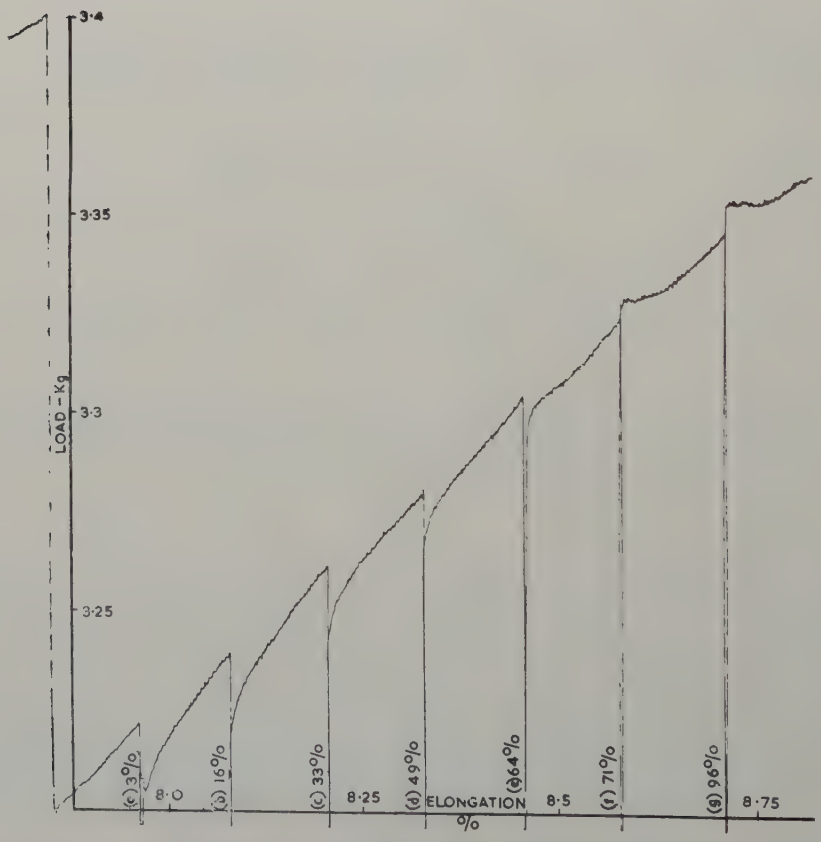

Region of a load-elongation curve for alloy crystal T142 showing a series of interruptions at constant time intervals of 3 min during which increasing percentages of load were removed and reapplied.

noted that there was a tendency for unloading yield points to appear earlier for those crystals orientated to give high rates of work hardening than for those which exhibited two-stage hardening. This indicates that the amount of cold work is an important factor for the appearance of this effect.

The results of these tests have shown that the size of the unloading yield point is dependent on the amount of load on the specimen. Other tests show that it is also dependent on the proportion of load removed in the manner illustrated in fig. 5, which shows this relationship for the aluminium crystals T112 tested at 90°K and T113 tested at 295°K. The curve for specimen T112 has been corrected to take into account the increase in the unloading yield point as a result of the increase in applied load during the test. The increase in applied load during the test at 295°K on specimen T113 was sufficiently small for this correction to be unnecessary.

In the case of the alloy crystal T153, it is possible by a study of figs. 3 and 4 to choose a load region where the strain ageing yield points are still present with the load maintained (e.g. for loads less than 4·2 kg in fig. 3), and where unloading yield points would also occur by partly removing the load during the interruption (e.g. for loads greater than 1·4 kg for 75% load removal in fig. 4). Thus in the load region between 1·4 and 4·2 kg, a sequence of interruptions with increasing load removals should produce both kinds of yield points in the subsequent plastic flow.

Figure 6 is a reproduction of an actual trace made by the recorder of the tensile machine during such a test on the alloy crystal T142 at 295°K in the load range 3·2–3·4 kg. As the proportion of load removed during the constant time interval of 3 min increased from (*a*) 3% to (*g*) 96%, the following sequence was observed:

(*a*) 3% A small sharp yield point was accompanied by a fall in flow stress.

(*b*) 16% The yield point vanished but the fall in flow stress remained.

(*c*) 33%
(*d*) 49% The fall in flow stress was becoming noticeably smaller.

(*e*) 64% The flow stress on retesting was much the same as before the interruption.

(*f*) 71% A rounded load drop was accompanied by an increase in flow stress.

(*g*) 96% Complete load removal during the interruption produced a further increase in flow stress accompanied by a large but rounded yield point.

Thus, gradually increasing load removals during constant time intervals produced, on one hand, a small sharp yield point and a softening of the crystal when the load was maintained, and on the other hand, a large rounded yield point and a hardening when most of the load was removed.

The time intervals of each interruption in this test was kept constant at 3 min. If the process responsible for the initial softening of the crystal was not taking place during unloading and reloading, it might be argued that waiting times should not include the time taken to unload and reload. If this were the case, the increasing proportion of the 3 min interval taken up by unloading and reloading would explain the gradual decrease of softening. To examine this contention, two tests (p) and (q) were carried out to compare the effect of maintaining the load for a 3 min interruption, (test p) and removing 92% of the load, waiting 3 min and reloading, (test q). The waiting period of 3 min did not, in the case of test (q), include the time of unloading and reloading. These tests are shown in fig. 7 for the alloy crystal specimen T142 tested at 295°K. The results of tests (p) and (q) are similar to those of tests (a) and (g) in fig. 6, and they indicate that the time taken to unload and reload is not related to the behaviour described.

Fig. 7

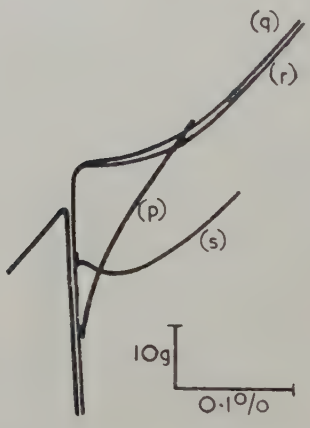

Composite diagram of the load-elongation relationships for alloy crystal T142 in the ranges 3·4 to 3·5 kg load and 9·25 to 10·0% elongation after the following tests at 295°K.

(p) Interruption of 3 min with 3% of load removed.
(q) Remove 92% of the load, wait 3 min and reload.
(r) Remove 92% of the load and reload where the total interruption time is 3 min.
(s) Remove 92% of the load, wait 60 min and reload.

This conclusion was confirmed by test (r), fig. 7, in which the 3-min time interval included the time taken to unload and reload, and the subsequent hardening and load drop produced was the same as for test (q). For long time intervals softening does occur even with the load removed. Test (s), fig. 7, shows that softening has occurred after a 60 min interval with 92% of the load removed. However, the rate of softening under these conditions is very much slower than with the load maintained.

§ 4. Summary of Results

An interrupted tensile test with the load maintained during the interruption produced the following effects on retesting.

(*a*) Sharp yield points were obtained with alloy crystals tested at room temperature. The magnitude of the yield point decreased with increase in applied load and eventually disappeared. No yield points were obtained with super-purity aluminium crystals or with aluminium alloy crystals tested at 90°K.

(*b*) A progressive softening of a specimen tested at room temperature, indicated by a fall in flow stress, occurred for both alloy and super-purity aluminium crystals. The effect increased with increase in applied load, and with time of interruption; it has to be noted, however, that at 90°K the effect did not occur. No softening was observed during tests at 90°K.

An interrupted tensile test with the load partly removed during the interruption produced the following effects on retesting.

(*a*) The sharp initial yield points were suppressed. The degree of suppression increased with increase of proportion of load removed and as the series of tests progressed to high loads.

(*b*) Softening at large extensions was diminished by load removal; this effect increased with increase of the proportion of load removed.

(*c*) At a certain value of applied load, large load removals completely prevented room temperature softening and, in fact, caused a hardening. Associated with the hardening was a large, but rounded, yield point, and this occurred with both alloy and aluminium specimens. This yield point increased and sharpened with the proportion of load removed and with the extent of prior cold work of the crystal.

(*d*) For crystals of different orientation, the onset of the unloading yield point occurred at lower extensions for crystals that work harden appreciably than it did for crystals which show easy glide. The unloading yield point did not occur until after the easy glide region.

(*e*) Unloading yield points were much larger and developed more easily during tests at 90°K than at 295°K.

(*f*) The magnitude of the unloading yield point was independent of time of interruption, but the hardening associated with it decreased with increase of waiting time at room temperature.

§ 5. Discussion

From the nature of the results, it is clear that a distinction must be made between two types of yield points. The initial sharp yield point, which occurred at low loads with the load maintained during the waiting period, has certain characteristics which indicate that it is a true strain-ageing yield point dependent on the presence of solute atoms for its occurrence.

It occurred only in the aluminium alloy crystals and not in the super-purity aluminium crystals; furthermore it occurred during tests at room temperature and not during tests at 90°K; it decreased with removal of load during the interruptions. Figure 6 shows the transition from the strain-ageing yield point to the unloading yield point as the load maintained on the specimen during a constant waiting time is gradually decreased.

The currently held theory of the strain-ageing yield point is due to Cottrell (1953). At temperatures at which solute atoms (zinc atoms in the case of the alloys used in this investigation) are able to diffuse through the crystal lattice, they will be attracted to positions of low energy adjacent to dislocations, where they form atmospheres which act as barriers to subsequent dislocation movement. Thus, the stress required to initiate slip is greater than that required to maintain slip, and a load relaxation will occur at the onset of plastic flow.

The softening of a crystal which occurs as a result of an interruption at room temperature after appreciable cold work is undoubtedly a recovery effect. It is well known that cold-worked aluminium and dilute aluminium alloys will recover at room temperature.

As a result of unloading, the formation of the unloading yield point, and the suppression of the recovery softening process, appear to be complementary effects, as revealed in fig. 6.

Haasen and Kelly (1957) explain the formation of the unloading yield point by suggesting that sessile dislocations are formed through the interaction of dislocations running back on intersecting slip planes as a result of unloading. The consequent anchoring of glissile dislocations would give rise to a yield point on retesting. The initial appearance of the unloading yield point only after the termination of the Stage I region of the stress–strain curve gives support to this mechanism. It is suggested that this explanation can be extended to account for the suppression of recovery softening which occurs at room temperature. With the load maintained the applied stress acting on the dislocations is balanced by the action of the back stress due to neighbouring dislocations. Thermal energy is sufficient to cause a re-distribution of dislocations forming a fairly well defined dislocation network. This would lead to a reduction in flow stress. The recovery process at room temperature cannot take place to the same extent if unloading has occurred, due to the anchoring of dislocations in the way described.

§ 6. Unloading, Strain Ageing and Recovery

The tests described in the previous sections have distinguished between two types of yield point and have shown a relationship between the development of an unloading yield point and the flow stress associated with it. The tests to be described in the present sections were carried out to examine more closely the connection between unloading, recovery and strain ageing by combining unloading and reloading with a waiting period

at load. Tests were carried out on both alloy and aluminium specimens at both room and liquid air temperatures. This procedure enabled the distinction to be made between yield points due to strain ageing and those due to unloading.

The testing procedure was as follows:

A specimen was strained at 295°K to 16–17% extension; the test temperature was then changed to 90°K. The stress-elongation curves for these two temperatures are shown in fig. 8. The test was frequently interrupted to carry out the following four separate tests, generally in the sequence given.

Test 1. The test was stopped and restarted after a time interval of 5 min. No load was deliberately removed during the interruption.

Test 2. The test was stopped for the purpose of removing a large percentage of the applied load which was re-applied immediately to continue the test.

Test 3. The test was stopped for an interval of 5 min. The specimen was then unloaded and reloaded immediately to continue the test.

Test 4. The test was stopped, the specimen unloaded and immediately reloaded nearly to the onset of plastic flow when an interval of 5 min was allowed to occur before the test was continued.

The diagrammatic illustration of each test is included in fig. 9. The extent of unloading in Tests 2, 3 and 4 was usually 80–90% of the applied load.

A number of crystals were tested according to the above programme and the results obtained from the super-purity aluminium specimen T286 and the aluminium–0·42 at. % zinc specimen T316 are typical. Figure 8 shows the initial orientation of these crystals together with their overall stress-elongation curves for extensions, partly at 295°K and partly at 90°K. The results of the four tests at each of the positions A, B and C, fig. 8, are illustrated in fig. 9, which is a reproduction of the load-extension curves obtained directly from the recorded chart. The details of these tests are shown in the table, which gives the load and elongation values at the commencement of each test; the load and elongation ranges over which these tests extended; and the percentage load removed where applicable. The results and interpretation of these tests are presented below in detail with reference to fig. 9.

6.1. *Super-purity Aluminium Specimen T286*

Position A

At small extensions, little or no room temperature recovery is occurring, and this would account for the absence of softening in Test 1. Tests 2, 3 and 4 indicate that unloading is having very little effect at this stage.

Fig. 8

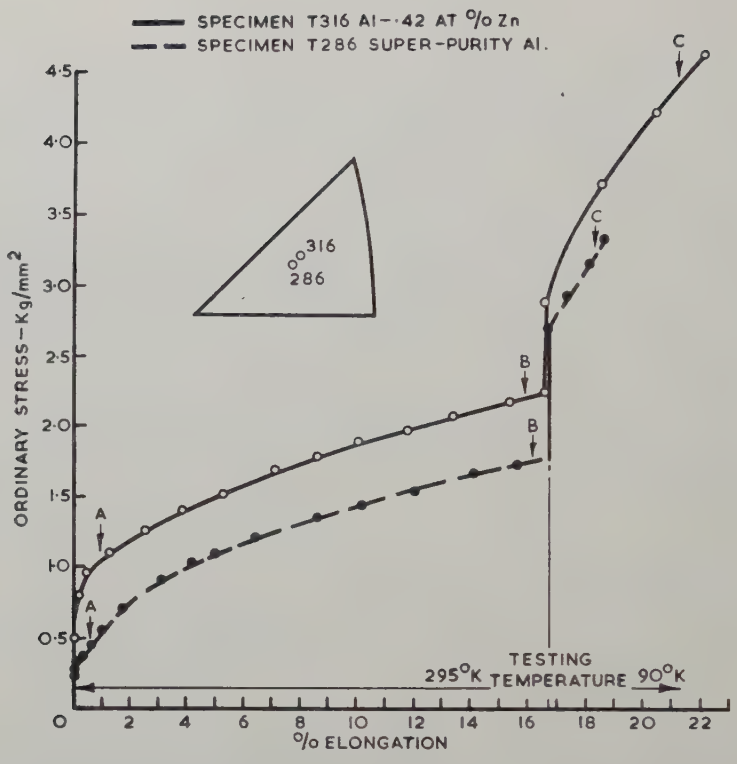

Stress-elongation curves for crystals tested at 295° K and 90°K.

Fig. 9

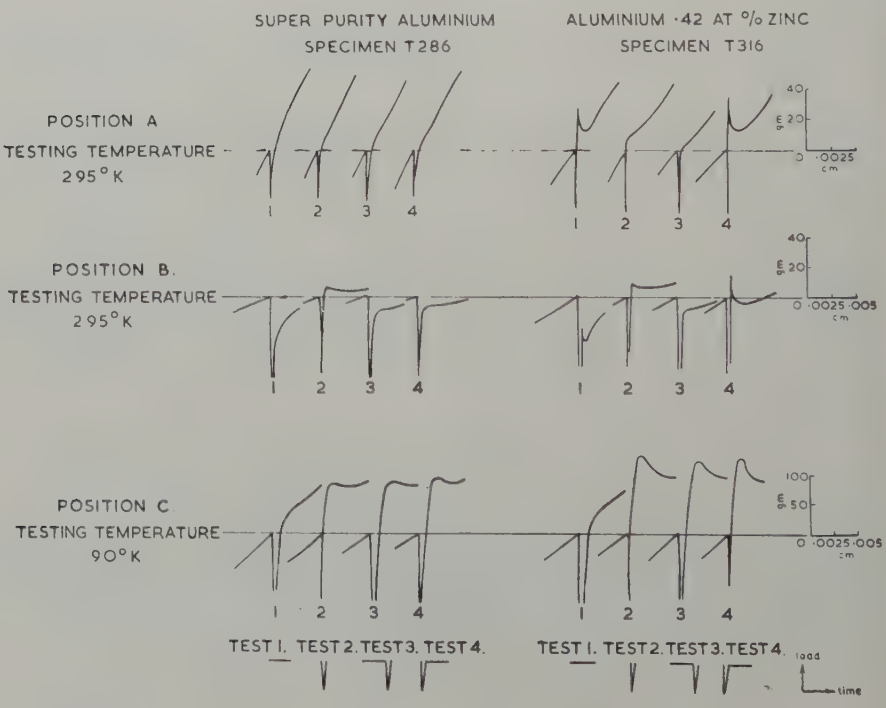

Load-extension relationships on retesting after a variety of tests performed during interruptions of tensile tests on super-purity aluminium and aluminium–zinc single crystals.

Position B

After some 16% elongation, the behaviour is now very different. Waiting 5 min without unloading (Test 1) produces a large fall in flow stress on retesting, which is indicative of the large amount of stress-assisted recovery occurring at room temperature at this extension. Unloading and reloading immediately (Test 2) produces a typical unloading yield point together with an absence of recovery softening indicated by an increase in flow stress. Tests 3 and 4, which combine a 5 min wait either before or after unloading and reloading, produce less well-developed unloading yield points with flow stresses intermediate between those obtained in Tests 1 and 2. The negligible effect of unloading during the tests at position A might be attributed to an insufficient number of intersecting slip planes present after this small extension, and the corresponding small number of blocked dislocation groups present. The trapping of dislocations as a result of unloading would tend to inhibit their movement and rearrangement associated with recovery, leading to the observed suppression of recovery softening. The intermediate flow stress values after Tests 3 and 4 suggest that some recovery is occurring after unloading and reloading (Test 4), while waiting 5 min before unloading and reloading allows slightly more recovery to occur as indicated by the slightly lower flow stress after Test 3 than after Test 4.

Position C

The same sequence of tests carried out at 90°K shows no recovery softening during Test 1, while all other tests involving unloading produce, on retesting, large unloading yield points. The similarity of results for Tests 2, 3 and 4 shows that the incorporation of a 5 min waiting period, whether before or after unloading and reloading, does not substantially affect the shape or size of the unloading yield point.

6.2. *Aluminium–0·42 at. % Zinc Specimen T316*

Position A

The main difference between the tests on the alloy specimen after a small extension compared with the corresponding tests on the super-purity specimen is the occurrence of large yield points after both Tests 1 and 4. It is noticeable that no yield points occurred after Tests 2 and 3, indicating that unloading and reloading prevents strain ageing from occurring, or as in the case of Test 3, unloading and reloading after an ageing period suppresses the occurrence of the yield point. This is in accord with earlier observations that unloading reduces the size of strain ageing yield points, the effect being greater for increased load removals and increase in specimen extension.

The occurrence of the large yield point after Test 4 shows that a 5 min ageing after unloading and reloading results in a larger yield point than is obtained by ageing for 5 min without unloading as in Test 1. Even for

these small extensions, some recovery is already occurring as shown by the small difference in flow stress between Test 1 and Test 4 and also between Test 2 and Test 3.

Unloading prevents the strain ageing yield point from occurring, even when an ageing period has occurred prior to unloading. This suggests that (as a result of the removal of the applied load) the running back of dislocations along slip planes (under the action of the back stress of neighbouring dislocations) is sufficient to dissociate the dislocations from their solute atom atmospheres formed during the prior ageing period.

Position B

Test 1 illustrates two aspects of recovery which are occurring after an elongation of 16% at 295°K. These are the fall in flow stress and the reduction in size of the strain ageing yield point in comparison with the yield points obtained after tests at position A where little or no recovery was occurring. The association of these two aspects of recovery and their increase with increase in crystal extension has been observed earlier (fig. 3). It is suggested that the dislocation network formed during recovery becomes saturated with solute atoms. This would have the effect of decreasing the available solute concentration for anchoring the potential glissile dislocations, giving rise to the observed decrease in yield point size.

Unloading and reloading without waiting (Test 2) produces a yield point very similar to that produced after Test 2 at position B for the pure aluminium specimen. The size and shape of this unloading yield point can be directly compared with the larger and more abrupt strain ageing yield point.

Unloading and reloading after an ageing period (Test 3) again prevents the strain ageing yield point from occurring and a reduced unloading yield point occurs accompanied by a flow stress intermediate between those obtained after Tests 1 and 2.

Test 4 shows that a large yield point can be obtained if ageing is preceded by unloading and reloading. This might be explained, at least partly, by the suggested suppression of recovery by unloading, allowing more solute atoms to be locally available for anchoring the glissile dislocations. That this is not the complete explanation can be appreciated by reference to fig. 10, which shows how yield points arising from the four tests develop with stress for the alloy crystal during the room temperature deformation. Curves 1 and 4 represent the relationship between stress and the magnitude of the yield points formed as a result of Tests 1 and 4. Both curves rise to a maximum very soon after the initial yield point and subsequently decrease with stress. Curve 4 is substantially higher than curve 1 at all stresses. This means that yield points arising from Test 4 are considerably larger than those after Test 1, even at low stresses where recovery effects are not yet appreciable. The principal cause of the large yield point after Test 4 is, therefore, more likely to be some combination of both unloading and ageing,

such as the ageing of sessile dislocations formed by prior unloading as proposed by Bolling (1959) in the case of α-brass. In contrast to curves 1 and 4, curves 2 and 3 are typical of the development of essentially unloading yield points and which correspond to the development of the unloading yield point shown in fig. 4. Curve 3 is lower than curve 2 due to the recovery softening occurring during the 5 min wait before unloading and

Fig. 10

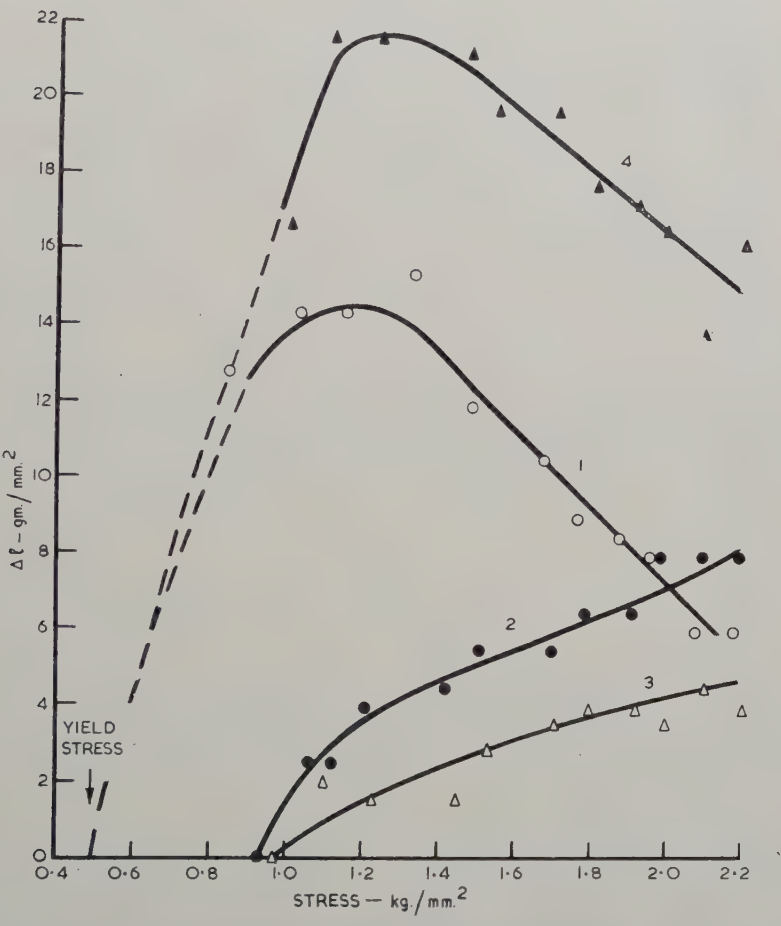

The variation of yield point size (Δl) with stress after Tests 1, 2, 3 and 4 performed during interruptions of tensile tests at 295°K on alloy crystal T316.

reloading. It can also be seen in fig. 10 that curve 4 does not fall off at high stresses quite so fast as curve 1, although the difference is small. It might be expected that the difference would be greater if recovery was being appreciably reduced by prior unloading and reloading. In contrast, fig. 11 shows how changes in flow stress (Δh) vary with stress for the same tests.

Curve 1 falls away considerably faster than curve 4. A further indication of the importance of unloading on recovery is shown in fig. 12, which expresses the change in flow stress as a function of time of interruption of a series of tests performed on specimen T143 after 15% elongation at room temperature. It is seen that if unloading and reloading precedes the

Fig. 11

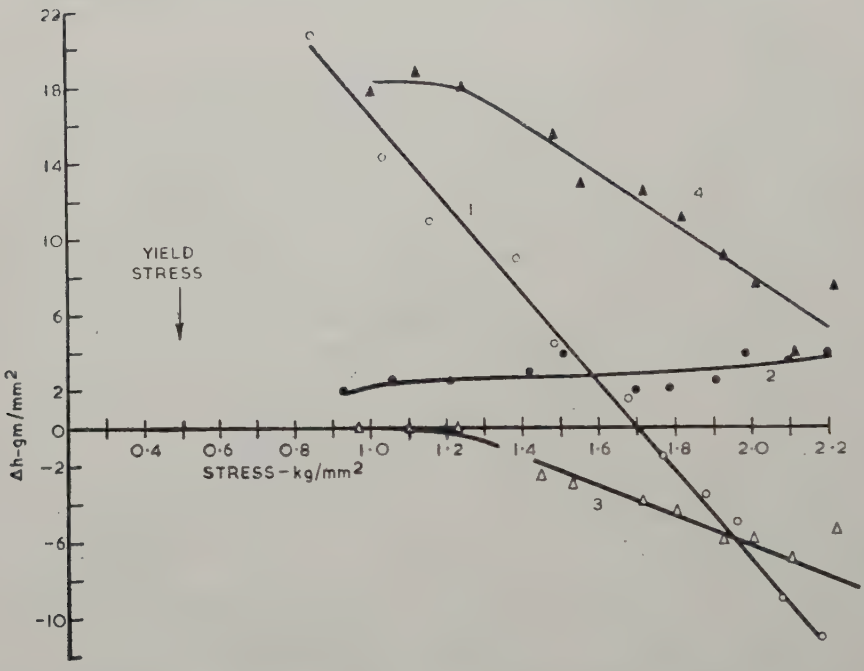

The variation of changes in flow stress (Δh) with stress after Tests 1, 2, 3 and 4 performed during interruptions of tensile tests at 295°K on alloy crystal T316.

waiting period, the subsequent recovery softening is considerably reduced. Hence, it is likely that part of the explanation for the large yield point obtained after Test 4 at large (specimen) extensions at room temperature is the partial suppression of recovery and the consequently diminished inhibiting effect of recovery on strain ageing.

Position C

Tests at 90°K are similar to the corresponding tests on the super-purity aluminium specimen. This is not unexpected as strain ageing does not occur at this temperature due to the absence of solute atom diffusion. Test 1 shows also that no recovery softening is taking place while Tests 2, 3

and 4, all of which involve unloading, exhibit large unloading yield points. The increase in size of these unloading yield points compared with tests at position C, for the super-purity aluminium crystal is due entirely to the larger applied loads and extensions operative during the alloy tests, as shown in the table.

Fig. 12

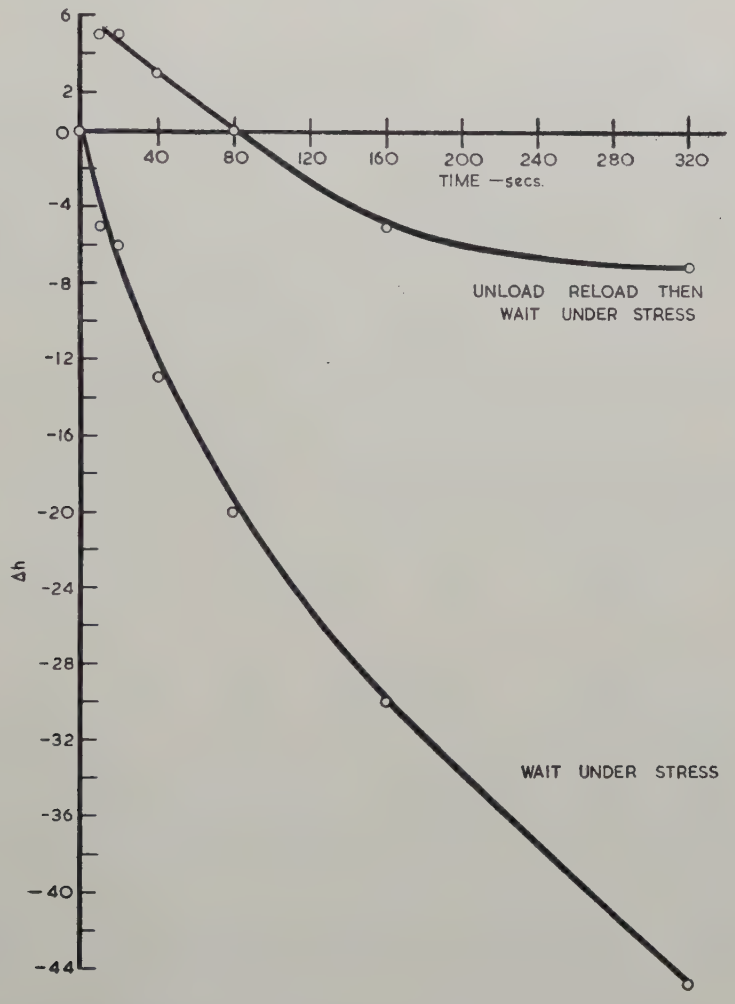

The variation of changes in flow stress (Δh) as a function of waiting time for alloy crystal T143 after 15% elongation at 295°K.

§ 7. Summary of Results

Test 1. *Test stopped and restarted after a time interval of* 5 *min during which time no load was deliberately removed*

295°K. The alloy crystal exhibited a strain ageing yield point while the aluminium crystal did not. At large extensions, a fall in flow stress

Table 1. Details of loads and elongations at which interruptions of tensile Tests occurred and the Percentage Load Removed where Applicable

Test (see fig. 9)		Super-purity aluminium (specimen T286) Load (kg)	Elong. (%)	Unload (%)	Load range (kg)	Elong. range (%)	Test (see fig. 9)		0·42 at. % zinc alloy (specimen T316) Load (kg)	Elong. (%)	Unload (%)	Load range (kg)	Elong. range (%)
A	1	0·688	0·302	—	0·186	0·361	A	1	2·068	0·81	—	0·220	0·68
	2	0·754	0·422	84·5				2	2·148	1·01	89·0		
	3	0·818	0·542	78·0				3	2·234	1·28	85·5		
	4	0·874	0·663	73·0				4	2·288	1·49	83·5		
B	1	3·364	15·65	—	0·040	0·75	B	1	4·440	15·6	—	0·068	0·8
	2	3·380	15·90	89·6				2	4·464	15·9	89·2		
	3	3·394	16·15	89·3				3	4·488	16·2	88·8		
	4	3·404	16·40	89·0				4	4·508	16·4	88·4		
C	1	5·72	17·4	—	0·58	1·1	C	1	7·80	19·0	—	1·30	2·6
	2	5·93	17·8	88·6				2	9·10	21·6	89·2		
	3	6·13	18·1	85·5				3	8·60	20·6	88·9		
	4	6·30	18·5	88·5				4	8·90	21·2	89·5		

occurred in both crystals and was accompanied, in the case of the alloy crystal, by a strain ageing yield point of diminished size. Both effects are attributed to recovery.

90°K. No yield points were observed in either specimen and no fall in flow stress occurred. This is explained by the absence of strain ageing and recovery at this temperature.

Test 2. Test stopped for the purpose of removing a large percentage of the applied load which was re-applied immediately to continue the test

295°K. No large effect was observed in either crystal at small extensions indicating that the strain ageing yield point was prevented from occurring in the alloy crystal. At large extensions, unloading yield points in both crystals occurred accompanied by an absence of recovery softening which is attributed to a suppression of recovery by unloading.

90°K. Large unloading yield points occurred in both crystals.

Test 3. Test stopped for an interval of 5 min, specimen then unloaded and reloaded immediately to continue the test

295°K. At small extensions, no yield points were observed in either specimen indicating that the effects of strain ageing in the case of the alloy crystal were eliminated as a result of subsequent unloading. At large extensions unloading yield points and increases in flow stress occurred, but to a smaller extent than in Test 2.

90°K. Large unloading yield points occurred in both crystals.

Test 4. Test stopped, specimen unloaded and immediately reloaded nearly to the onset of plastic flow, left for 5 min before the test was continued

295°K. At small extensions no yield points and no change in flow stress were observed for the aluminium crystal while at large extensions an unloading yield point and an increase in flow stress occurred. Both these effects were slightly larger than those obtained in Test 3, but not as large as in Test 2. Well developed yield points occurred for both extremes of extension for the alloy crystal accompanied by an increase in flow stress. It is suggested that the ageing of sessile dislocations is mainly responsible for this effect, whilst a contributory factor is the inhibiting effect of unloading on recovery which would otherwise reduce the strain ageing yield point at the large extension (as in Test 1).

90°K. Large unloading yield points occurred in both crystals.

§ 8. Discussion

The factors governing the appearance of unloading effects implies that their explanation is closely associated with the mechanism of work hardening. According to the latest ideas on work hardening (Basinski 1959)

Lomer–Cottrell sessiles are not now considered to play such an important role than hitherto supposed. At the same time they must contribute to the general picture of work hardening and their existence can satisfactorily explain the experimental features of unloading. The increased yield point obtained if ageing is preceded by unloading and reloading has been explained in part by the ageing of sessile dislocations. This implies that the dislocations held back by sessiles are released by the break down of the latter in a way discussed by Stroh (1956), rather than by cross slipping around the obstacles. Otherwise ageing the sessiles would not be expected to enhance the yield point.

§ 9. Conclusions

Unloading yield points occur in both aluminium and dilute aluminium–zinc single crystals. Strain ageing yield points are suppressed or enhanced depending whether ageing occurs before or after unloading and reloading. The results suggest that the ageing of sessile dislocations formed by unloading is largely responsible for the enhanced yield point. In addition, room temperature recovery, which produces a fall in flow stress, and a reduced strain ageing yield point can be partially suppressed by unloading, and this effect contibutes to the enhanced yield point if ageing is preceded by unloading and reloading.

Acknowledgments

The author wishes to acknowledge the assistance of Mr. E. H. Köster in the experimental work, and to Dr. A. R. Harding and Mr. G. E. G. Tucker for helpful discussions of the results and their interpretation. Thanks are due to Aluminium Laboratories Limited, Banbury for permission to publish this paper.

References

Basinski, Z. S., 1959, *Phil. Mag.*, **4**, 393.
Bolling, G. F., 1959, *Phil. Mag.*, **4**, 537.
Cottrell, A. H., 1953, *Dislocations and Plastic Flow in Crystals* (Oxford: University Press).
Haasen, P., and Kelly, A., 1957, *Acta Met.*, **5**, 192.
Holden, A. N., and Kunz, F. W., 1952, *J. appl. Phys.*, **23**, 799.
Makin, M. J., 1958, *Phil. Mag.*, **3**, 287.
Paxton, H. W., 1953, *J. appl. Phys.*, **24**, 104.
Stroh, A. N., 1956, *Phil. Mag.*, **1**, 489.

Anomalous Electron Absorption Effects in Metal Foils†

By H. Hashimoto‡
Metallurgy Department, Cambridge University

and A. Howie and M. J. Whelan
Cavendish Laboratory, Cambridge

[Received March 22, 1960]

Abstract

The dynamical theory of electron diffraction including a term to take account of absorption has been applied to explain some contrast anomalies observed at extinction contours and stacking faults on transmission electron micrographs of metal foils. The theory is at present phenomenological because the detailed mechanism of the absorption process is not understood. This paper reports some preliminary results of the theory and compares them with observations.

Observations by transmission electron microscopy on thin foils of several metals have revealed certain interesting contrast effects at extinction contours and stacking faults. These effects can be explained in terms of an anomalous absorption effect similar to the well-known Borrmann effect (1941, 1950) observed with x-rays.

Figure 1 (*a*) and (*b*) and fig. 2§ show typical examples of the appearance of bend extinction contours (Heidenreich 1949) observed on transmission electron micrographs of thin and thicker areas of metal foils. Figure 1 (*a*) is a bend contour in a thin region of aluminium foil. Selected area electron diffraction patterns have shown that such a contour is produced by two lowest order Bragg reflections $h\,k\,l$ and $\bar{h}\,\bar{k}\,\bar{l}$. For example the area of the foil labelled A in fig. 1 (*a*) gives rise to a strong 111 reflection together with a weak $\bar{1}\bar{1}\bar{1}$ reflection, while the area labelled B gives rise to a strong $\bar{1}\bar{1}\bar{1}$ reflection and a weak 111 reflection. Subsidiary maxima are visible on either side of the principal dark contours A and B. In the region lying between the two principal contours the intensity transmitted in the bright field image (fig. 1 (*a*)) is observed to be lower than that on the other sides of the principal contours. This asymmetry in the intensity transmitted on either side of a Bragg reflection increases with increasing foil thickness while the visibility of subsidiary maxima decreases. In thicker regions a bend extinction contour appears as a dark band. An example of this is shown in fig. 2, which is a bright field micrograph taken from a copper foil.

---

† Communicated by the Authors.
‡ On leave of absence from Kyoto Technical University, Japan.
§ Figures 1 and 2 and figs. 7 and 8 are shown as plates.

In this case no subsidiary maxima are visible. The interior of the band is very dark, while the light borders of the band show very good electron transmission. Note that the dislocations are very clearly visible in these regions. The bands can be swept across the field of view by tilting the specimen. Selected area diffraction patterns have confirmed that the transparent borders are associated with particularly strong incident and lowest order reflected waves in agreement with the observations of Kohra and Watanabe (1959) on molybdenite crystals. The intensity asymmetry in thin regions and the disappearance of subsidiary contours in thick regions are not predicted by the usual dynamical theory of diffraction (without absorption).

The presence of considerable background scattering and Kikuchi lines on selected area diffraction patterns suggest that incoherent scattering of electrons may be responsible for the contrast anomalies discussed above. A phenomenological description of the effect of incoherent scattering (hereafter referred to as absorption) can be obtained by application of the dynamical equations of electron diffraction to a crystal with complex lattice potential. The imaginary part of the lattice potential gives rise to absorption. Yoshioka (1957) has given a general quantum mechanical justification of this procedure. In considering the explanation of the observations it is important to note that both types of bend contour mentioned above are produced by two lowest order Bragg reflections, i.e. the so-called 'systematic' reflections on opposite sides of the origin of reciprocal space. The dynamical theory of electron diffraction for two strong reflections (i.e. a three-beam theory) should therefore be applied. However, numerical calculations for this case have shown that the main qualitative features of the results are unchanged by applying the usual two-beam theory to one-half of the bend contour. The theory is then identical with that of the corresponding x-ray Borrmann effect which has been treated by Zachariasen (1945), by Von Laue (1949) and by Hirsch (1952). Figure 3 (*a*) and (*b*) shows typical intensity profiles of one-half of a bend extinction contour for bright and dark field images respectively, calculated by the one strong reflection approximation (i.e. a two-beam theory). It will be noted that the intensity of the bright field image is asymmetrical about the centre of the reflection, while the peak of maximum intensity is displaced from the centre. However, in the dark field image there is no asymmetry and the peak maximum occurs at the centre of the reflection. This has been observed experimentally. Figure 1 (*b*) is the dark field image in the strong reflection from the area A in fig. 1 (*a*). To a rough approximation the image appears symmetrical. The exact symmetry of course will depend on the nature of the buckling of the foil. The vertical scale of the intensity in fig. 3 depends on the mean absorption coefficient of the material, while the shape of the curves depends on the crystal thickness t, and on two parameters t_0 and τ_0. t_0 is the extinction distance calculated from $t_0 = \lambda E / V_g$, where λ is the electron wavelength, E is the electron energy in volts, V_g is the Fourier coefficient of order **g** of the real part of the complex lattice potential

and **g** is the reciprocal lattice vector corresponding to the Bragg reflection. Extinction distances for low-order reflections of face-centred cubic metals are of the order of a few hundred angstroms (Whelan 1959, Hirsch *et al.* 1960). τ_0 is an absorption parameter derived from the same formula by substituting for V_g the Fourier coefficient of order **g** of the imaginary part of the complex lattice potential. The spacing between the subsidiary

Fig. 3

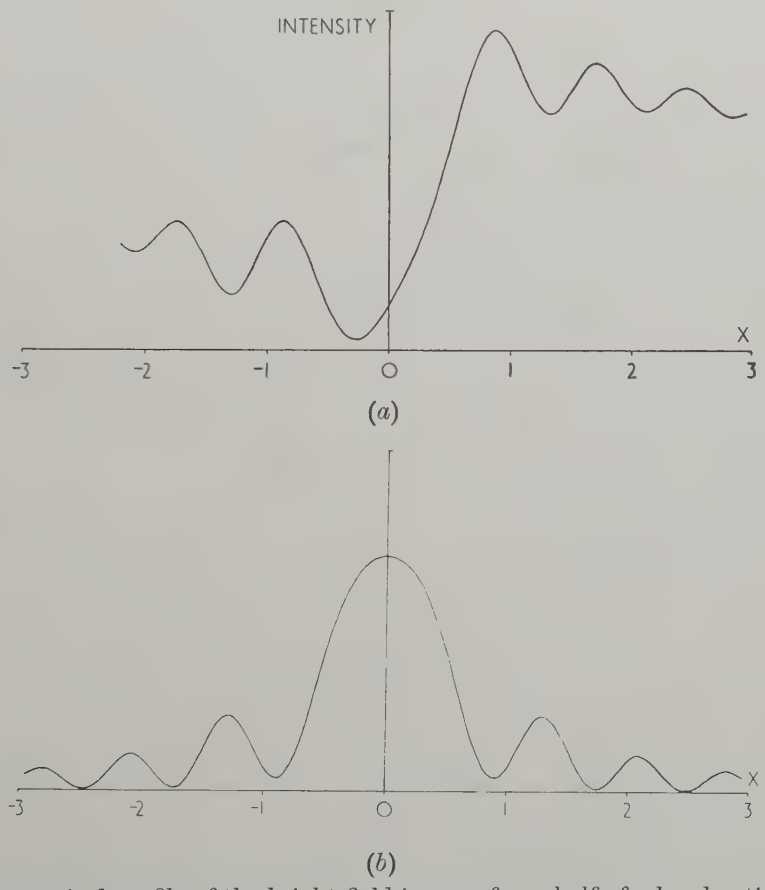

(*a*) Theoretical profile of the bright field image of one-half of a bend extinction contour in a thin region such as fig. 1 (*a*). The ordinate is the intensity transmitted on a linear scale which depends on the mean absorption coefficient. The abscissa x (see Whelan and Hirsch 1957 a) represents deviation from the Bragg angle. $x=0$ corresponds to the exact Bragg angle. Note the asymmetry of the bright field image. (*b*) Profile of the dark field image corresponding to (*a*). ($t/t_0=1{\cdot}5$, $t/\tau_0=0{\cdot}15$.)

maxima in fig. 3 (*a*) is determined by t/t_0, while the shape of the curve, i.e. the degree of asymmetry and the amplitude of the subsidiary oscillations, depends on t/τ_0. The quantity $\pi t/\tau_0$ is identical with the parameter Ak used by Zachariasen (1945) and by Hirsch (1952). Figure 3 (*a*) and (*b*) corresponds to $t/t_0=1{\cdot}5$ and $t/\tau_0=0{\cdot}15$. As t/τ_0 increases the asymmetry of

the bright field image increases while the amplitude of the subsidiary oscillations decreases. Figure 4 (*a*) and (*b*) shows intensity profiles for $t/t_0 = 10$ and $t/\tau_0 = 1{\cdot}0$. Figure 4 (*a*) accounts qualitatively for the nature of one-half of the bend extinction contour observed in thick regions

Fig. 4

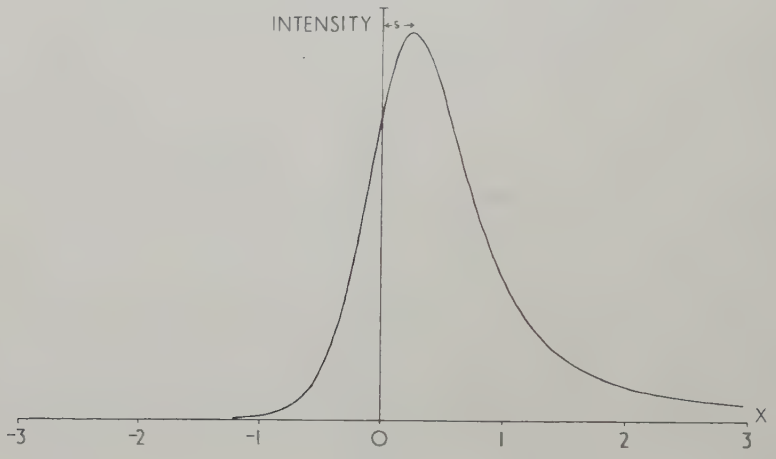

(*a*)

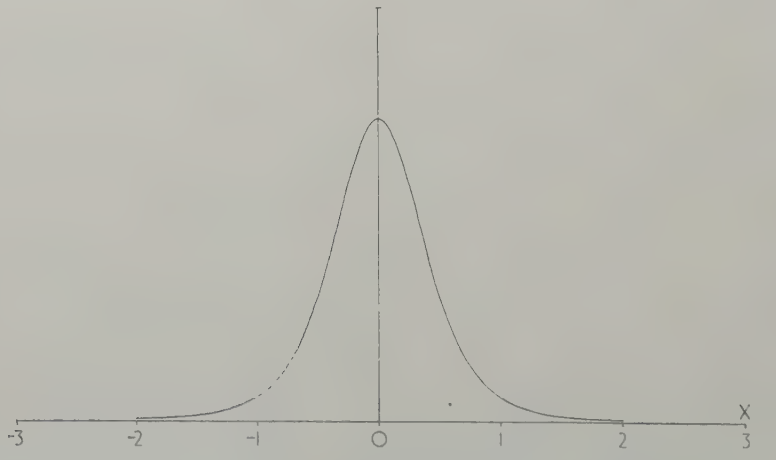

(*b*)

(*a*) Theoretical profile of the bright field image of one-half of a bend extinction contour in a thick region such as fig. 2. Note the absence of subsidiary maxima and the displacement s of the peak from the exact Bragg angle. (*b*) Profile of the dark field image corresponding to (*a*). ($t/t_0 = 10$, $t/\tau_0 = 1$.)

(fig. 2). Note that for thick crystals (fig. 4 (*a*) and (*b*)) the intensity profile of the dark field image is similar in nature to that of the bright field image except for a displacement s of the peak of the bright field image from

the exact Bragg condition. This is the phenomenon of 'reversal' of the extinction line and has been discussed by Hirsch (1952) for the x-ray case. This effect in thick regions has also been verified experimentally.

The theory has been extended to calculate the profile of fringes observed at stacking faults in face-centred cubic metals. The formal theory can easily be obtained from that given by Whelan and Hirsch (1957 a, b) by allowing the parameters β_1 and β_2 used by those authors to become complex and by including a mean absorption coefficient. The theory leads to the following results.

(*a*) At the reflecting position for small t/τ_0, the fringe profiles exhibit alternating intensities of fringe maxima or minima depending on crystal thickness. The spacing between the intensity maxima corresponds approximately to $\frac{1}{2}t_0$ as in the theory without absorption. The difference between adjacent intensity minima is larger near the edges of the fault (fig. 5 (*a*)), while the peak intensity transmitted in the middle of the fault is smaller than that at the edges. In fact in fig. 5 (*a*) the choice of absorption parameters ($t/t_0 = 5, t/\tau_0 = 0{\cdot}35$) is such that the subsidiary minima are suppressed at the light fringes A near the edges of the fault although they are visible at B. The intensity profile of the bright field image is symmetrical about the centre of the fault.

(*b*) Figure 5 (*a*) shows that the theory accounts for the absence of subsidiary fringes near the edges of the fault, an effect which was tentatively attributed by Whelan and Hirsch (1957 b) to strains due to a surface oxide film. Figure 7 shows an example of a stacking fault in stainless steel where the subsidiary fringes near the edges of the fault are not visible. It is thought that this micrograph corresponds fairly closely to the condition of fig. 5 (*a*).

(*c*) The profile of the dark field image is asymmetrical about the centre of the fault (fig. 5 (*b*)). This has been verified experimentally.

(*d*) At the reflecting position for large t the subsidiary maxima or minima tend to disappear except near the centre of the fault. In this case the spacing between the main fringes near the edges of the fault corresponds to t_0. The mean intensity transmitted in the dark and bright field images and the visibility of the fringes is lower near the centre of the fault as shown in fig. 6 (*a*) and (*b*), for which $t/t_0 = 8, t/\tau_0 = 0{\cdot}56$. Figure 8 shows an example of the decrease in visibility of the fringes near the centre of a fault in stainless steel. It is thought that this micrograph corresponds closely to the theoretical curve of fig. 6 (*a*).

The results show that absorption effects must be considered to explain the fine detail of transmission electron micrographs of thick metal foils. At present however there is no theoretical treatment of incoherent scattering in metals which leads to a reliable estimate of the absorption parameter τ_0. The observations on aluminium and stainless steel foils can be explained on the assumption that τ_0 is about 10 to 15 times t_0. The detailed mechanism of the absorption process is also unknown.

Fig. 5

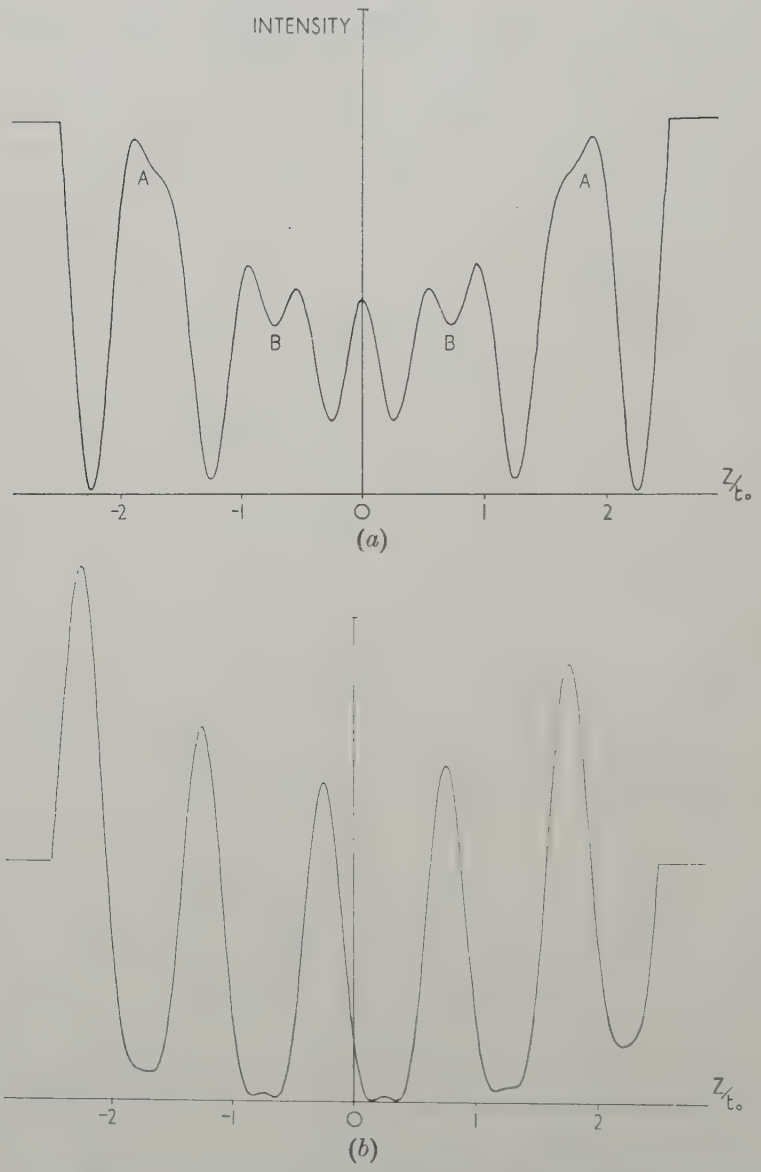

(*a*) Theoretical profile of the bright field image of the interference fringes at a stacking fault in a face-centred cubic metal. The ordinate is the intensity transmitted on a linear scale which depends on the mean absorption coefficient. The abscissa z/t_0 is proportional to distance on the image measured from the centre of the fault ($z=0$) (see Whelan and Hirsch 1957 a). The curve is calculated from the exact Bragg angle ($x=0$). Note the weak dark fringes at B and the absence of similar fringes at A. Note also that the image is symmetrical about $z=0$. Compare with fig. 7. (*b*) Dark field image corresponding to (*a*). Note the asymmetry of the image about $z=0$. ($t/t_0=5$, $t/\tau_0=0{\cdot}35$.)

It is in principle possible to estimate τ_0 from bright field and dark field micrographs. For example in thick regions the displacement s (fig. 4 (*b*)) between the peaks of dark field and bright field images is a function of t/τ_0, and provided t is known, τ_0 can be estimated if s is measured. Measurements of the intensity transmitted at extinction contours relative to that of the incident beam could also be used to determine the mean absorption coefficient. Then if τ_0 were known for several reflections, the atomic form factor for incoherent scattering could be derived.

Fig. 6

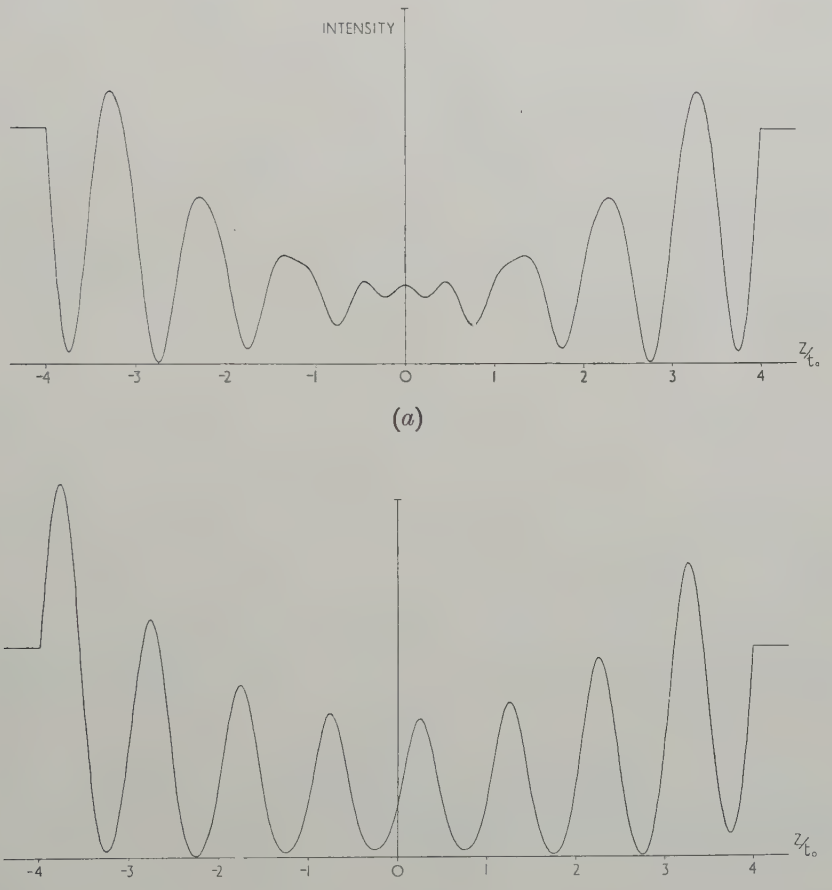

(*a*) Theoretical profile at the exact Bragg angle of the bright field image of the fringes at a stacking fault in a thicker region. Note the absence of subsidiary dark fringes except near the centre of the fault. Note also the decrease in visibility of the fringes near the centre of the fault. Compare with fig. 8. (*b*) Dark field image corresponding to (*a*). ($t/t_0=8$, $t/\tau_0=0{\cdot}56$.)

An interesting application of the results for a stacking fault arises from the symmetry and asymmetry about the centre of the fault of bright field and dark field images respectively. For certain symmetrical orientations of a f.c.c. plate crystal (e.g. (100) parallel to the surface) it is not possible from the bright field image of a stacking fault alone to decide which edge of the fault corresponds to the top or bottom surface of the crystal. However, comparison of fig. 5 (*a*) and (*b*) (or fig. 6 (*a*) and (*b*)) shows that at one edge of the fault bright field and dark field images tend to be similar in nature, whereas at the other edge they tend to be complementary. These two cases correspond to the intersection of the fault with the surfaces closest to and furthest away from the electron beam source respectively. Therefore bright field and dark field images of a fault should be sufficient to differentiate between the two edges. Similar considerations would be expected to hold for dotted (fringed) dislocation images.

The theory also accounts qualitatively for certain other contrast effects observed at dislocations, such as the dotted appearance near the surfaces of dislocations running obliquely through foils (Hirsch *et al.* 1960) and the general dark nature (free from dotted effects) of the images of dislocations in the interior of thick crystals. These effects would be analogous to the decreasing transmitted intensity and visibility of fringes at a stacking fault towards the centre of the fault. Full details of the theory outlined in this paper will be published later.

Acknowledgments

Our thanks are due to Professor N. F. Mott, F.R.S. and to Professor A. H. Cottrell, F.R.S. for their encouragement. We are grateful to Drs. P. B. Hirsch, J. Nutting, to Mr. R. M. Fisher, and to a number of our colleagues for stimulating discussions. Thanks are also due to the Director and staff of the Mathematical Laboratory, Cambridge, for permision to use EDSAC 2.

Acknowledgments for financial support are due to the Japanese Ministry of Education (H.H.), to the Master and Fellows of Trinity College, Cambridge (A.H.) and to the Royal Society Mr. and Mrs. John Jaffé Donation (M.J.W.).

References

Borrmann, G., 1941, *Phys. Z.*, **42,** 157; 1950, *Z. Phys.*, **127,** 297.
Heidenreich, R. D., 1949, *J. appl. Phys.*, **20,** 993.
Hirsch, P. B., 1952, *Acta cryst.*, **5,** 176.
Hirsch, P. B., Howie, A., and Whelan, M. J., 1960, *Phil. Trans. roy. Soc.* **252,** 499.
Kohra, K., and Watanabe, H., 1959, *J. phys. Soc. Japan*, **14,** 1119.
Laue, M. von, 1949, *Acta cryst.*, **2,** 106.
Whelan, M. J., 1959, *J. Inst. Metals*, **87,** 392.
Whelan, M. J., and Hirsch, P. B., 1957 a, *Phil. Mag.*, **2,** 1121; 1957 b, *Ibid.*, **2,** 1303.
Yoshioka, H., 1957, *J. phys. Soc. Japan*, **12,** 628.
Zachariasen, W. H., 1945, *Theory of X-ray Diffraction in Crystals* (New York: Wiley & Sons), p. 135.

REVIEWS OF BOOKS

Heat and Thermodynamics. Fifth edition. By J. K. Roberts, revised by A. R. Miller. (Blackie, 1960.) [Pp. 619.] Price £2 5*s*.

The fifth edition of this well-known text-book consists essentially of the edition of 1950 together with some 25 pages of new material. The changes appear to be, for the most part, those necessitated by advances in technique or by changes in convention. For example, the section on magnetic cooling reports the successful outcome of the attempts at nuclear demagnetization, and the chapter on temperature mentions the new definition of the Thermodynamic Scale in terms of a single fixed point. J. A.

Hypersonic Flow. Edited by A. R. Collar and J. Tinkler. (Butterworths Scientific Publications, 1960.) [Pp. xv+432.] Price £3 10*s*.

This book is a record of the eleventh Colston Symposium, held at the University of Bristol in April 1959, which was devoted to Hypersonic Flow. Fifteen papers were presented, which are all reproduced here in full together with a report of the discussion after each paper. The scope of the papers range from surveys of the experimental work being carried out at various laboratories throughout the world to applied research on the design of hypersonic vehicles and the theoretical solution of particular flow problems. The book will be of great intesest to active workers in the field of hypersonic flow, but cannot be recommended to the reader who knows little about the subject and wishes to learn more.

The publishers are to be congratulated on the very attractive appearance of the book. P. G. S.

Non-Relativistic Quantum Mechanics. By R. M. Sillitto. (Edinburgh University Press, 1960.) [Pp. 230.] Price £1 15*s*.

Although there are numerous treatises on Quantum Theory, there is room for a modern teaching text for undergraduates. Here is a nice straightforward account of the standard theory, without frills but quite clear and explicit. Whilst the argument is mathematical rather than ' physical ' nothing is laboured and there are no obvious omissions. It is going to be extremely useful, especially for good students who are not specializing in mathematical physics but who need to learn the key ideas from a modern standpoint. I only wonder whether the author will succeed in his attempt to put across pure matrix mechanics at an early stage before the reader has had much experience with the general properties of wave functions. The conceptual jump from energy levels and wave packets to states and operators is the most important and difficult thing to learn in the course and is, perhaps, best approached more gently. But the direct attack is certainly worth trying. J. M. Z.

Progress in Elementary Particle and Cosmic Ray Physics. Vol. V. Edited by J. G. Wilson and S. A. Wonthuysen. (Amsterdam : North-Holland Publishing Company, 1960.) [Pp. 461.] Price £4 5*s*.

The earlier volumes in this series were entitled *Progress in Cosmic Ray Physics.* With the great accelerators encroaching more and more on the high energy region, the editors felt that the title and the contents of the series should include elementary particle physics. Clearly this is a wise change.

The present volume consists of review articles on weak decays, nucleon–nucleon scattering, anti-nucleons, cosmic ray jets, the absorption of negative muons. Of these perhaps the most stimulating is the article on jets by D. H. Perkins, in which the puzzle of the high degree of elasticity in very high-energy collisions is emphasized. J. H.

Theory of Elementary Particles. By P. Roman. (Amsterdam : North-Holland Publishing Company, 1960.) [Pp. xii+575.] Price £5.

The main part of this volume consists of a very careful and very detailed discussion of those groups which are used for classifying the elementary particles and for examining the selection rules that govern their interactions. The representations of the four-dimensional orthogonal group and its sub-groups are considered in detail, and applied to spin and rotation, the Lorentz invariance of generalized field equations, and the various theories of isobaric space. The discrete operations, space inversion, time reversal and charge conjugation are also examined and there is a clear discussion of parity violation.

The mathematical apparatus which is set up is perhaps somewhat more elaborate than is necessary for the job it does, and in places the notation is too generalized and too cumbersome. Nevertheless this must be a valuable book for anyone who wishes to know what are the mathematical foundations of the symmetry principles of elementary particle physics. J. H.

Electrons and Phonons. By J. M. Ziman. (Oxford : The Clarendon Press, 1960.) [Pp. 554.] Price £4 4*s*.

This book is excellent. The author sets out to describe the bulk of the electron and phonon theory of solids with emphasis on transport phenomena. While presupposing only an elementary knowledge of wave mechanics, he succeeds beyond all expectations and, indeed, it is impossible to think of a single criticism which can be made of content or of presentation. The author's style is so lively that the reader's attention is always captured even throughout the more sophisticated sections of the book and important principles are clearly distinguished from subsidiary points in a way usually possible only in lectures.

The subject matter is logically organized and the index so good that it is easy to find the discussion of any particular problem. As a result the book will be just as valuable to the established research worker as it is to the graduate student. It is quite obviously one of those few books which we always want close to hand and despite its high cost must be regarded as indispensable to any worker or student in this field W. M.

Introduction to Statistical Thermodynamics. By T. L. Hill. (Reading, Mass. : Addison-Wesley Publishing Company, 1960.) [Pp. xiv+508.] Price £3 14*s*.

This volume is intended—as its title implies—as an introductory text-book on equilibrium statistical mechanics, and as such is aimed at the same public as Rushbrooke's text-book. It is mainly meant to be used for courses for chemists—in Great Britian it would serve admirably for a final Honours Year course. The coverage of topics is very broad and gives a good idea of modern—that is, post-war—developments in statistical thermodynamics. After a short introduction on the principles of statistical mechanics (although this is called ' quantum ' statistical mechanics, quantum mechanics only is invoked in assuming quantization of energy ; the typical quantum mechanical aspects of the Fermi–Dirac and Bose–Einstein's statistics are only very briefly discussed

in the very last chapter) the main part of the book is concerned with applications. These range from perfect monatomic, diatomic, and polyatomic gases to the theory of polymer and polyelectrolytic solutions and gels. A large number of exercises of a broad range of difficulty make this book even more useful, and this reviewer expects that it will be widely used by physical chemists.

D. ter Haar.

Optics of Thin Films. By Antonin Vašiček. (North-Holland Publishing Company, 1960.) [Pp. xii+403.] Price £4.

The applied optics of thin films has become an important subject in the past twenty years but there is still no good general text on it. Professor Vašiček's book is an interesting essay which recalls its author's striking personality but it is too uneven and sketchy to be useful as a text-book. It deals with Fresnel's formulae, reflection and transmission by one, two and many films, metallic films and polarization effects. The treatment is almost entirely theoretical ; there is nothing about methods of producing thin films, a very little about measuring their properties and some mention of applications.

The author points out in the preface that the book reflects his own interests and this is certainly clear from the lists of references alone. This bias results in unnecessary detail on some topics, e.g. it is hardly necessary nowadays to devote about 100 pages to deriving and discussing special formulae for one and two films when these follow immediately from the general formulae for n films. On the other hand, many important properties of periodic multilayers are omitted ; if the author had applied the Brillouin zone theory here he would not have made the following misleading statement (p. 238) : " Although the greatest reflectivity increases further with increasing number of films, the spectral region of this high reflectivity narrows somewhat ". It does not. Results are frequently obtained for multilayers and also for single absorbing films by considering multiple reflections and there is much discussion about the validity of this and other methods. It seems to the reviewer that provided the elementary but tedious mathematics is correctly carried out, all such phenomenological approaches must lead to the same results since they are all based ultimately on Maxwell's equations.

To sum up, those familiar with the subject of thin film optics will enjoy reading this book but it cannot rank either as a reference work, since it covers too little ground, or as a research monograph, since it is too laboured on elementary points.

W. T. W.

Foundations of Electromagnetic Theory. By John R. Reitz and Frederick J. Milford. (Addison-Wesley, 1960.) [Pp. 387.] Price £2 9*s*.

Principles of Electricity and Magnetism. By E. M. Pugh and E. W. Pugh. (Addison-Wesley, 1960.) Price £2 9*s*.

Foundations of Electromagnetic Theory is a text written for a course on electricity and magnetism for physicists, advertised as " at advanced undergraduate level ", though it does not quite cover all that might be expected in Cambridge of a final year student. It starts with electrostatics at a level including the use of Poisson's equation and the uniqueness theorem, and covers the usual range through Maxwell's equations up to the radiation from a dipole aerial and from an accelerating point charge. Two chapters on the microscopic theory of dielectrics and magnetism are included, as well as an interesting chapter on the behaviour of plasmas. However, there are also a few gaps, with no mention for example of noise, valves, the impulse response of a two-terminal system, or the formulation of magnetostatic energy in the presence of permanent magnets. The Drude formula for the conductivity of a metal contains the usual incorrect factor of $\frac{1}{2}$.

On the whole the style is extremely clear, and the book can be warmly recommended as a good text for third year students. There are also many examples, the typography is pleasing, and the diagrams are up to the usual superlative Addison-Wesley standard. It seems hardly necessary to remark these days that rationalized M.K.S. units are used.

The second book *Principles of Electricity and Magnetism* covers almost exactly the same ground but at a somewhat lower standard, particularly in the use of mathematics. The style is rather ponderous. V. H. O.

Selected Lectures in Modern Physics. Edited by H. Messel. (Macmillan, 1960.) Price 30*s*.

In January 1958 the Nuclear Research Foundation arranged a series of lectures on selected topics in physics, in the University of Sydney. The objective was a refresher course for science teachers which would stimulate interest and, eventually, encourage students to read Science or Engineering at Universities. This book is a reprint of the lectures, and it is interesting to note that a copy was issued, free, to every science teacher in the State of New South Wales.

There are 22 lectures in the book, given by 18 people and, as might be expected, the emphasis is strongly placed upon nuclear physics. The first nine lectures deal with various aspects of this subject—if we include cosmic radiation under the same general heading. There are three lectures related to astrophysics, two on relativity, and the remainder on a variety of topics. In an effort of this kind, the choice of subject matter is to some extent dictated by the interests of the lecturers available, and to some extent also by the possibility of adding a little glamour to an elementary exposition. The former factor doubtless accounts for the inclusion of a most interesting chapter on " Physics in Rainmaking " and the latter for the fact that there is no mention of solid state physics apart from one lecture on " Transistor Electronics ". In the same way, it is understandable that many of the passing references to particular pieces of research are to Australian work.

The style and standard of the individual lectures varies considerably. There is the frankly chatty and conversational style of " How to talk to an Electronic Brain " and the rather thorough and formal exposition of " Precise Measurement ". This last, although a fascinating subject is a little unexpected, in a book on " Modern Physics ", as indeed is the lecture on " The Concept of Temperature ". Some of the lectures are well written and easy to read, others are more difficult, either because of the inherent difficulty of the subject—e.g. " Strange Particles" —or because of defects of presentation. The second lecture on Nuclear Energy, dealing with reactor technology is little more than a set of lecture notes and contains the correct, but unhelpful, paragraph : " Example of gases H_2, He, CO_2, N_2, Air, A."

It would perhaps be unfair to criticize the book for a lack of balance either in subject matter or in treatment. It could form a useful addition to sixth form and University libraries, where harassed students writing essays would welcome it, and find the short reading lists appended to many of the lectures very helpful. N. T. O.

Solid State Physics. Vol. 10. Edited by F. Seitz and D. Turnball. (New York : Academic Press, 1960.) [Pp. 516.] Price $14.50.

The mixture as before—Positron Annihilation (Wallace) ; Diffusion in Metals (Lazarus) ; Wave Functions for Electron-Excess Color Centres in Alkali Halide Crystals (Gourary and Adrian) ; Continuum Theory of Stationary Dislocations (de Wit) ; Theoretical Aspects of Superconductivity (the late

Professor M. R. Schatroth). I still think that it is a mistake to ask every well known scholar in the field to write a review of his subject, instead of commissioning longer, broader, more integrated articles and books from carefully selected people. But the series continues to be useful for reference.

J. M. Z.

Introduction to Solids. By L. V. Azaroff. (McGraw-Hill, 1960.) [Pp. 460.] Price £3 14*s*.

An amusing consequence of progress in science is that it keeps making nonsense of the inter-disciplinary frontiers so firmly defended by the academic pundits. This book correctly claims to be " suitable for students of chemistry, ceramics, metallurgy, mineralogy, physics and all engineering fields dealing with solid state ". All that it does is to collect together all the physical properties of solids, and indicate their explanation. It is not a very advanced book ; there is really no mathematics, and some of the more complicated topics are blocked in rather sketchily. But the author's instinct to explain things in terms of 3-dimensional geometry is essentially sound. Solids, like works of architects, are *structures*, and this is more directly relevant, for most scientific purposes, than that they are also minimum free energy states of ensembles of solutions of the quantum-mechanical many-body problem. Here is a lively, well-written, elementary text book for ordinary undergraduates. It is what we have been needing for a long time.

J. M. Z.

Advances in Cryogenic Engineering. Vol. 5. Edited by K. D. Timmerhaus. (New York : Plenum Press Inc., 1960.) [Pp. 582.] Price $13.50.

This volume contains the papers delivered at the Conference on Cryogenic Engineering held at the University of California on September 2–4, 1959.

The primary emphasis at this conference was on the use of cryogenic liquids as fuels for missiles and the majority of the papers dealt with problems arising from this application. There can be no doubt that the book is essential reading for all engineers working in this field. Many of the papers will also be of interest to a wider public, especially the series of articles on thermal insulation and the experimental studies of the burning and explosion of hydrogen.

J. A.

Physics of the Atom. By M. Russell Wehr and James A. Richards. (Reading, Mass.: Addison-Wesley; and London, 1960.) [Pp. xi+420.] Price £2 9*s*.

Modern physics, interpreted as the contribution of the twentieth century to the subject, is gradually working its way further and further back in university and now even in school courses. Some day, perhaps, we shall have a satisfactory treatment which combines the classical approach with the modern, the older knowledge being entirely re-seen in the light of the new. Until that happens, we have an increasing number of tests from which to choose in shaping an introductory course in atomic and nuclear physics to follow the traditional grounding in heat, light, sound, electricity and magnetism. For reasons which it would be interesting to analyse, they mostly come from authors in the United States and very few from the United Kingdom. The latest addition to the ranks is also American, and it is perhaps best to compare it with its stable-mates.

Wehr and Richards have set out to write a sequel to the well-established *University Physics* of Sears-Zemansky. Twelve chapters take the student from the atomic view of matter, electricity and radiation, through relativity,

x-rays and the wave-particle concept to the solid state, with nuclear physics occupying the last four chapters. The treatment is largely chronological and in this respect, as in the informal, almost colloquial style, the book is akin to Oldenberg's *Introduction to Atomic Physics*. It is distinctly more advanced, however, in that it has " not hesitated to use calculus where it is appropriate ". The amount of mathematical development is very limited, nevertheless, except in the chapter on relativity. It is thus much less suited to a university introductory course as usually understood in this country than is French's *Principles of Modern Physics*, for example. It should be much more useful to sixth forms, as a chatty and more or less painless survey for the would-be physicist of the territory he must later explore in greater detail. It should also fit well into a broad course in physical science for chemists, engineers or others who want only a nodding acquaintance with the ideas of modern physics, without a detailed mastery of its techniques. If they work through a good selection of problems at the end of each chapter, they could pick up quite a lot of these also, if they would. The text is very well set-out, the diagrams are excellent, and plenty of references are given for further reading. One can well imagine a youngster's imagination being fired on coming upon such a readable and intelligently presented account of what physics now means, after all the drudgery of the old school mill. But at the same time someone ought to warn him that it is not always so easy as it is made to sound in these pages. V. E. G.

BOOK NOTICES

Formation and Trapping of Free Radicals. Edited by A. M. Bass and H. P. Broida. (New York and London: Academic Press, 1960.) [Pp. 522.] $16.00.

The Other Side of the Moon. Issued by the U.S.S.R. Academy of Sciences. Translated from the Russian by J. B. Sykes. (Pergamon Press, 1960.) [Pp. 36.] 10*s*. 6*d*.

Sector-focused Cyclotrons. Proceedings of an Informal Conference, Sea Island, Georgia, February 2–4, 1959. Nuclear Science Series Report, No. 26. (Washington, D.C.: National Academy of Sciences, 1959.) [Pp. 291.] $2.50.

Cosmology. By H. Bondi. Second Edition. (Cambridge: University Press, 1960.) [Pp. 182.] Price 30*s*.
This is a second edition of a well-known work.

Über neue Rechnungsgrundlagen der Atom- und Strahlungsphysik. By Karl Nowak. (Wien: Verlag Neue Physik, 1959.) [Pp. 78.] Price D.M. 7.50, 2*s*. 6*d*.

Dynamics of Climate. The Proceedings of a Conference on the Application of Numerical Integration Techniques to the Problem of the General Circulation, held October 26–28, 1955. Edited by R. L. Pfeffer. (Pergamon Press, 1960.) [Pp. 137.] Price £1 15*s*.

[*The Editors do not hold themselves responsible for the views expressed by their correspondents.*]

Fig. 2

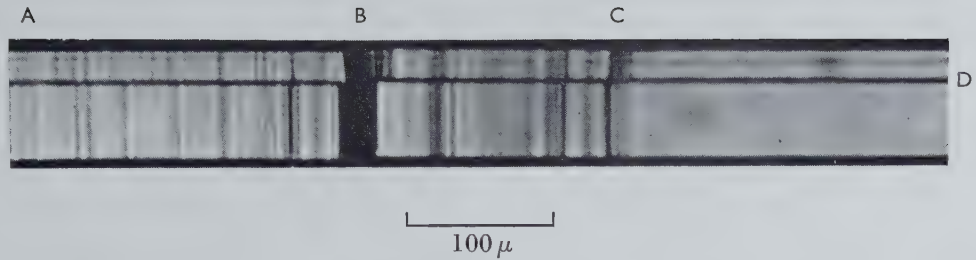

Optical micrograph of a platelet which fractured at B after deformation by pyramidal glide. Note the Lüders band, AC.

Fig. 3

1 μ

Electron micrograph showing pyramidal glide traces, $\langle \bar{1}\bar{1}20 \rangle$ dislocations, $\langle \bar{1}\bar{1}23 \rangle$ dislocations, and prismatic dislocation loops.

Fig. 4

1 μ

Electron micrograph showing ⟨1120⟩ traces at *a*, *b*, *c*, *d*, *e*, pyramidal traces at A, B, C, D, E, F, G, and loops along traces B, C, D, E and G. The dislocation which produced trace E has cross glided at O, acquiring a multiple jog and forming a row of loops.

Fig. 6

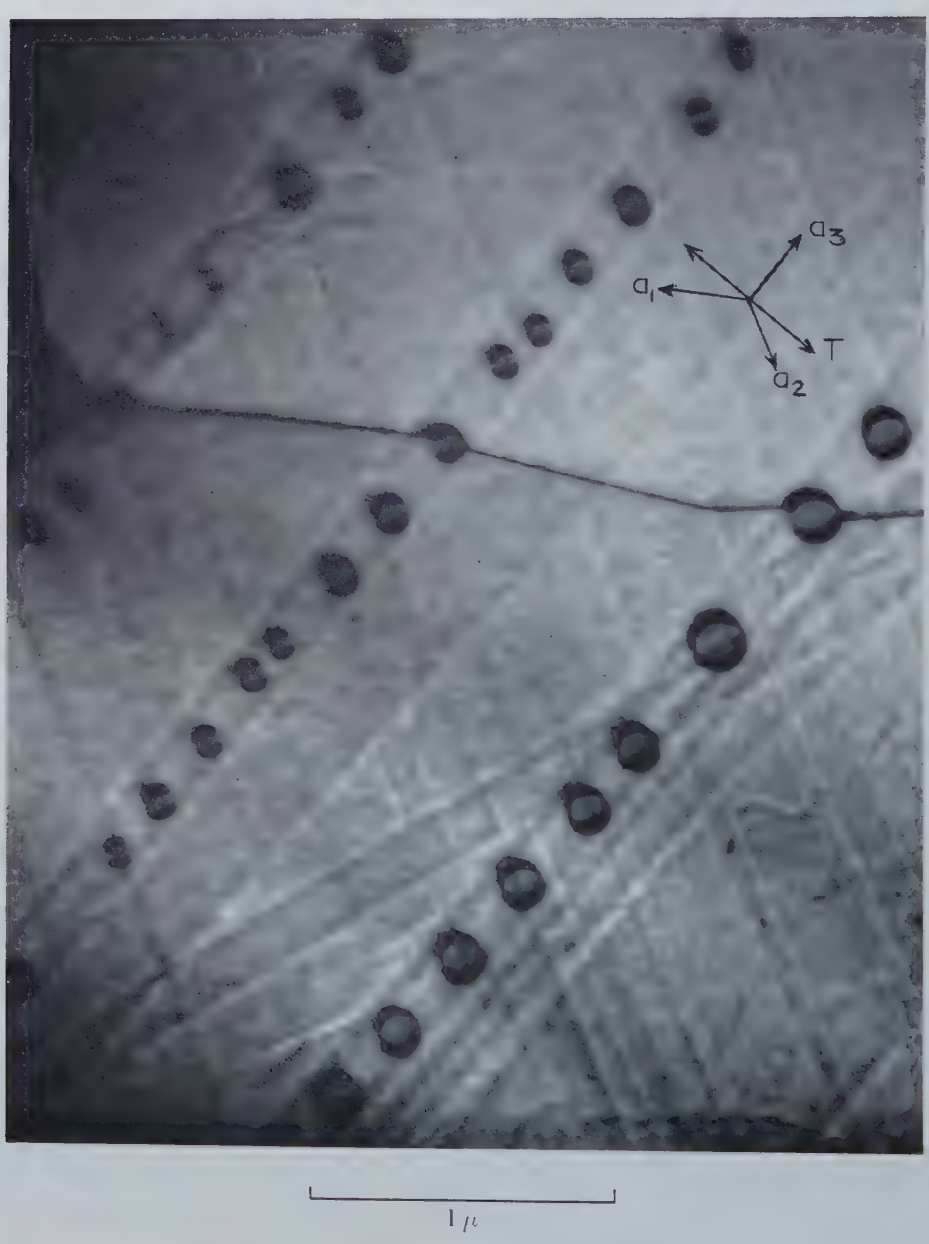

Loops along pyramidal traces. A ⟨1120⟩ dislocation is pinned at three loops.

Fig. 7

1 μ

Heavily deformed region showing $\langle \bar{1}120 \rangle$ dislocations pinned at loops.

Fig. 9

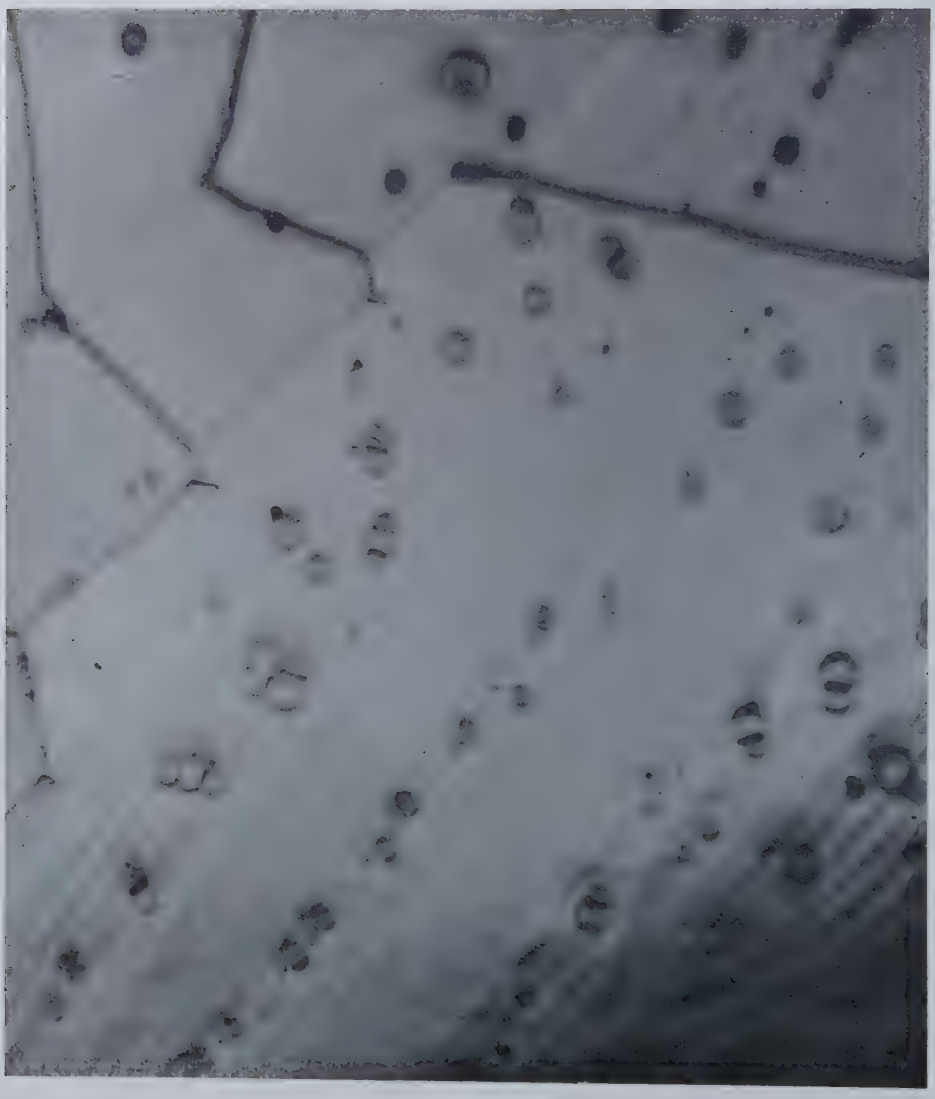

1 μ

Clusters of loops along overlapping glide traces.

Fig. 10

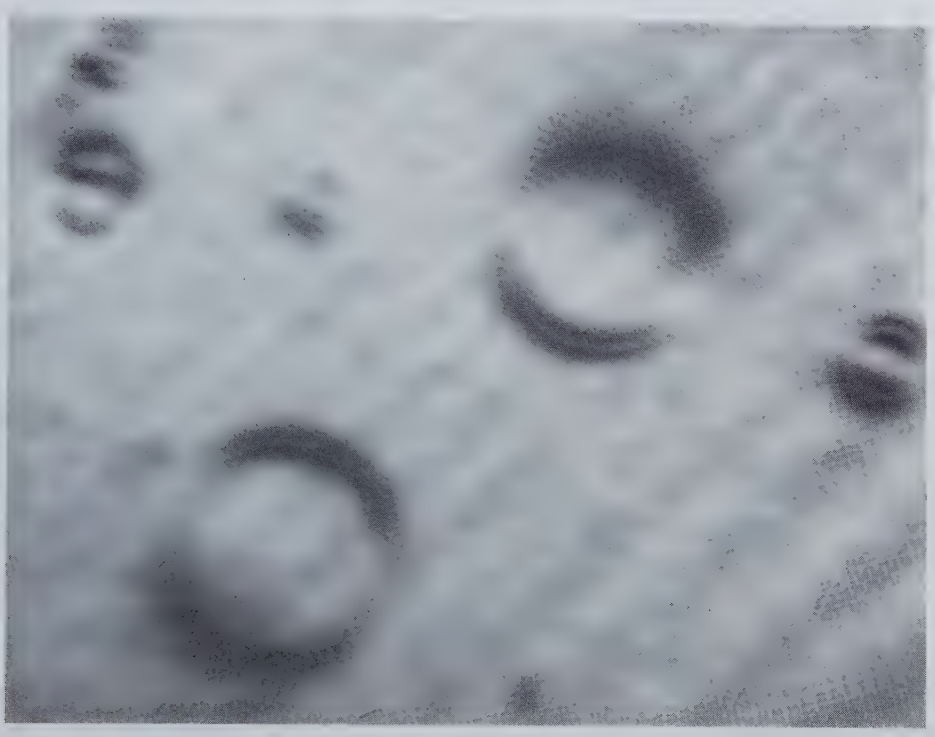

(*a*)

(*b*)

0·1 μ

(*a*) $\langle 0001 \rangle$ loops with vanishing contrast along a direction parallel to strongly reflecting $(11\bar{2}0)$ planes.

(*b*) Diffraction pattern for (*a*), showing the $11\bar{2}0$ spot.

Fig. 10 (*continued*)

(*c*)

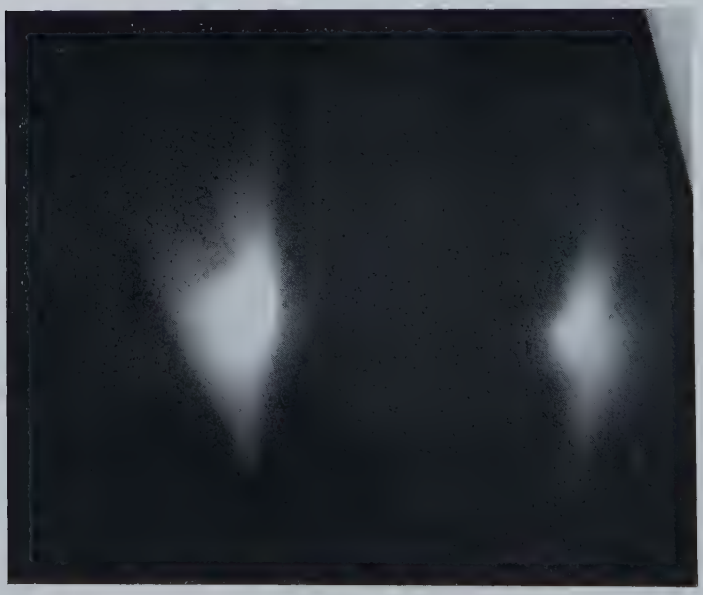

(*d*)

1 μ

(*c*) Both $\langle 0001 \rangle$ loops (at A) and $\langle \bar{1}\bar{1}23 \rangle$ loops formed by the same dislocation mechanism.

(*d*) Diffraction pattern of (*c*).

Fig. 11

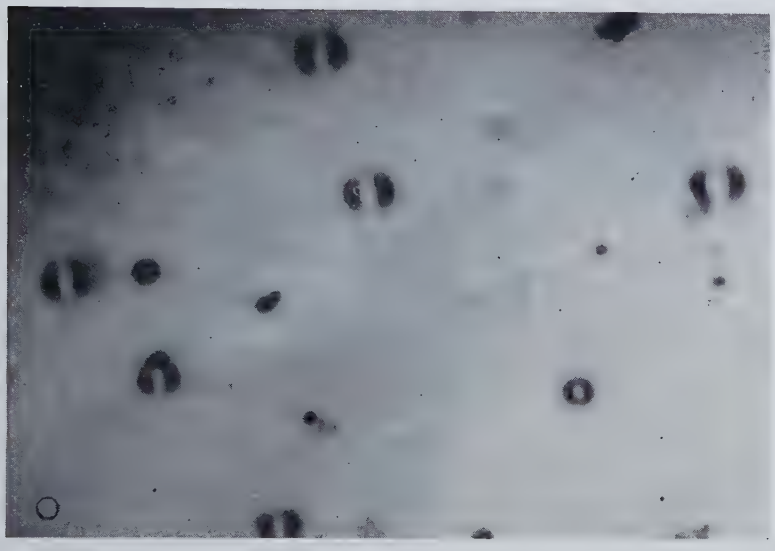

(*a*)

(*b*)

1 μ

Sequence showing the annealing of loops at room temperature. The numbers refer to the time in minutes at which exposures were made.

Fig. 11 (*continued*)

(*c*)

(*d*)

1 μ

Fig. 11 (*continued*)

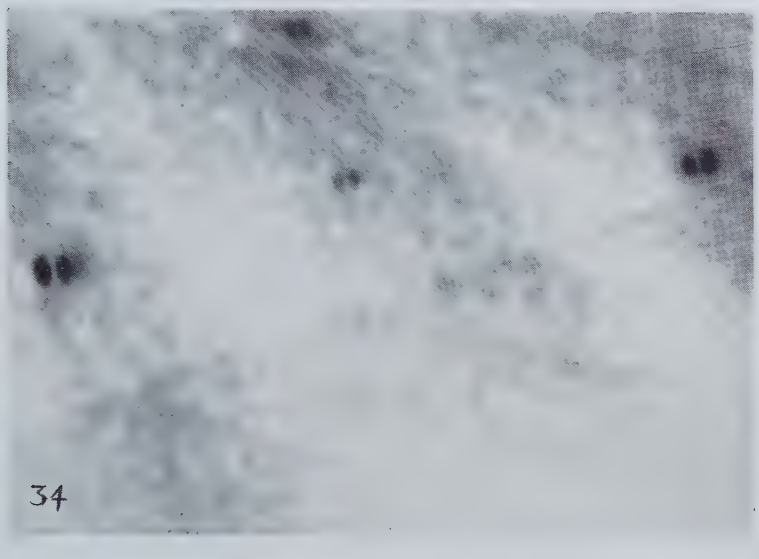

(*e*)

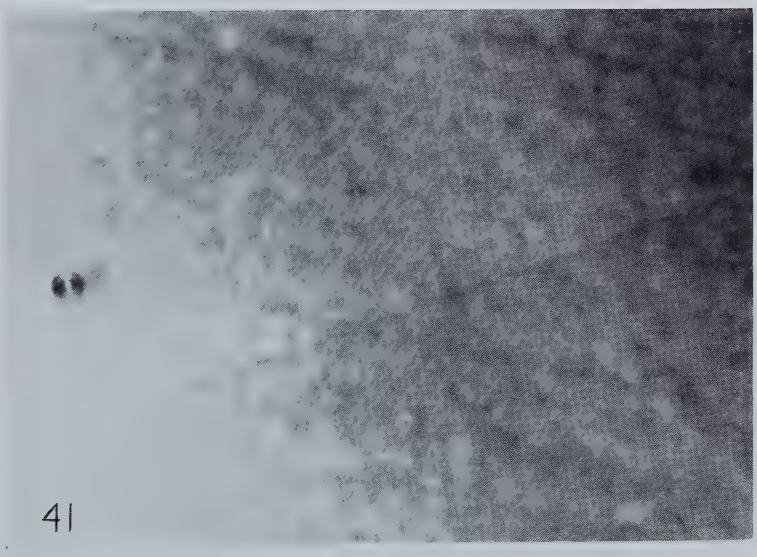

(*f*)

1 μ

Fig. 1

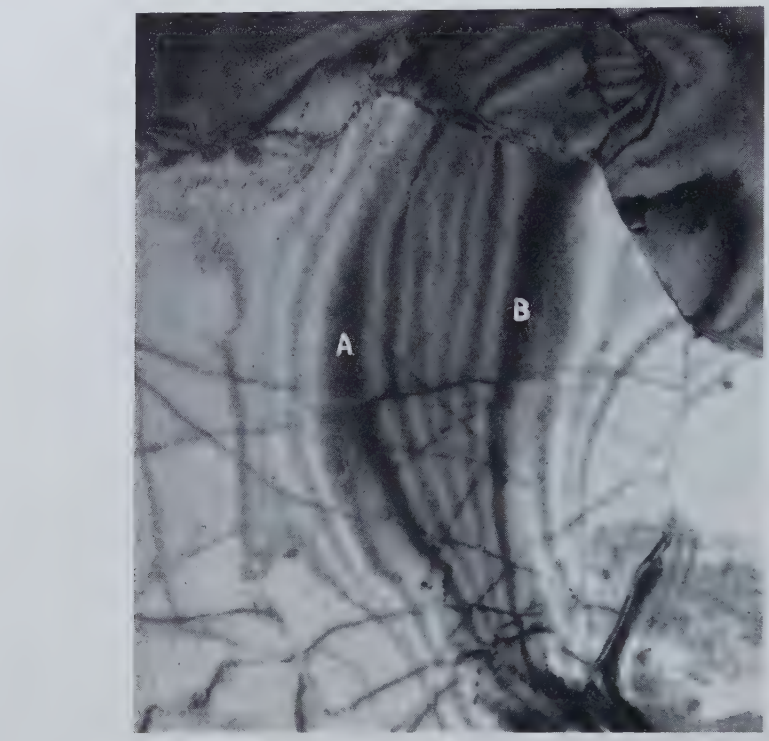

0·5 μ

(*a*)

(*b*)

(*a*) Bright field micrograph of a bend extinction contour in aluminium foil. The contour is produced by the 111 reflection (A) and the $\overline{1}\overline{1}\overline{1}$ reflection (B). Note the difference between the intensities transmitted inside and outside the contour. Mag. $\times 53\,000$. (*b*) Dark field image of the same region in the 111 reflection.

Fig. 2

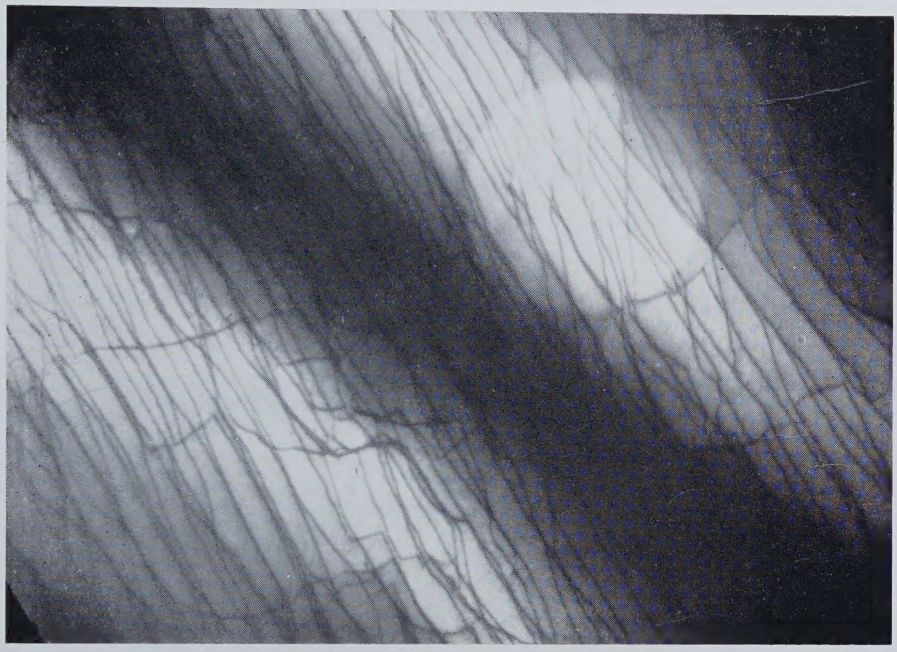

0·5 μ

Bright field micrograph of a bend extinction contour in a thick region of copper foil (exact thickness not known). The transparent regions correspond to strong 111 and $\overline{111}$ reflections respectively. Note the absence of subsidiary maxima and minima as in fig. 1 (*a*). Mag. $\times 30\,000$.

Fig. 7

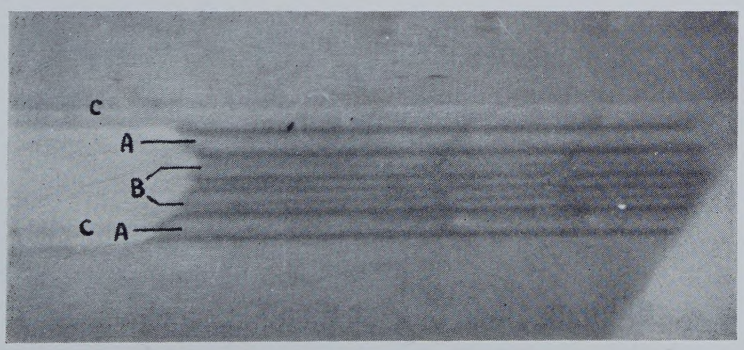

1·0 μ

Bright field micrograph of a stacking fault in stainless steel. Note the subsidiary dark fringes B and the absence of similar fringes at A. Compare with fig. 5 (*a*). C – C is a slip trace produced by a moving dislocation and should not be confused with the fault contrast. Mag. $\times 130\,000$.

Fig. 8

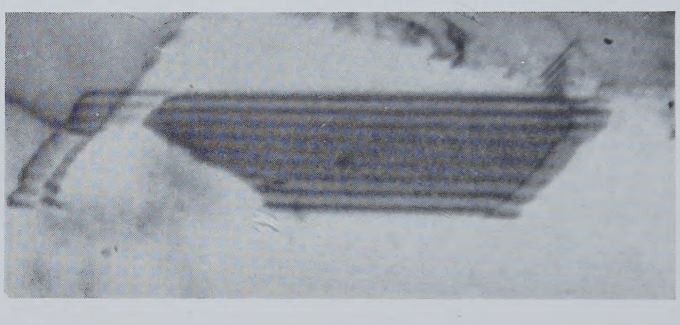

0·1 μ

Bright field micrograph of a stacking fault in stainless steel showing fringes similar to the type predicted in fig. 6 (*a*). Note the decrease in visibility of the fringes near the centre of the fault. Mag. $\times 130\,000$.